High Performance Multimode Fiber Systems: A Comprehensive Approach

A Thesis
Presented to
The Academic Faculty

By

Arup Polley

In Partial Fulfillment
of the Requirements for the Degree
Doctor of Philosophy
in the School of Electrical and Computer Engineering

Georgia Institute of Technology
December 2008

High Performance Multimode Fiber Systems: A Comprehensive Approach

Approved by:

Dr. Stephen E. Ralph, Advisor
School of Electrical and Computer Engineering
Georgia Institute of Technology

Dr. John D. Cressler
School of Electrical and Computer Engineering
Georgia Institute of Technology

Dr. G. K. Chang
School of Electrical and Computer Engineering
Georgia Institute of Technology

Dr. John R. Barry
School of Electrical and Computer Engineering
Georgia Institute of Technology

Dr. Rick P. Trebino
School of Physics
Georgia Institute of Technology

Date Approved: November 4, 2008

Dedicated to

My parents, Shri Anil Kumar Polley and Smt. Hira Polley
for their love, blessing, and sacrifices

My uncle Dr. Pranesh Chowdhury
for his inspiration, support, and teachings

CONTENTS

ACKNOWLEDGEMENTS

This dissertation would not have been possible without the help of many people over the past few years. First of all, I thank my advisor, Dr. Stephen Ralph, for his motivation, technical supervision, and support. I would also like to thank my committee members, Dr. John D. Cressler, Dr. G. K. Chang, Dr. John R. Barry, and Dr. Rick P. Trebino, for their time and encouragement.

I express gratitude for the valuable technical contributions and advices from the past and present student members of the Ultrafast Optical Communications Laboratory: Ketan M. Patel, Jeffrey J. Lillie, Joong H. Kim, Kasyapa Balemarthy, Rohan J. Gandhi, Shannon M. Madison, and Patrick J. Decker. Of these, the mentorship of Ketan M. Patel and Kasyapa Balemarthy are especially significant.

I am grateful to Patrick O' Farrel, and Jim Weiser (National Semiconductor) for providing assistance and guidance during the Litelink project, which I was a part of. I am thankful for the technical suggestions and support I received from Mike Wincn and Robert Dahlgren (University of California Santa Cruz) during this collaborative project. Special thanks are due to Stanton Halpern of Georgia Tech Research Institute for assistance with the receiver development.

A lot of credit goes to my colleague and longtime friends, Saikat Sarkar, Padmanava Sen, Bevin G. Perumana, for their assistance during the times of need. I also appreciate the advices and contributions from Arindam Basu, Tanmoy S. Mukherjee, Rajarshi Mukhopadhyay. I thank my friends at Georgia Tech., namely Mrinmoy Ghosh, Atri

Dutta, Jacob R. Minz, Vidyakiran Yalavarthy, Biswajit Mitra, and many more for the support and the years of fun.

Finally, no person can be successful without the love and support of his family. I am thankful to my loving wife Rita for her patience, moral support, and for making life full of joy. Acknowledgement goes to my brother Anirban Polley for his encouragements. I will always be indebted to my uncle Dr. Pranesh Chowdhury for not only igniting the passion for knowledge since my childhood but also for giving it a direction. Finally, deepest gratitude is reserved for my parents, Shri Anil Kumar Polley and Smt. Hira Polley, who with their love, blessing, and sacrifices, have made this possible.

LIST OF TABLES

LIST OF FIGURES

SUMMARY

Steady increases in the bandwidth requirements of access networks and local area networks have created a need for short-reach links supporting data rates of 10 Gb/s and larger. Server applications and data center applications too require such links. The primary challenge for these links lies in the reduction of the cost while retaining or improving the performance.

Traditionally, multimode fiber (MMF) has satisfied these needs because of its low installation cost resulting from the alignment tolerance associated with the large core size. However, in view of the ever-increasing performance requirements, extraction of the best performance requires a holistic view of the channel that involves global optimization of transmitter, fiber, receiver performance and signaling strategies. The optimization results in a channel impairment mitigation technique that is a combination of optical, opto-electronic, and electronic methods.

Both glass and plastic MMF links have been addressed in this work and many of the advances apply equally to both media. One example that applies strictly to glass MMF is the use of Raman amplification to not only combat attenuation but to reduce intersymbol interference (ISI). Raman amplification was demonstrated as an optical channel impairment mitigation technique enabling multi-km, multi-Gb/s transmission over glass-MMF. We demonstrated both numerically and experimentally that a power penalty reduction of 1.4 dBo can be achieved for 10 Gb/s transmission over 9 km of 62 μm glass MMF with a Raman pump power 250 mW.

In recent years, plastic optical fiber (POF) has emerged as a potentially lower cost alternative to glass-MMF in enabling high performance links. The primary objective of this research is to explore the possibilities and develop low-cost, short-reach, high-data-rate POF-links. Using a comprehensive multimode fiber model, we showed that strong mode coupling, together with a reasonably accurate refractive index profile enables 40 Gb/s transmission over 200 m of graded-index POF. We experimentally demonstrated 40 Gb/s error-free transmission over 100 m of graded index perfluorinated POF (GI-PF-POF). We also demonstrated that even larger core (120 μm) GI-PF-POF can support >10 Gb/s over 100 m length. We numerically computed and experimentally measured the differential modal delay of GI-PF-POF to demonstrate that the available bandwidth is nearly independent of the launch conditions. Therefore, the alignment tolerance at the transmitter is increased resulting in a dramatically reduced packaging cost at the transmitter.

However, the large-core POF increases the difficultly in capturing of the light efficiently onto a detector and results in optical power penalty and associated modal noise. To solve this, we have designed and developed a 10 Gb/s photoreceiver consisting of a large (100 μm diameter) GaAs PIN photodetector and a regulated cascade input based transimpedance amplifier (TIA) with low input impedance.

Thus, a low-cost, alignment-tolerant, high-data-rate link is realized that uses a high-power, high-speed vertical cavity surface emitting laser (VCSEL) transmitter, large-core, high-speed GI-PF-POF, and the developed receiver.

CHAPTER I

INTRODUCTION

Over the past few decades, advances in communication technology and an increasing reliance on information exchange in society and economy have inspired and supported each other. As a result, there has been tremendous growth in wired, wireless, and optical fiber communication. One of the primary technical challenges in enabling high-data-rate communication is the enhancement of link bandwidth and reach while keeping the complexity and cost of systems low. In the case of wired communication, optical fiber has clear advantages over copper wire in terms of bandwidth, loss, and cross talk, which become extremely critical in high-speed links. Single-mode fiber (SMF) almost exclusively serves as the backbone of the network because of its extremely low loss and large bandwidth, which are desirable for high-data-rate, long-haul systems. On the other hand, multimode fiber (MMF) provides the necessary bandwidth for short reach links at a much lower installation and component cost compared to SMF and copper wire. Therefore, it is widely used for the "last mile" reach in the access network.

1.1. Motivations

A steady increase in the total internet traffic over the last two decades has not only increased the bandwidth requirement of the backbone network, the demand for bandwidth of the end-user has also increased dramatically. As a result, the 10 Gb/s or even higher

data-rates, which are typically reserved for long-haul systems are deployed for local area networks (LANs). Along with that, the increasing speed of microprocessors can now support data center or server applications at a much higher rate. This is reflected in the need for high-speed links for storage area networks (SANs), and data center interconnects.

1.1.1. Why multimode fiber?

However, the design of communication link for LAN or data-center applications is different from that of long-haul systems. A significant part of the cost of the network and the components is provided by the end-user and therefore a challenge in designing access network is the reduction of overall cost while retaining high bandwidth. Along with the cost of the components of the link, the packaging and installation play a key role in influencing the design.

Though MMF cannot support the bandwidth-distance achievable in SMF, it is used in the vast majority of the LAN links because it provides the necessary bandwidth for short reach links at a much lower installation and component cost. Because of the larger size of the MMF core compared to SMF, the placement tolerances of the laser at the transmitter and the photodetector at the receiver relative to the fiber are greatly relaxed and therefore permit passive alignments resulting in reduced assembly costs. Moreover, inexpensive materials such as plastics can be used for some of the components, further reducing the cost [1]. Along with that, 850-nm vertical cavity surface emitting lasers (VCSELs) are widely used as transmitters for the MMF links for their cost benefits.

1.1.2. Need for improved MMF links: 10 Gb/s Ethernet and beyond

Ethernet is the most widespread wired LAN technology and the development of Ethernet standards goes hand in hand with the adoption and development of improved MMF channels. Figure 1 provides a brief description of the current 10 Gb/s and the possible future Ethernet standards over copper and fiber links. The trend of extending the reach and data rate of the links is obvious in the previous standards and the 10GbE standards shown in the figure. Although the twisted pair of copper wires is a relatively low-cost and low-power solution compared to the MMF solutions, the motivation for the transition from the Cu links to the MMF links is their much higher available bandwidth. However, the need for even higher performance MMF solutions is apparent.

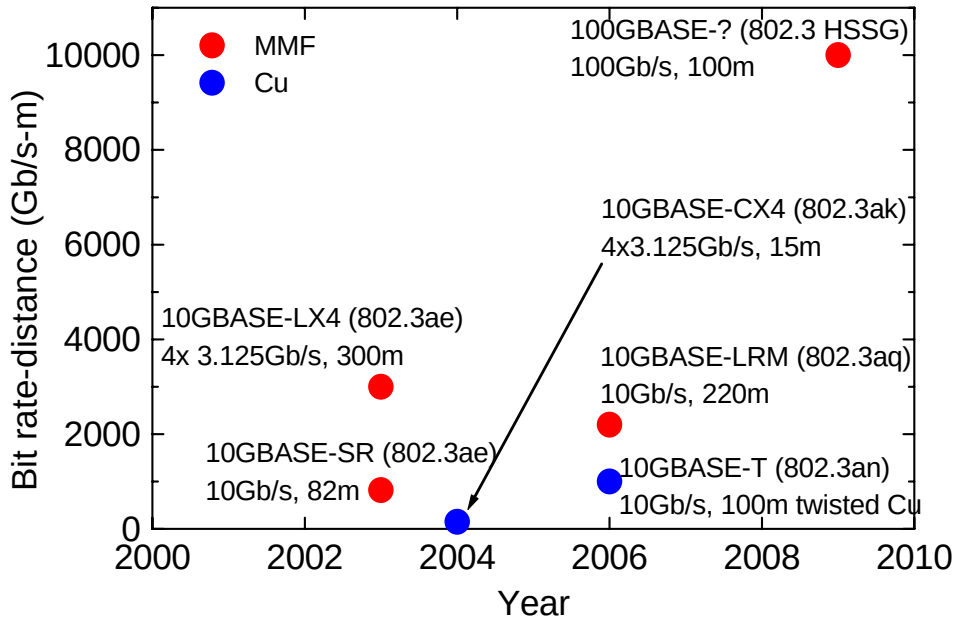

Figure 1. 10 Gb/s Ethernet standards over MMF and copper links

The extension in the reach from 82 m in 10GBASE-SR to 220 m in 10GBASE-LRM has been achieved by the use of electronic equalizer with the already deployed MMF links. Apart from this electronic method of improving fiber link performance, optical channel impairment mitigation methods and channel modulation methods are also needed to be explored to improve the overall link performance.

1.1.3. Need for low-cost, high-performance, short-reach links

Traditionally, copper cables have been considered as the low-cost, reasonably high-speed alternative for all short-reach applications including data-center, server applications and LANs. Though glass-MMF outperformed copper cables in terms of bandwidth, the low cost and ease of handling of copper cables are still not achieved in fiber links. Recently active cables have emerged as another potential solution that provides many of 'user-friendly' benefits of the copper cables along with all the performance advantages of the fiber channels. It can be described as a "hard-wired" fiber cable where transmitter and receiver are already attached to the fiber so that the end-user can directly access the electrical input and output signals. There are several advantages of using active cables compared to conventional fiber cables or copper cables; they are: a) larger bandwidth-reach, b) no need for eye safety, splicing, cleaning and other connectorization issues, c) lighter in weight – easier handling, d) requires less volume – increases airflow, improves cooling, e) indifferent to electromagnetic interference, g) smaller bend radius – inherent to thinner fiber, h) relief from unintended ground loops. In recent times, there have been several commercial products exploiting the concept of active cables. Although this

solution takes the burden of fiber installation off the end-user, the challenge still lies in the development of low-cost active cables while maintaining the bandwidth.

1.1.4. Why plastic optical fiber – *plastic* multimode fiber?

Plastic optical fiber has a history that even predates that of glass fiber, and yet it has been completely overshadowed by the glass fiber in the last decade. The primary reason is the much lower loss of glass fiber (0.2 dB/km for SMF and <3 dB/km for MMF) compared to the high loss of early POF (typically 200-1000 dB/km). As a result, POF found application primarily in the automotive industry as a low-performance and short-distance link.

However, recent advances in the manufacturing process of POF has established it as an alternative to glass-MMF and copper links for short-reach and high-data-rate links [2][3]. In fact, conventional glass-MMF and POF both have the same basic advantages of a large-core fiber and they both are perfect candidates for LANs and interconnects. Compared to glass-MMF, POF has some other advantages, such as, potentially low component and overall system cost, ease of connectorization, and mechanical flexibility [2]. Furthermore, POFs are generally made with large core size (100 μm to 1 mm) that provides more tolerance in connectorization. However, there are several issues that need to be addressed to make POF links a viable solution for short-reach links. These issues include bandwidth of large-core POFs, design of suitable receiver, attenuation in POF and its impact on the power budget. These issues are extensively explored to develop high-bandwidth, short-reach POF links.

1.2. Organization of the thesis

The dissertation is organized as follows. Chapter 2 revisits the fundamentals of MMF links. The primary mechanisms that contribute to the channel impairments and the prior art to combat these impairments are briefly reviewed. Then a comprehensive, numerical MMF model that has been developed in-house and extensively used in the current research work is described. As an application of the model a method to estimate the mode coupling in MMF is developed. Experimental measurements and numerical analysis that corroborate the validity of the MMF model and estimate the mode coupling strength in glass-MMF are described.

Chapter 3 discusses the use of Raman amplification to not only combat attenuation but to reduce intersymbol interference (ISI) in multi-km, multi-Gb/s transmission over glass-MMF. Both numerical analysis and experimental evaluations demonstrating the effect of Raman amplification in glass-MMF are described. It is demonstrated that a power penalty reduction of 1.4 dBo can be achieved for 10 Gb/s transmission over 9 km of 62 μm glass MMF with a Raman pump power 250 mW.

Chapter 4 introduces the state-of-the-art in POF with brief description of the availability of POF and its bandwidth, attenuation, and mode coupling properties. A summary of the link performance reported in the literature is presented. A brief comparison of the glass-MMF and POF is performed that forms the preliminary basis for determining the more suitable candidate for low-cost, high-performance, short-reach links. A comprehensive numerical analysis of the GI-PF-POF is performed with an emphasis on the effect of strong mode coupling on the response of POF channel. The experimental measurement results supporting the numerical analysis are presented that

show that GI-PF-POF has large bandwidth with Gaussian-like response and nearly launch-insensitive response. These results indicate that the high-data-rate POF link with a large alignment tolerance at the transmitter is achievable.

Chapter 5 describes the development of large active area photoreceiver for MMF links. The photoreceiver is comprised of a GaAs photodetector with a diameter of 100 μm and a regulated cascade input based transimpedance amplifier with large tolerance to input capacitance. The developed photoreceiver increases the ease of collection and reduces of alignment requirements. The ac analysis and noise analysis of the TIA are performed and optimization rules for the best frequency response and minimum noise are developed. Experimental evaluation of the receiver is presented including eye diagrams and bit error ration (BER) curves at 10 Gb/s.

Chapter 6 demonstrates the link performance using POF which are shown to have large bandwidth in chapter 4 and high-speed receivers including the large-area receiver described in chapter 5. In this chapter experimental results demonstrating a record 40Gb/s data transmission over POF are described. Finally, a highly alignment tolerant POF link using multimode VCSEL, 120 μm core POF and the developed receiver is demonstrated. This demonstration forms the prototype of the high-performance, low-cost, short-reach link that has been the goal of the research.

The unique contributions of the research work are summarized in chapter 7. At the end, the future directions are presented.

CHAPTER II

MMF BASICS AND MODELING

2.1. Introduction

A comprehensive knowledge of the transport mechanism of a medium is essential for the appropriate use of it as a transmission channel. In addition, a proper understanding of the origin and the magnitude of the channel impairments is necessary for the synthesis and analysis of impair mitigation methods. In this chapter we first explore some of the important concepts related to MMF links that directly affect its performance as a communication medium (section 2.2). We also describe a full MMF model that has been extensively used throughout the entire work (section 2.4). Finally we present a novel method that has been proposed and developed to investigate the mode coupling in MMF (section 2.5).

2.2. Issues in multimode fiber links

Like any communication channel, an MMF channel also suffers from various signal distortions limiting its usefulness. In this section, the primary mechanisms contributing to the channel impairment in MMF are discussed. Glass-MMF and POF both are essentially large-core optical waveguide supporting multiple transverse electromagnetic modes and they suffer from similar channel impairments. In the following subsections the primary challenges related to both types of MMF channels are examined. Although

some of these issues are interrelated, they are separately identified for clarity. In each subsection, first the origin of the problem is briefly described and then its specific impact on glass-MMF and POF is elaborated.

2.2.1. Inter-modal dispersion

Inter-modal dispersion is the primary bandwidth-limiting mechanism in multimode fibers. At the wavelength of interest, graded-index MMF supports hundreds of propagating waveguide modes with different transverse electric field profiles, propagation constants, and group velocities. The launched optical power is distributed among different modes and arrives at the fiber end with different delays. This inter-modal dispersion causes pulse broadening and inter-symbol interference (ISI) in On-Off Keying (OOK)-modulation-based optical communication via MMF [1][4].

Typically, the MMF bandwidth property is described in terms of bandwidth-distance product and differential modal delay (DMD) [5]. DMD is widely used to quantify the MMF bandwidth when a large number of modes are excited. To perform a DMD measurement, a short pulse is launched into the MMF via a small-diameter source (~5μm), typically a SMF, at different offsets from the center of the core. Depending on the offset, different modes are excited and the pulse energy arrives at different delays. DMD [s/m] is quantified by the temporal width at 25% of the peak signal strength of the fiber response for all offsets.

2.2.2. Accuracy of refractive index profile

In MMF, group delays of the individual modes depend strongly on the refractive

index profile. In fact, the graded refractive index profile yields a much smaller DMD compared to the step index profile by properly compensating the optical path length along the fiber for different transverse modes. The refractive index profile of a typical graded index MMF is given by the standard α-profile [4]:

$$n(r) = \begin{cases} n_1 \sqrt{1 - 2\Delta \left(\frac{r}{a} \right)^{\alpha}} & 0 \le r \le a \\ n_1 \sqrt{1 - 2\Delta} & r \ge a \end{cases}, \quad (1)$$

where r is the radius from the center of the core, a is the radius of the core-cladding interface, n_1 is the peak refractive index within the core, α is the profile parameter, and Δ is the maximum index contrast ratio between cladding and core. The DMD is minimized for $\alpha \approx 1.97$ (nearly parabolic profile) when profile dispersion [4] is ignored. However, because of the limitations in the manufacturing process, deviation from ideal refractive index profile occurs. Refractive index profile can also vary along the length of the fiber. All these contribute to an excess DMD compared to the ideal graded index profile.

Based on the 10-Gb/s Ethernet standards (IEEE 802.3aq) development efforts, a set of 108 index profiles with corresponding modal delays for 300 m of fiber has been employed to represent the most problematic MMF that may be found in installed FDDI networks [6]. The index deviations include dip and peak at the core center, sub-optimal α (1.89, 2.05), imperfect transition from core to cladding, and kink perturbations. The modern glass-MMF manufacturing process has certainly improved and the degree of imperfections mentioned above has reduced.

In the case of POF, the manufacturing processes are still developing and although graded index profiles with varied core sizes are produced, the accuracy of the generated

profile is not yet available.

2.2.3. Connectorization

One of the primary driving forces of MMF economy is the large alignment tolerance of the MMF links compared to the SMF links. The connector tolerance required for SMF with 8-10 μm core size is much stricter compared to the typical 7 μm tolerance of the 50/62.5 μm core MMF. This larger tolerance in the connector offset allows for simple implementation of connectors and reduces the optical packaging cost of the transmitter and the receiver.

Connector offset has a significant impact on the impulse response of glass-MMF links with only a few modes excited, e.g., restricted mode launch condition. The connector offset near the transmitter or somewhere along the link changes the mode power distribution (MPD) and as a result, the delay spread of the excited modes changes. The connector offset can also introduce mode-selective attenuation, resulting in modal noise (section 2.2.4).

POF employs inexpensive and simple termination, where two fiber ends can be butt-coupled or even crimped on [7].

2.2.4. Modal noise

Modal noise is an additive and signal-dependent amplitude noise that is specific to multimode fiber links [8]. When a coherent light propagates through a MMF via a number of modes, interference between these modes yields a speckle pattern at the fiber

end-face. This speckle pattern is extremely sensitive to the phase difference among the modes, which can vary with time from a) a change in fiber characteristics resulting from external forces, temperature change b) changes in the laser transmission wavelength. A misaligned connector in the fiber link or partial detection in the photodetector can produce speckle-dependent loss and result in modal noise. Modal noise has been extensively explored and modeled in the early years of investigation on MMF links. Modal noise can result in a power penalty and more importantly can potentially result in an asymptotic bit-error-ratio floor [9].

2.2.5. Mode coupling

The transverse electromagnetic modes are an orthogonal set of modes in a MMF waveguide and ideally there should not be any interaction among the excited modes. However, in reality, imperfections in the waveguide such as changes in diameter, elliptical core deformations and random bends of the axis lead to coupling of modes, i.e., power is transferred from one mode to the other. This phenomenon is called mode coupling and it has two important consequences. First, the spatial intensity profile inside the fiber changes along the length of the fiber as different modes are excited. Second, since power is transferred among modes with different group velocities, the temporal response of the fiber changes. Significant work has been done and published on mode coupling in MMF in the early years of MMF investigation. A comprehensive theory of mode coupling had been developed that describes the phenomenon using the coupled power equation among different mode groups [10][11].

Efforts have been made to quantize the mode coupling efficiency. These methods are

essentially based on comparing the evolution of MPD observed experimentally with that predicted by the mode coupling theory. However, the MPD of numerous modes present can only be approximately estimated by analyzing the far-field image of the fiber output. One of the widely used methods employs changing the launching condition to control the selective excitation of lower-order modes (LOMs) to higher-order modes (HOMs). This can be performed by exciting the fiber with plane waves at different angles with the fiber end-face [12]. The larger angle excites the HOMs, whereas the normal incidence excites primarily the LOMs. Another method is to launch with a SMF at different offsets from the MMF core-center [13]. Increasing the offset from the core excites increasingly HOMs. In the case of low mode coupling, the far-field pattern looks like an annular shape when the HOMs are excited; on the other hand, the far-field pattern takes a disk shape with primarily the LOMs excited. Strong mode coupling in a MMF changes the launched MPD and the far-field pattern takes the disk shape even when HOMs are excited. This method can be used to estimate the mode coupling strength when the mode coupling effect is large.

It is also known from the theory that under strong mode coupling, the temporal response of the fiber takes a Gaussian response whose full width at half of the maximum amplitude (FWHM) increases proportionally with the square root of the fiber length [10].

Accurate quantization of the mode coupling in modern glass-MMF and its impact on the temporal response is required to evaluate the glass-MMF-channel performance. This issue is addressed in section 2.5.

POF exhibits strong mode coupling and this issue is taken up in detail in section 4.2.4.

2.3. Channel impairment mitigation in MMF: Prior art

Optical channel impairment mitigation schemes can be broadly classified into optical, electronic, and opto-electronic methods. The effectiveness of any of those schemes has to be evaluated in terms of cost and performance. In general, an optimum balance between the optical and electrical signal processing produces the best solution for optical channels. In the case of glass-MMF, the primary channel impairment is the bandwidth limitation resulting from inter-modal dispersion. In the following paragraphs, some of the notable inter-modal dispersion compensating schemes are briefly described.

2.3.1. Controlled launch condition

The bandwidth of a glass-MMF depends strongly on the number of modes excited and the power distribution among them. Therefore, different spatial intensity profiles at the source are used to control the MPD and thus to maximize the achievable bandwidth. The two important launch conditions are – overfilled launch (OFL), where the fiber core is filled with input light and many modes are excited; and underfilled launch (UFL) or restricted mode launch (RML), where only part of the fiber core is illuminated and a few modes are selectively excited. Two different variations of UFL employed by the IEEE802.3aq are a) center launch (CL), where the MMF is excited near the center with a maximum offset tolerance of 7 μm, and b) offset launch (OL), where the MMF is excited at 18-23 μm offset from the core center [14].

2.3.2. Spatially resolved equalization

The MMF modes have different spatial intensity profiles and delays. These modes are spatially resolved using multi-segment photodetectors at the end of propagation and the temporal responses from different detectors are optimally combined to achieve higher bandwidth. In the simplest implementation, the difference of the response from two concentric photodetectors – one circular and one annular - improves the bandwidth nominally by a factor of two [15].

2.3.3. Electronic equalization

MMF is a linear channel and the channel impairment can be effectively mitigated by inverting the channel by the use of electronic filters [16]. The two widely used filter topologies are a) feedforward equalizer (FFE), which is a linear finite impulse response (FIR) filter and b) decision feedback equalizer (DFE), which uses the decisions made on earlier symbols to predict the current symbol. Electronic equalization to enhance the reach and bandwidth of glass MMF is a part of the IEEE802.3aq standard.

2.3.4. Multi wavelength transmission

Like SMF, MMF also has a wide low-loss transmission window that can be effectively utilized by transmitting at multiple wavelengths. Course wavelength division multiplexing (CWDM) and subcarrier multiplexing (SCM) [17] are two such techniques that have been proposed and investigated for MMF links.

2.3.5. Multilevel modulation

Instead of two-level binary transmission, pulse amplitude modulation (PAM) with more levels such as PAM-4, PAM-8 etc. can be used to transmit at higher data rates within the bandwidth constraint of MMF.

2.3.6. Other electronic methods

MMF is viewed as a low-cost, short-reach and high data-rate medium, and the application of complex link performance improvement techniques that are used in wireless, wired, and long-haul SMF channels may be considered prohibitively expensive. Forward error correction is widely used in long-haul systems and can significantly improve the bit error ratio (BER) of a channel. A simplified and hybrid version of error correcting techniques such as the Viterbi algorithm have been investigated and proved to be useful for MMF links [18].

2.4. Comprehensive model development for multimode fiber

The performance evaluation of any communication channel requires a comprehensive and accurate model of the channel. A multimode fiber channel, in general, has the property that channel response can widely vary, depending on the numerous factors such as variation in the refractive index profile of the fiber, output intensity profile of the source, coupling of light into the fiber, response of the photodetector, etc. Therefore, it is

extremely important to perform a full end-to-end channel analysis considering the variation in different factors that influence MMF response.

Extensive research on and publication of the physical model of MMF have been performed during the development of glass-MMF [4][10]. Primarily based on those works, a comprehensive and accurate model of MMF has been developed by the Ultrafast Optcal Communication group at the Georgia Institute of Technology and a detailed description of that model can be found in [19]. A summary of the model is provided in the following sections. Experimental measurements are performed to quantify the effect of mode coupling in commercially available MMF using the MMF model (section 2.5).

The multimode fiber model consists of two primary components: mode solver and mode propagator under mode coupling.

2.4.1. Mode solver

Multimode fiber supports a multitude of electromagnetic modes that propagate along the fiber with a characteristic transverse electric field profile also called mode field profile, propagation constant and group velocity. These properties of the fiber modes depend primarily on the refractive index profile of the MMF (section 2.2.2) and the wavelength of operation. The mode fields are actually eigenfunctions of the wave equation appropriate for a dielectric medium. Starting from the vector wave equation and applying the *slowly varying index* criterion of MMF, a scalar wave equation for the linearly polarized (LP) electric field $E(r,\phi)$ is obtained [4]. The radial component $R(r)$ of the mode profile and the propagation constant β are found via the solution of the scalar wave equation:

$$\frac{d^2R(r)}{dr^2}+\frac{1}{r}\frac{dR(r)}{dr}+\left(n^2(r)k_o^2-\beta^2-\frac{l^2}{r^2}\right)R(r)=0\,. \tag{2}$$

The azimuthal component $\Phi(\phi)$ is obtained from the solutions of

$$\frac{d^2\Phi(\phi)}{dr^2}+l^2\Phi(\phi)=0\,. \tag{3}$$

A finite-difference approach is used to solve the scalar equation for any arbitrary $n(r)$ and the solution provides the β_{lm} and $R_{lm}(r)$ for each propagation mode with radial and azimuthal mode number m and l, respectively. Using $R_{lm}(r)$ and $\Phi(\phi)$ the two-dimensional electric field profiles $E_{l,m}(r,\phi)$ of each fiber mode are computed.

$$E_{lm}(r,\phi)=\begin{cases}R_{lm}(r) & \text{for } l=0\\ R_{lm}(r)Cos(l\phi)\\ R_{lm}(r)Sin(l\phi)\end{cases}\text{for } l\geq 1 \tag{4}$$

Using the WKB approximation [4], the group delay per unit length of fiber τ_{lm} can be computed for pure α profiles:

$$\left(\frac{\tau_{lm}}{\tau_o}\right)^2=1+\Delta b\left(\frac{\alpha-2-y}{\alpha+2}\right)+\frac{(\Delta b)^2}{2}\left(\frac{3\alpha-2-y}{\alpha+2}\right), \tag{5}$$

where the normalized propagation constant is $b=\left(1-\left(\beta_{lm}/n_1k_o\right)^2\right)\Big/\left(1-\left(n_2/n_1\right)^2\right)$, the profile dispersion is $y=-\left(2n_1\lambda d\Delta c_o\right)\Big/\left(\tau_o\Delta d\lambda\right)$, c and k_o are the velocity of light and propagation constant in free-space, and τ_0 is the group delay resulting from core material properties. The higher-order terms are neglected. However, to compute the group delay for arbitrary $n(r)$, the Rayleigh quotient method is used [19].

The power launched in different modes depends on the source excitation. For a source electric field profile $E_s(r,\phi)$, the power P_{lm} coupled to mode (l,m) is found using

$$P_{lm} \propto \int_r \int_\phi E_s^2(r,\phi) E_{lm}^2(r,\phi)\, dr d\phi . \tag{6}$$

In the case of negligible mode coupling, the launched mode power distribution does not change during propagation through the fiber. With a sufficiently large photodetector, the modes maintain spatial orthogonality and contribute to the net photocurrent separately. Thus, the normalized photocurrent impulse response (IPR) $h_{mmf}(t)$, after fiber length L, is described as

$$h_{mmf}(t) = \sum_k P_k \delta(t - L\tau_k) . \tag{7}$$

Here, the modes with distinct (l,m) are enumerated using a single parameter $k \equiv (l,m)$ and the double sum is avoided.

In the case of graded-index MMF with $\alpha \approx 2$, modes with the same $g = 2l + m - 1$ form velocity degenerate mode groups. The number of modes with mode-group number g is the degeneracy of that mode group.

2.4.2. Propagation under mode coupling

Under the influence of mode coupling, power transfer occurs among the guided modes during propagation in a MMF and that in turn alters the channel response. This interaction is modeled by a set of coupled equations describing the power flow in a waveguide with N modes [10].

$$\frac{\partial P_n}{\partial z}+\tau_n\frac{\partial P_n}{\partial t}=-\gamma_n P_n+\sum_k d_{n,k}\left(P_k-P_n\right), \tag{8}$$

where P_n is the power in the nth mode at time t at a distance z. γ_n is the attenuation coefficient for the nth mode and $d_{n,k}$ is the coupling coefficient between two modes n and k. Assumptions that were used in deriving the coupled equations are a) the imperfections in the waveguide such as changes in diameter, elliptical core deformations, and random bends of the fiber axis lead to coupling of modes; b) these imperfections appear in a random fashion along the length of the waveguide, and statistical ensemble average can be taken. It should be noted that the perturbation interacts strongly with the phases of the field and the effect is integrated over the length of the waveguide. A Fourier spectra of the spatial frequency of the perturbation is determined to quantify the interaction with the propagation phase difference of the modes and the contribution is contained in the mode coupling coefficient $d_{n,k}$ given by

$$d_{n,k}=A\left[\frac{\left(\pi k_0 c\varepsilon_0\right)^2}{8}\rho_{n,k}^2\frac{1}{\left(\Delta\beta_{n,k}\right)^8}\right], \tag{9}$$

$$\rho_{n,k}=\int_0^\infty rE_n\left(r\right)E_k\left(r\right)\frac{\partial\left[n\left(r\right)\right]^2}{\partial r}dr\,, \tag{10}$$

where ε_0 is the free space dielectric constant. E_n is the radial electric field profile of the nth mode, $\Delta\beta_{n,k}$ is the difference in propagation constant of mode n and k, and A is the mode coupling strength. The electric field profile and the propagation constants are found using the mode solver. The electric field profile in Eq. (12) is normalized such that

$$\int_0^\infty rE_n^2\left(r\right)dr=\frac{k_0}{\pi}\sqrt{\frac{\mu_0}{\varepsilon_0}}\frac{1}{\beta_n}. \tag{11}$$

Complete mode coupling is assumed between the modes within a mode group as β_{nk} are very close, and strong coupling is suggested by Eq. (11). Since the adjacent mode groups have the smallest $\Delta\beta_{n,k}$, the coupling is dominated by them. The coupling coefficient d_g between two adjacent velocity degenerate mode groups g and g+1 can also be found using an approximate analytical solution [11], and it matches well with the exact value obtained using equations (9), (10), and (11).

$$d_g = \frac{1}{2}\left(\frac{nk_0}{a}\right)^2 \Delta^2 \left(\frac{g}{g_{TOT}}\right) \frac{A}{\left(\Delta\beta_{g,g+1}\right)^8}, \tag{12}$$

where g_{TOT} is the total number of mode groups present.

A split-step method is used to numerically solve a variation of Eq. (8), derived for velocity degenerate mode groups. The results provide the temporal response and MPD as a function of distance propagated along the fiber. The mode coupling strength A is a parameter representing the inherent fiber property and can be measured experimentally as described in section 2.5.

It is apparent from Eq. (12) that the MCC increases linearly with mode group number for pure α profiles. An effective MCC of a fiber is obtained by averaging the coupling coefficient across all mode group pairs. Mode coupling length (MCL) is defined by the distance required to reach a steady-state MPD inside the fiber [10]. This is obtained by solving the coupled power equations for the steady-state condition. The eigenfunction corresponding to the smallest eigenvalue provides the steady-state MPD of the fiber. The steady state MPD for a lossless system ($\gamma_n = 0$) is equal power in all modes (*not* mode groups). An estimate of the MCL is given by $L_c = 4.61/\left(\sigma(2) - \sigma(1)\right)$, where $\sigma(1)$ and $\sigma(2)$ are the two smallest eigenvalues of the coupled power equations [10]. This

definition ensures that the steady-state MPD is 100 times stronger than the next strongest eigenfunction.

2.5. Mode coupling in glass multimode fiber

Since mode coupling can potentially change the impulse response of MMF, it is important to quantify the mode coupling strength A in commercially available MMF to accurately estimate the link performance.

Apart from the change in MPD, the other obvious effect of mode coupling is the energy filling between the distinct mode groups and the corresponding change in the temporal response. Therefore, instead of comparing the change in MPD, we focus on the impulse response, which is sensitive to the mode coupling coefficient and is directly related to the channel performance.

Impulse response measurements of the MMF are done with sufficient temporal resolution and dynamic range to separate the mode groups distinctly and quantify the energy arriving between them. To minimize the chromatic dispersion, 16-ps-FWHM pulses at 1550 nm are launched. A mode-locked laser followed by a bandpass filter is used to generate the nearly transform-limited pulses. A detector-sampling module with net bandwidth of 20 GHz is used as the receiver. A GRIN lens couples all modes of 50-μm MMF in the detector with nearly 100% efficiency. The signal is launched into the MMF-core with a SMF at different offsets, which allows the control of the MPD. To reduce the noise, the response is effectively averaged for 32 minutes and dynamic range of three orders is obtained. Care is taken to minimize the jitter and drift in the acquired waveforms.

The use of 1550 nm helps to ensure that the primary modes are temporally separated because of large DMD at 1550 nm for fibers optimized at 1310 nm. Coupling strength A, which is a function of micro-bending perturbation and mechanical properties of fiber, is expected to be only slightly dependent on the wavelength of operation By comparing the measured impulse responses of 4 km of 50-μm MMF with the numerically generated impulse response, we estimate a coupling strength A of $1x10^8$ (Figure 2). The observed uniformity of arrival of the mode groups suggests that the fibers examined can be described by an α profile without any major index profile defects. Hence, in the numerical model, we assume the $\Delta\beta$'s to be that of a fiber with a pure α profile. The modal delays and the MPDs at the launch are adjusted for different correlation length to match the received waveform.

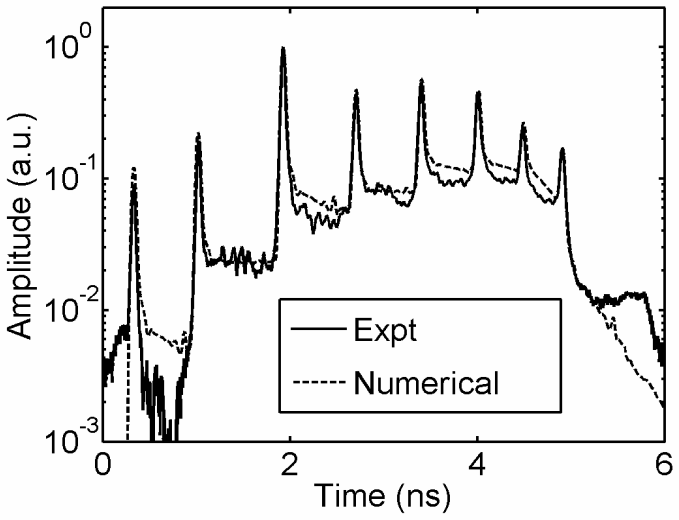

Figure 2. Comparison of measured impulse response and its numerical estimate for 4 km of 50-μm MMF. Energy appearing between the primary mode groups indicate the effect of mode coupling. Two qualitative observations as expected from the numerical results are: a) stronger mode coupling effect for higher order modes arriving later; b) asymmetric pedestal for the last mode group.

Similar measurements are performed with 1.1 km and 9 km of 62.5-μm-MMF (Figure 3). The coupling strength *A* of a typical 62.5-μm, FDDI-grade fiber is estimated to be $5x10^7$. The effective MCC is found to be 0.15 km^{-1}.

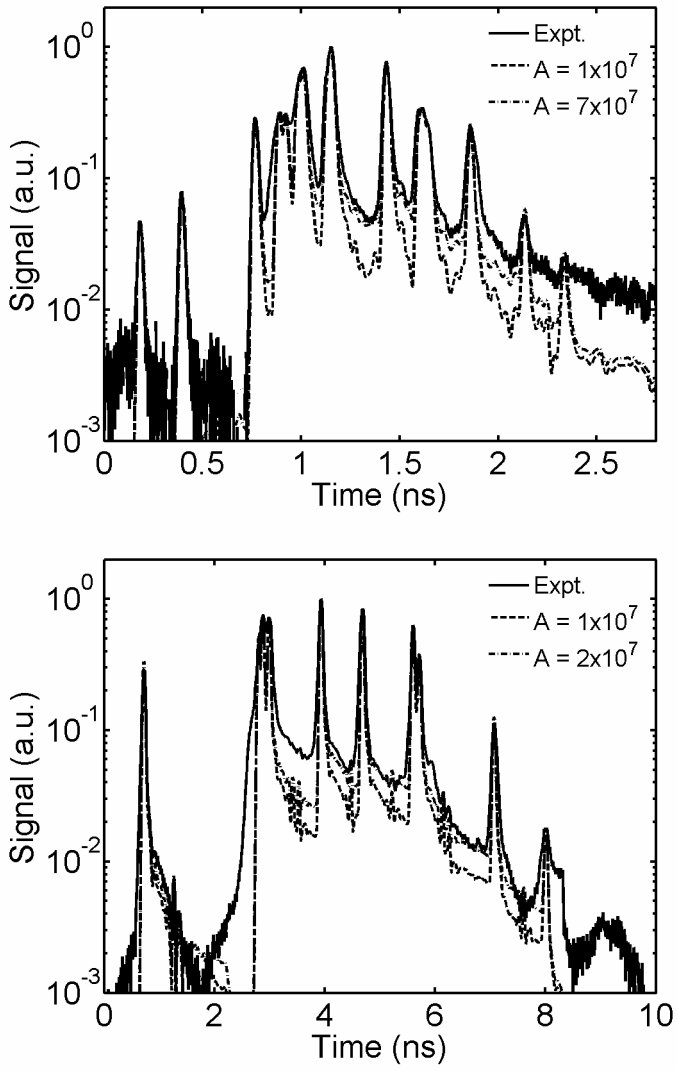

Figure 3. Two representative high resolution, high dynamic range 62.5-μm MMF responses a) 1.1 km b) 9 km. Modal coupling is identified by the strength of the response between the arrivals of the primary mode groups. For fiber (a) a coupling strength of A = $7x10^7$ provides the best agreement with the measured responses whereas for fiber (b) A = $2x10^7$ provides the best match. The coupling strength of these and other measured fibers is larger than A = 10^7.

The method described above is specifically suitable for MMFs with 'relatively small' mode coupling strength and therefore requires long length of fiber to have any perceptible effect on the impulse response. In that regime, modes can be resolved temporally and the estimation of mode coupling strength is more accurate than the methods relying on just the evolution of MPD. Here, it is noted that for smaller length of fiber, the temporal resolution can be improved by using narrower launch pulses and a receiver with larger bandwidth. However, the dynamic range of the measurement is often limited by the detector response, and an appropriate length of fiber should be chosen to clearly observe the mode coupling effects.

2.6. Summary

The described MMF model is numerically accurate and is critical to the investigation of the channel impairment mitigation schemes conceived for glass-MMF. In particular, Raman amplification in glass-MMF is extensively explored using the model in chapter 3. Experimental results accurately quantify the mode coupling in commercial glass-MMF and its impact on a long MMF channel is thoroughly investigated in [19]. The quantitative agreement between the measured and the numerically simulated MMF impulse responses without any adjustable parameter also validates the accuracy of the model in predicting the spatial and temporal behavior of MMF in the presence of mode coupling. The model is extensively applied to explore the behavior of POF, where the effect of mode coupling is significant.

CHAPTER III

RAMAN AMPLIFICATION IN MMF

3.1. Introduction

Distributed Raman amplification using the transmission fiber as the gain medium is an established technology for long-haul communication systems, especially for wavelength division multiplexed (WDM) systems, where simultaneous amplification of multiple channels is necessary to compensate for the fiber loss [20][21]. Some of the advantages of Raman amplifications are lower noise compared to erbium doped fiber amplifiers (EDFA), broad and flexible gain spectrum useful for WDM systems. However, its application in MMF links may be regarded as impractical, considering the typical reach and economy of conventional MMF links. On the other hand, it has been shown that the LOMs in MMF have larger gain compared to the HOMs [22][23] and this property has been used to demonstrate single-mode Raman fiber-laser operation [24] and beam cleanup and combining in MMF [25]. In early years, MMFs were used with LEDs that had large numerical aperture and excited lots of modes. Later, high-speed (≥1 Gb/s) MMF links used laser sources, which have a much smaller numerical aperture and excite only a few modes. In particular, center launch using a small area laser source excites only the lowest-order modes and yields a much smaller delay spread. This suggests that the lowest-order mode dominance in Raman amplification in MMF can be effectively exploited in a long-reach MMF-link with a center-launch excitation.

At first a comprehensive numerical modeling of the Raman amplification in commercially available graded-index MMF is performed (sections 3.2, 3.2.1, 3.2.2, 3.2.3). Following that, the effect of Raman amplification on MMF impulse response is examined numerically and experimentally (sections 3.3.1, 3.3.2).

3.2. Theory of Raman amplification in MMF

Unlike SMF, in MMF both the pump and the signal propagate in multiple modes. Therefore, the conventional Raman gain expression [21][26] is generalized to a gain matrix describing the interaction between the pump and signal modes. The gain of the j^{th} signal mode because of the i^{th} pump mode is given by

$$G_{ij} = \exp\left(\left(\frac{g_R}{A_{eff}}\right)_{ij} P_i L_{eff}\right), \tag{13}$$

where P_i is the pump power in the i^{th} mode and L_{eff} is the conventional effective length of the fiber. $L_{eff} = (1-\exp(-\alpha_p L))/\alpha_p$, where α_p is the attenuation coefficient of the pump and L is the fiber length. The effective Raman gain, i.e., the ratio of Raman gain coefficient g_R to effective area A_{eff} for ij pump and signal mode pair, is given by

$$\left(\frac{g_R}{A_{eff}}\right)_{ij} = \frac{\iint g_R(r) E_i^2(r,\theta) E_j^2(r,\theta) dr d\theta}{\iint E_i^2(r,\theta) dr d\theta \iint E_j^2(r,\theta) dr d\theta}, \tag{14}$$

where E_j and E_i are the transverse electric field profiles for the j^{th} signal and the i^{th} pump mode, respectively. The net gain for each signal mode j is found by summing the contribution from all pump modes:

$$G_j = \sum_i G_{ij} \,. \tag{15}$$

Finally, the modified impulse response of the MMF after mode-selective Raman amplification is given by

$$h_{mmfR}(t) = \sum_j G_j m_j \delta\left(t - \tau_j\right), \tag{16}$$

where m_j and τ_j are launched power and delay of the j^{th} mode.

3.2.1. Estimation of Raman gain coefficient

The higher refractive index in the core of MMF is achieved by doping GeO_2 in the silica. A graded refractive index profile is achieved by applying a graded doping along the core radius. Incidentally, GeO_2 also has a higher Raman gain coefficient compared to pure silica and thus GI-MMF has a radially dependent Raman gain coefficient.

The refractive index for pure silica and GeO_2-doped silica at the wavelength of operation can be found from the Sellmeier equation. The parameters of the Sellmeier equation for 0, 6.3, 8.7, 11.2, 15.0, 19.3% GeO_2-doped silica are listed in [26]. Refractive indices of silica with the above GeO_2 concentration are obtained at a signal wavelength of 1550 nm. The data points are fitted to a polynomial function that generates GeO_2 doping concentration from refractive index (Figure 4).

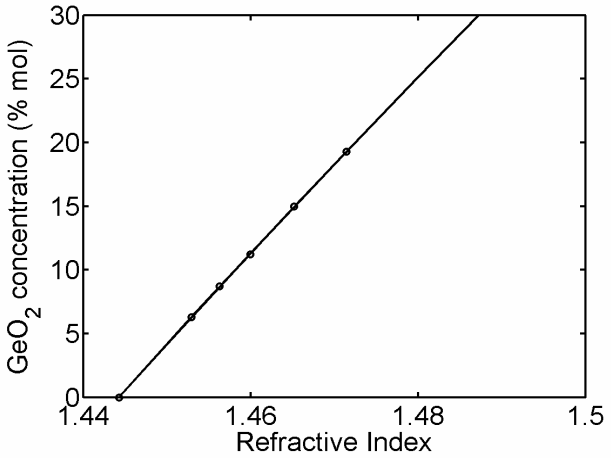

Figure 4. GeO_2 doping density vs. refractive index of GeO_2 doped silica.

Figure 5 shows the Raman gain coefficient for pure silica vs. the pump-to-signal frequency shift at a signal wavelength of 1 μm. The red and blue curves represent the Raman gain coefficient for pump light polarized parallel and perpendicular, respectively, to the polarization of the signal light. It shows that the total Raman gain is dominated by the parallel polarization. The peak gain coefficient of 1.046×10^{-11} cm/W is obtained at a frequency shift of 440 cm^{-1} with signal wavelength of 1 μm. For a depolarized pump and signal, the peak Raman gain coefficient reduces to $1.046 \times 10^{-11}/2 = 0.5023 \times 10^{-11}$cm/W.

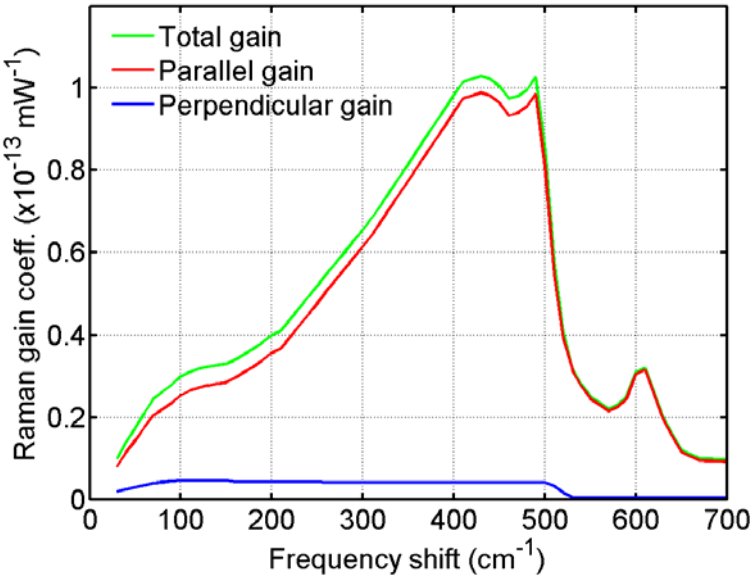

Figure 5. Parallel and perpendicular Raman gain coefficient of fused silica.

The Raman gain coefficient $g_R\left(x_{GeO_2},\nu\right)$ of doped silica with a GeO_2 doping density of x_{GeO_2} [mol %] and for a frequency shift of ν is given by

$$g_R\left(x_{GeO_2},\nu\right)=\frac{n_2^2}{n_1^2}\left[g_R\left(SiO_2,\nu\right)+c\left(\nu\right).x_{GeO_2}.g_{Rp}\left(SiO_2,\nu\right).\frac{\lambda_s^3}{\lambda_{sPeak}^3}\right], \qquad (17)$$

where n_1 and n_2 are refractive indices in a GeO_2-doped silica core and a pure silica cladding, respectively. $c\left(\nu\right)$ is a regression factor obtained from [26]. $g_R\left(SiO_2,\nu\right)$ and $g_{Rp}\left(SiO_2,\nu\right)$ are Raman gain coefficients of silica at the signal wavelengths λ_s and λ_{sPeak}, respectively. For a pump wavelength of λ_p, the Raman gain in silica peaks at a frequency shift of 440 cm^{-1} and the wavelength of the peak gain is given by

$\lambda_{sPeak} = \dfrac{1}{\left(\dfrac{1}{\lambda_p} - 440\times10^{-4}\right)}$. The Raman gain also varies linearly with frequency and the Raman gain for a signal wavelength of λ_s [μm] with a depolarized pump is given by

$$g_R\left(SiO_2,\nu\right) = \frac{0.5023\times10^{-11}\,cm/W}{\lambda_s[\mu m]}. \tag{18}$$

$g_R\left(SiO_2,\nu\right)$ and $g_{Rp}\left(SiO_2,\nu\right)$ are calculated using Eq. (20) and appropriate λ_s and λ_{sPeak}.

The most commonly used signal wavelength and pump wavelength for Raman amplification are 1550 nm and 1450 nm, respectively. Although typically MMF links are operated at 850 nm and 1310 nm wavelengths, a Raman amplified MMF link is preferred at 1550 nm because of the availability of pump diodes at 1450 nm. Therefore, the Raman gain coefficient as a function of GeO_2 doping density is computed for the signal wavelength of 1550 nm (Figure 6).

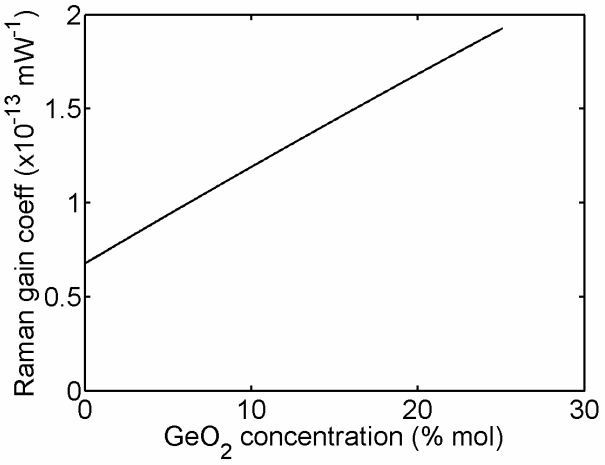

Figure 6. Raman gain coefficient vs. GeO_2 doping density in doped silica.

The results of Figure 5 and Figure 6 are combined to find the dependence of the Raman gain coefficient on the refractive index of GeO_2-doped silica (Figure 7). A polynomial function is constructed that is used to estimate the radial dependence of the Raman gain coefficient in the MMF-core.

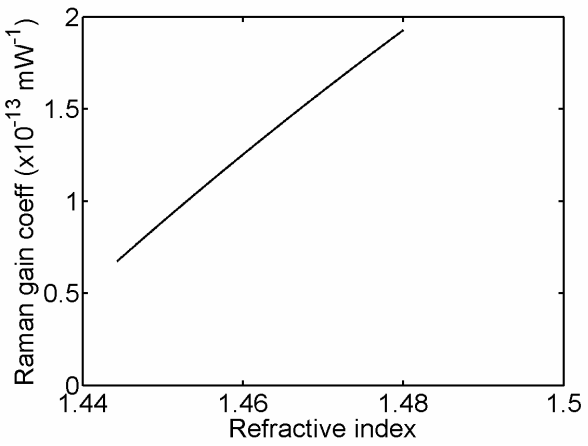

Figure 7. Raman gain coefficient vs. refractive index of GeO_2 doped glass

3.2.2. Estimation of Raman gain coefficient of MMF

Numerical evaluation of Raman amplification is performed for both 50-μm and 62.5-μm graded-index MMF. The pump attenuation coefficients of 62.5 μm and 50 μm MMF are 0.37 and 0.40 dB/km, respectively.

The peak index delta for 62.5-μm and 50-μm MMF are typically 2% and 1%, respectively. The mode solver uses a refractive index profile with α=2 to compute the transverse electromagnetic fields and group velocities of different modes. The transverse

electromagnetic fields are used for calculating the launched MPD (Eq. (6)) and the effective Raman gain (Eq. (14)).

From the parabolic refractive index profile, the GeO_2 doping concentration and subsequently the Raman gain coefficient as a function of radial distance are computed (Figure 8). To achieve the index delta in 50-μm and 62.5-μm MMF, 11% and 22% peak GeO_2 concentration, respectively, are required, assuming a pure fused silica cladding. This results in a peak Raman gain coefficient of 1.2×10^{-13} m/W and 1.7×10^{-13} m/W in 50-μm and 62.5-μm MMF, respectively.

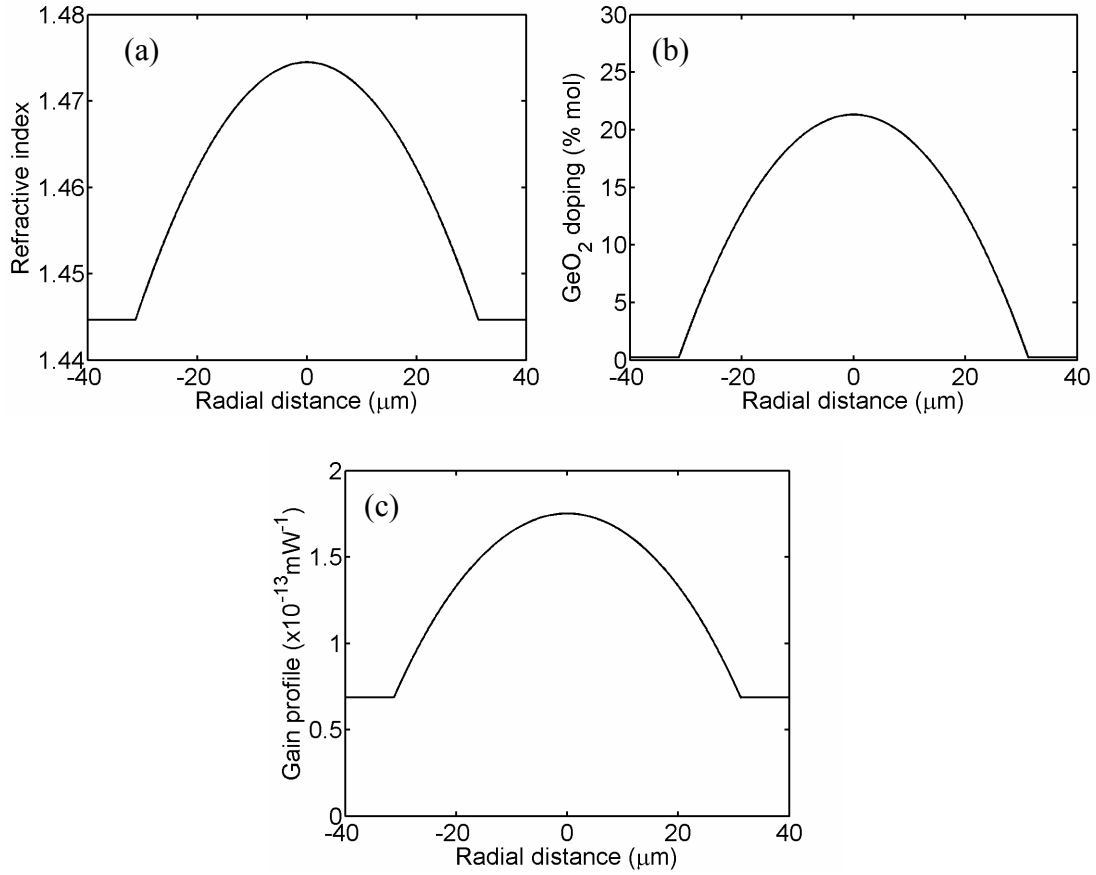

Figure 8. (a) Refractive index, (b) GeO_2 doping density and (c) Raman gain coefficient vs. radial distance for modern 62.5-μm GI-MMF

A comparison of the effective Raman gain of the lowest-order mode in different types of MMF and SMF is done to estimate the efficiency of Raman amplification in MMF. Using Eq. (14) (with g_R=1), the effective area of the lowest order mode (LP_{01}) in MMF is obtained. It is found that effective area in 62.5-μm MMF is less than twice that of SMF and one order of magnitude smaller than step-index MMF of the same radius (Table 1). Interestingly, the larger 62.5-μm fiber has a smaller effective area for LP_{01} than the 50-μm fiber because of the larger index contrast. On the other hand, the on-center Raman gain coefficients are found to be 1.8 and 2.5 times that of pure silica for 50-μm and 62.5-μm MMF, respectively. Thus, for communications-grade MMF, the larger mode area is effectively balanced by the increased Raman gain coefficient.

Table 1. Effective area and peak depolarized Raman gain coefficient for SMF and the LP_{01} pump and signal mode pairs of MMFs.

Fiber	Effective area (μm^2)	Peak Raman gain ($\times 10^{-13}$ m/W)
Standard SMF	85	0.43
62.5-μm GI-MMF	160	0.85
50-μm GI-MMF	187	0.60
50-μm step-index MMF	1311	0.60

A figure of merit for the Raman amplification in fiber is given by the ratio of the effective Raman gain and the pump attenuation coefficient, $FOM = \frac{g_R}{A_{eff}\alpha_p}$. The FOMs of standard SMF, dispersion shifted fiber (DSF), dispersion compensating fiber (DCF)

and the lowest order mode of 50-μm and 62.5-μm MMF are shown in Figure 9. This figure shows that the FOM for the lowest-order mode in 62.5-μm MMF is comparable to that of standard SMF, and it is an equally effective medium for Raman amplification as SMF. However, the FOM for 50-μm MMF is approximately half of that of 62.5-μm MMF and suggests a lower Raman gain.

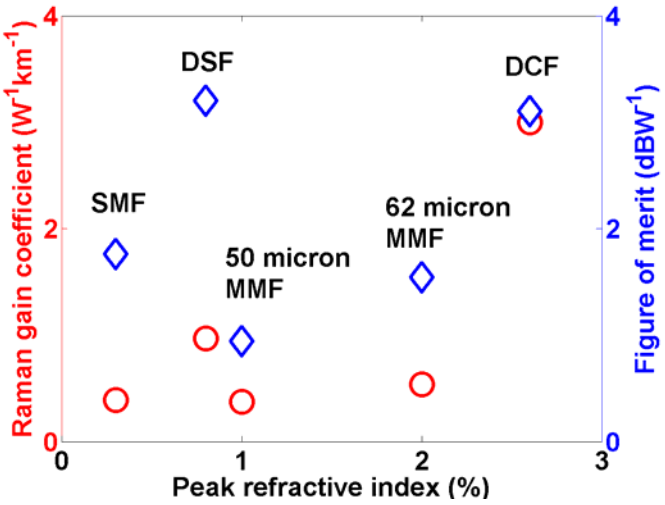

Figure 9. Raman gain coefficient and figure of merit (FOM) vs. peak refractive index for different single mode and multimode fibers.

The HOMs in a MMF have significantly larger effective area and therefore as given by Eq. (14) have a smaller effective Raman gain. Further reduction in the effective Raman gain occurs because of the radial dependence of the Raman gain coefficient. These effects provide the basis for the mode selective gain in MMF.

3.2.3. Mode selective gain

In a nominally center-launch excitation, the lowest-order mode LP_{01} and a few higher-order modes are excited and therefore only those modes take part in Raman

amplification. The effective Raman gain coefficients of the dominant signal and pump mode pairs are shown in Table 2. It is found that the mode selective gain strongly favors the LP_{01} mode. The next strongest pump-signal mode pair, LP_{11}–LP_{11}, has a gain coefficient <74% of the LP_{01} mode and all other mode pairs are less than 50% of the LP_{01}–LP_{01}. The effective Raman gain coefficient for LP_{01} pump and signal modes is ~0.54 $km^{-1}W^{-1}$ and ~0.37 $km^{-1}W^{-1}$ for 62.5-μm and 50-μm MMF, respectively. This is comparable to that reported for standard SMF, 0.4-0.5 $km^{-1}W^{-1}$ and consistent with Table 1. The radial dependence of the Raman coefficient reduces the effective Raman gain of the LP_{03} mode pair by an additional 4%. Higher-order modes have significantly stronger reduction.

Table 2. Effective Raman gain coefficients ($W^{-1}km^{-1}$) for the lowest order pump and signal mode pairs in 62.5-μm MMF.

	Signal modes				
Pump modes	LP_{01}	LP_{02}	LP_{03}	LP_{11}	LP_{12}
LP_{01}	0.56	0.28	0.21	0.28	0.21
LP_{02}	0.28	0.27	0.17	0.13	0.14
LP_{03}	0.21	0.17	0.18	0.10	0.09
LP_{11}	0.27	0.14	0.10	0.41	0.20
LP_{12}	0.20	0.12	0.10	0.20	0.25

3.3. Effect of Raman amplification on MMF impulse response

Raman amplification in communication-grade fiber typically requires long length of link for significant amplification. Impulse response of long MMF links is highly dependent on the modal dispersion and therefore the launch conditions. We demonstrated in the last section that the Raman amplification in MMF provides larger gain for lower order modes and therefore center-launch condition which excites lower order in MMF is preferred for a Raman amplified MMF link.

We numerically simulated the effect of Raman amplification on impulse response of nearly center-launch excited MMF links and also experimentally verified the results using long communication-grade MMF.

3.3.1. Simulation results

Using the results of mode selective Raman amplification, a full channel model of MMF-link is developed to examine the effects on impulse response. A conventional experimental set up for impulse response measurement is numerically simulated. The signal and the depolarized pump are launched into the MMF from a SMF at different offsets from the core-center and co-propagated along the MMF. In the receiver-end the pump is dropped and the signal is measured using a photodetector.

The initial MPD for near center launch conditions (Figure 10a) reveal that LP_{01} is the primary excited mode. Since the LP_{01} has the largest mode power even for slightly off-centered launch conditions, LP_{01} has the largest total gain for near-center-launch conditions, and LP_{01} is strongly selectively amplified. It is noted that the net Raman gain

and the gain of LP_{01} mode gracefully degrades with increasing offset (Figure 10b). This insures the Raman gain is not overly sensitive to the perturbations in the mode power distribution.

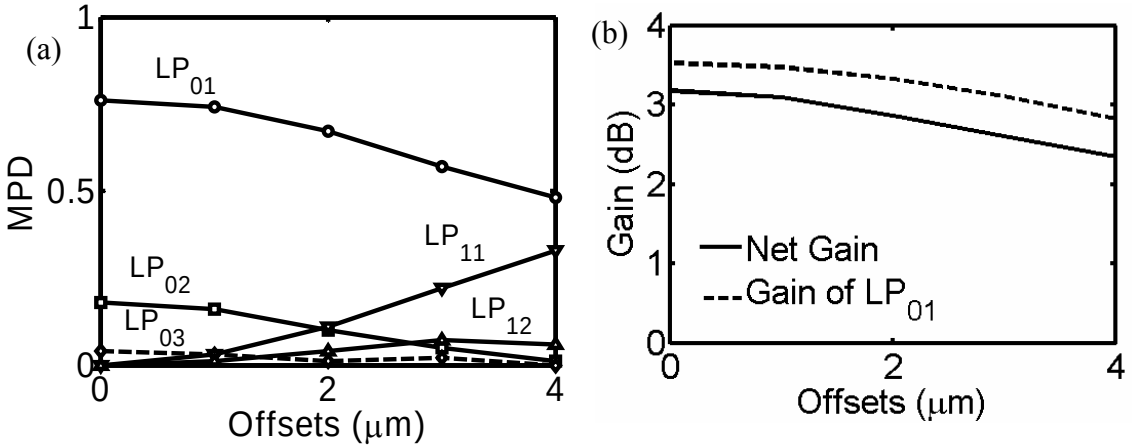

Figure 10. (a) Normalized launch power in lower ordered modes of 62.5-μm MMF for SMF launch at offsets from the core-center. (b) Change in net gain and gain of LP_{01} mode for a pump power of 250 mW

The IPR is computed with and without 200 mW of Raman pump power for 8 km of both 50-μm and 62.5-μm MMF (Figure 11). The computed IPRs clearly demonstrate that the LP_{01} mode is selectively amplified compared to the HOMs.

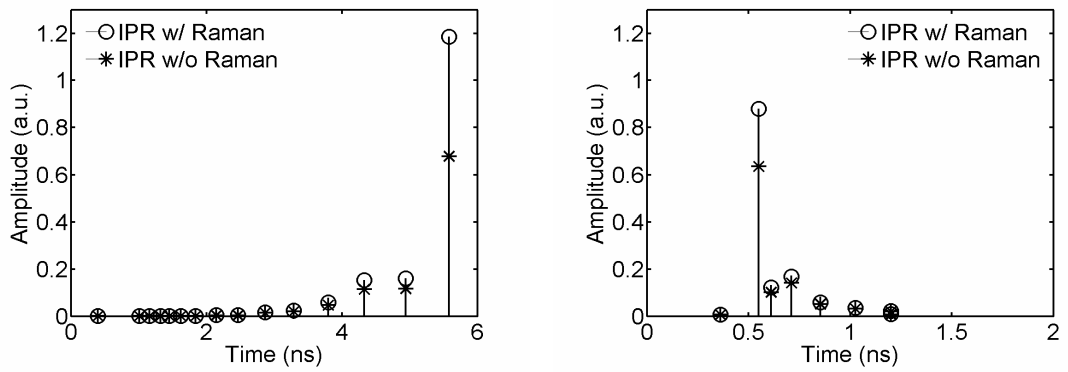

Figure 11. Simulated IPRs of (a) 9-km 62.5-µm MMF and (b) 9-km 50-µm MMF for 3-µm-offset SMF-launch without and with Raman amplification demonstrating the mode selective gain.

3.3.2. Measurement results

Experimentally we examine the simplest implementation; pump and signal launched via the same SMF (Figure 12).

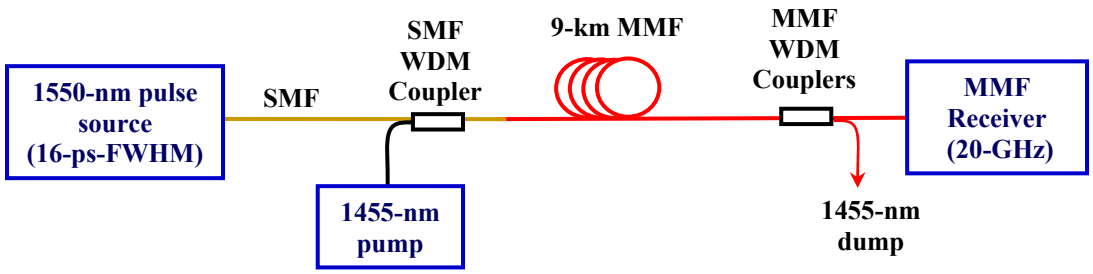

Figure 12. Experimental set up for impulse response measurement of Raman amplified MMF link

The 1550-nm signal is co-propagated together with a depolarized 1455-nm pump. We use modest pump powers of 200 to 250 mW, power that is easily provided by a single pump diode. The signal and pump are multiplexed using a SMF-WDM coupler and

launched together via the SMF at specific offsets (0-4 μm) near the center of the MMF core to simulate typical connector offsets. At the receiver a custom MMF-WDM coupler is used to drop the remnant pump power allowing the signal to be detected using a commercial MMF receiver. For the impulse response measurements, a mode-locked fiber laser is used as a source of 16 ps nearly-transform-limited pulses. Both 50-μm and 62.5-μm fibers with lengths 4.0 km and 9.1 km and with an overfilled-launch-bandwidth of ~2000 MHz-km and 1230 MHz-km respectively are examined.

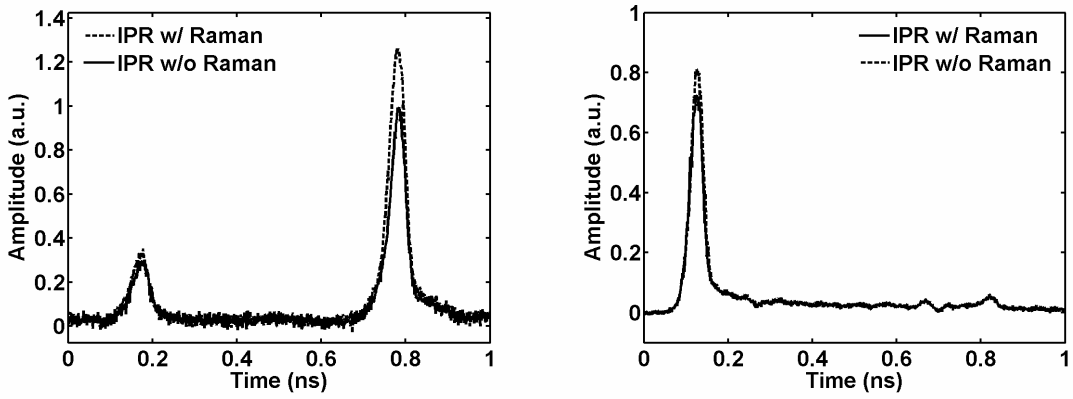

Figure 13. Measured IPRs of (a) 9.1-km 62.5-μm MMF for 3-μm-offset SMF-launch and (b) 4-km 50-μm MMF for ~0-μm-offset SMF-launch without and with Raman amplification demonstrating mode selective gain.

The measured IPRs are shown with and without 200 mW of Raman pump power for 50-μm and 62.5-μm MMF. The gain of the LP_{01} mode as computed from the measured impulse response of Figure 13a accounts for more than 90% of the total signal gain although the LP_{01} mode accounts only for 75% of the initial total launched power. This is consistent with the separately measured total power gain. Both measured and computed IPRs clearly demonstrate that the LP_{01} mode is selectively amplified compared

to the higher order modes. This assessment is made by first identifying the LP_{01} mode and the LP_{11} mode by experimentally observing the behavior of Figure 11a as the offset is scanned.

3.4. Reduction of intersymbol interference via mode selective Raman amplification

Based on the impulse response measurement results mode selective Raman amplification is proposed as an inter-symbol interference (ISI) mitigation method for long MMF links. The method is distinguished from the MMF channel impairment mitigation techniques briefly described in section 2.3, because it is a fully optical method that can be equally exploited for multi-wavelength (CWDM), *long* MMF channel independent of the data rate. It is also noted that the well-known refractive index profile irregularities [6], which alter the differential modal delay (DMD), do not generally alter the Raman gain coefficient or the mode profiles significantly. This makes mode selective Raman amplification in GI-MMF a robust ISI reduction technique independent of the specific DMD.

The experimental set up for a 10Gb/s, multi-km, Raman-amplified MMF-link is similar to the set up used for impulse response measurement with the pulse-source replaced by a 10Gb/s transmitter at 1550 nm. The PRBS 2^{31}-1 NRZ data stream has 40 ps rise time (10-90%) and the MMF detector has 12 GHz bandwidth. Figure 14(a) and (b) show the eye diagram without and with a 250 mW Raman pump respectively. Figure 13(a) reveals that the eye is reduced by significant ISI which is clearly the result of the

deterministic *amplitude* jitter (DAJ) caused by the HOM groups. By comparison of Figure 13(a) and (b) it is clear the Raman gain of the LP_{01} mode increases the eye opening yet does not increase the DAJ i.e. the width of the zeros and ones as would be the case for uniform gain for all modes. This observation is consistent with improvement in IPR.

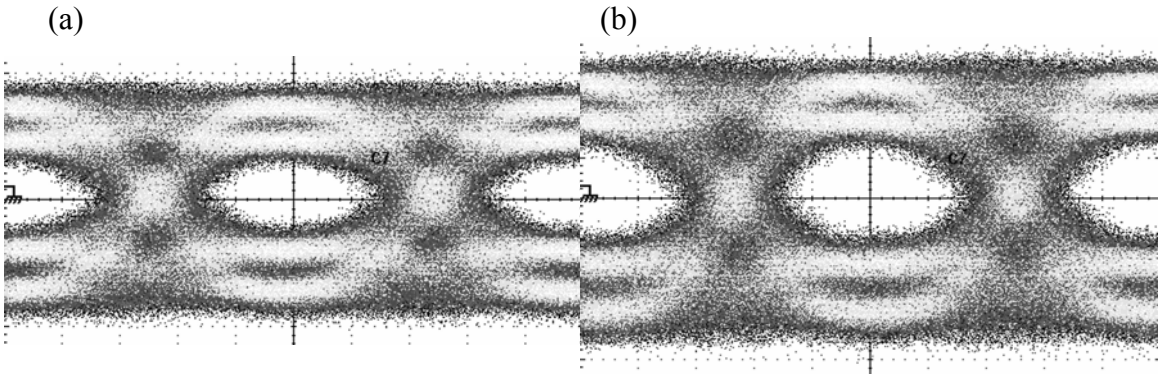

Figure 14. Experimentally measured eye diagram for 10 Gb/s data transmission through 9.1 km of 62.5-μm MMF for 2 μm offset SMF launch without (a) and with (b) 250 mW Raman pump

The ISI reduction is further illustrated by the amplitude probability density obtained in a 20 ps sampling window in the middle of the eye (Figure 15). The similar widths of the measured amplitude probability density (PD) confirms a nearly unchanged DAJ. Furthermore, the nearly parallel tails of the histogram with and without Raman amplification demonstrate negligible added noise due to pump power fluctuation and modal noise in the Raman amplification process.

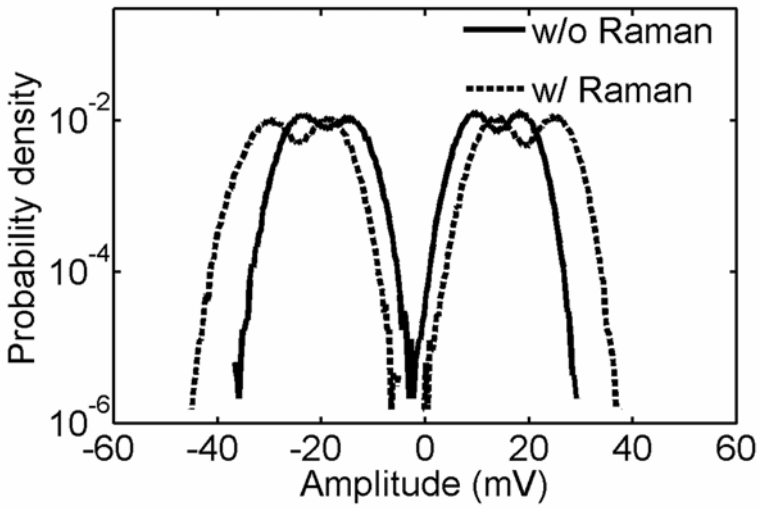

Figure 15. Histogram in 20 ps vertical sampling window at the center of eye demonstrating Q improvement due to mode selective Raman amplification.

The ISI reduction which is 1.4 dB at 250 mW increases with increasing Raman pump. From the experimental results it is estimated that a Raman pump of 750 mW yields >4 dB improvement in the Q factor for offsets as large as 4 μm thus demonstrating the efficacy and robustness of the ISI reduction. Furthermore longer fiber lengths are more effective for exploiting Raman amplification. It is found that link lengths of ~12km at 1550nm provide improved performance.

3.5. Summary

Raman amplification in glass GI-MMF is extensively explored numerically and mode selective Raman amplification is demonstrated. It is shown that the gain of the lowest order mode in communications grade GI-MMF is comparable to that found in

SMF and the importance of a graded index on mode selective Raman amplification in MMF is demonstrated. The first use of mode selective gain in communication links to reduce ISI in multi-km 10-Gb/s MMF links is also demonstrated. The ISI improvement is independent of DMD and bit rate and hence is equally available for higher data-rates and multi-wavelength applications.

CHAPTER IV

PLASTIC OPTICAL FIBER BANDWIDTH

4.1. Introduction

In this dissertation, plastic optical fiber is investigated as a medium for high-performance, short-reach links primarily because of the termination and the alignment tolerance benefits of these fibers. However, the effectiveness of the POF in a high-speed link is dependent on the available bandwidth. We know that in the case of the glass-MMF, the bandwidth of is dependent on the core size and the refractive index profile of the MMF as well as the launch conditions and the wavelength of the optical signal. Therefore it is necessary to quantitatively investigate the effect of these parameters on the bandwidth of the POF.

In this chapter we first provide a brief introduction to the state-of-the-art in plastic optical fiber including some of the basic properties of it. Then we characterize the bandwidth and temporal response of POF via numerical simulation using the comprehensive MMF model described earlier. The effect of mode coupling and refractive index variations are explored quantitatively explored. The numerical results are followed by the experimental evaluations of the temporal response of the POF. After the medium is the characterized, we also explore the capacity of the POF links including the transceiver bandwidth limitation to support data rates of 40 Gb/s.

4.2. Plastic optical fiber basics

In the following subsections the availability and typical applications of commercial POFs are presented followed by some of the important properties of POF. Finally a comparison between glass-MMF and POF is performed to evaluate the trade-off in the design of low-cost, short-reach links.

4.2.1. Availability and applications

Until recently, the commercially available POF were mostly PMMA (polymethyl methacrylate)-based step-index POF. The large attenuation in PMMA-POFs limited the link lengths to <50 m while the large dispersion limited the data rate to 100 Mb/s. These links found use in low-performance applications, such as automotive industry. Media Oriented Systems Transport (MOST) is a European standard that supports 100-500 Mb/s over 1 mm core POFs for interconnects in automobiles.

The next generation of POF is an amorphous perfluorinated polymer (polyperfluoro-butenylvinylether) –based GI-POF. In 1997, GI-PF-POFs with one-third loss of PMMA-POF was developed at Asahi Glass. These GI-PF-POFs became commercially available from Chromis Fiberoptics since 2005. The experimental demonstrations in this dissertation are performed on GI-PF-POFs from Chromis Fiberoptics.

A few of the representative commercially-available POFs including their vendor-specified specifications is listed in Table 3. The significant difference in the core sizes and attenuation of the PF and PMMA based POF makes PF-POF the medium of choice for high-performance links.

Table 3 Available commercial POFs

Vendor/ Product	Chromis/ GigaPOF 50SR	Chromis/ GigaPOF 120SR	Asahi Glass/ Lucina	Optimedia/-	Mitsubishi/ -
Type/ Material	GI-PF	GI-PF	GI-PF	GI-PMMA	SI-PMMA
Numerical Aperture	0.19 +/- 0.015	0.185 +/- 0.015	0.185 +/-0.01	0.23-0.3	0.5
Core/ Cladding Diameter (μm)	50/490 +/- 5	120/490 +/- 10/7	120/492 +/- 10/3	1000/2200 +/- 5%	980/1000 +/- 60
Attenuation (dB/km) @850nm	<50	<60	<40	<200	<200
@ 1300nm	<60	<160	---	<4000	<4000
Bend Loss* (dB)	<0.35	<0.6	---	---	---
Bandwidth	>300MHz-km @850nm	>300MHz-km @850nm	>940MHz x200m @850nm	Dependent on NA	--

*Bend loss measured after 10 turns over 25mm radius quarter circle

4.2.2. Attenuation

Both PF and PMMA based plastic optical fiber has significantly larger attenuation compared to glass-MMF. In the case of PMMA-based fiber the high attenuation is attributed primarily to the Rayleigh scattering of light in the fiber core [27]. However, in recent years Polymethyl Methacrylate (PMMA)-based POF with attenuation <200 dB/km in 550-700 nm wavelength [28] has been developed.

Pererfluorinated POF with <50 dB/km attenuation in the 700-1400 nm wavelength [30] has been developed. Like PMMA-POF, the primary reason for the loss in PF-POF is Rayleigh scattering. A theoretical lower limit of attenuation in PF-POF made from poly-perfluorobutenylvinylether (PBVE) in the 850 nm wavelength has been found to be 10 dB/km. Thus, with further improvements in the manufacturing process, PF-POF with

even lower loss is expected. Figure 16 shows the attenuation vs. wavelength of GI-PF-POFs manufactured by Chromis Fiberoptics.

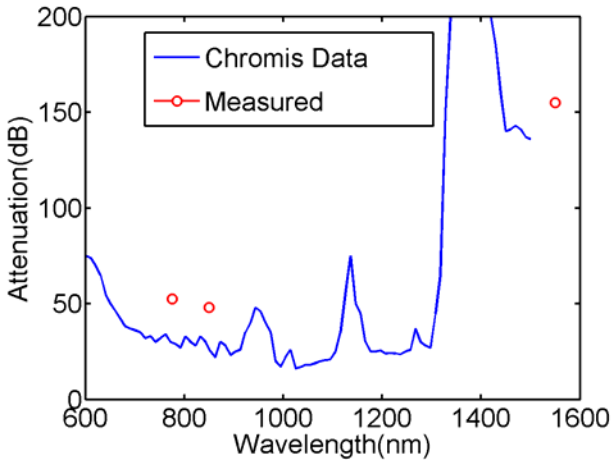

Figure 16. Attenuation vs. wavelength for the new generation of GI-PF-POF from Chromis fiber optics. The measured values include the coupling loss at the transmitter and receiver.

4.2.3. Reported performance

Link demonstrations using POF has been reported in the literature. Table 4 [31] provides an overview of recent link performance with various types of POF. The fiber types are PMMA-based step-index POF (PMMA-SI-POF), PMMA-based GI-POF (PMMA-GI-POF) and GI-PF-POF. The laser sources used are Fabry-Perot (FP), Distributed Feedback (DFB), and VCSEL. The PMMA-POF links are primarily demonstrated at relatively shorter wavelength regimes compared to the PF-POFs. Transmission at high data rates (~10 Gb/s) are performed for relatively smaller core POFs i.e. 130 μm diameter compared to 1 mm of conventional POFs. In the current research, obviously we have focused on the relatively smaller core PF-POFs.

Table 4 POF-based data transmission experiments

Fiber type	Core diameter (μm)	Bit rate (Gb/s)	Distance (m)	Laser	Wavelength (nm)
PMMA-SI-POF	1000	0.5	100	FP	650
PMMA-SI-POF	1000	1.0	15	VCSEL	780
PMMA-SI-POF	120	2.5	2.5	VCSEL	835
[32] PMMA-GI-POF	500	2.5	200	FP	645
GI-PF-POF	170	2.5	300	FP	645
GI-PF-POF	130	2.5	550	VCSEL	840
GI-PF-POF	130	2.5	550	DFB	1310
GI-PF-POF	130	9.0	100	VCSEL	830
GI-PF-POF	155	7.0	80	VCSEL	935
[33] GI-PF-POF	130	11.0	100	FP	1300

4.2.4. Mode coupling

Two different phenomena influence the bandwidth of POF significantly – intermodal dispersion and mode coupling. POF exhibits more bandwidth than is expected from a DMD computation using the refractive index profile. To explain this bandwidth enhancement, mode coupling and differential modal attenuation (DMA) have been proposed [34][35][36]. The presence of strong mode coupling in POF was concluded from two observations: a) significant change in the MPD after propagating through the POF (section 2.2.5) and b) temporal measurement showing pulse broadening (σ) proportional to approximately the square root of the fiber length (L). The measurements were performed on a PMMA-based SI-POF with core diameter of 1 mm [37] and

PMMA-based GI-POF with core diameter of 0.5 mm yielding 3 GHz bandwidth from 100 m fiber length [34]. The estimated mode coupling length for these fibers was reported to be of the order of 15-30 m. Similar measurements performed on a 140 μm core GI-PF-POF with 60 dB/km loss showed $\sigma \propto L^{0.57}$ [35]. Moreover, DMD measurements showed a Gaussian-like response for all offsets, suggesting strong mode coupling. In [38], following a detailed modeling and measurements involving a far-field radiation pattern, it was concluded that mode coupling is the primary reason for the enhanced bandwidth in GI-PF-POF, and the mode coupling length is of the order of 20-100 m.

However, complete characterization of a GI-POF using a comprehensive channel model is required to explain the bandwidth properties quantitatively. A detailed exploration of the parameter space, including core diameter, refractive index profile is also necessary to optimize the GI-MMF for the best performance.

4.2.5. Comparison between the glass and plastic MMFs

Until recently, MMF has essentially been referred to *glass*-MMF. However, with the advances in POF manufacturing technology and the realization of the potential of POF, both glass- and plastic- MMF are being considered with equal importance.

Table 5 provides a comparison of the strength and drawbacks of both types of MMFs. They both provide the fundamental advantages of a large-core fiber. However, there are certain differences in their properties arising because of the difference in the material used and the manufacturing process. The best solution and the choice of the fiber should necessarily be guided by the application and the demand from the link.

Table 5. Comparison of typical properties of glass MMF and POF

Typical properties	Glass MMF	POF
Core size	➢ Typically 50 and 62.5 μm ➢ Standardized by the industry	➢ 500-1000μm (PMMA-POF) ➢ 50-150μm (PF-POF) ➢ Not standardized yet
Attenuation	➢ <3 dB/km @ 850 nm ➢ <1 dB/km @ 1300 nm	➢ 150-200 dB/km (PMMA-POF) ➢ 30-50 dB/km (PF-POF)
Transmission window	➢ 800 – 1600 nm	➢ 550 – 700 nm (PMMA-POF) ➢ 750 – 1350 nm (PF-POF)
Mode coupling	➢ Mild	➢ Strong
Intermodal dispersion (ps/m)	➢ Varies widely depending on the generation of fiber ➢ ~2 ps/m for FDDI-grade GI-MMF ➢ ~0.5 ps/m for modern OM3 MMF	➢ Not directly measurable due to mode coupling effects
Typical bandwidth and link length	➢ Bandwidth×distance limited by intermodal dispersion ➢ 500 MHz-km for FDDI-grade GI-MMF ➢ 2000 MHz-km for OM3 MMF	➢ Bandwidth×distance limited by intermodal dispersion and mode coupling ➢ Link length also limited by attenuation ➢ 4 Gb/s transmission over 300 m of PMMA-POF is reported ➢ 11 Gb/s over 100 m of GI-PF-POF is reported
Connectorization	➢ Special connectors/patchcords ➢ Splicing requires special cutting and connecting tools	➢ Butt coupling or crimp on ➢ Easy, requires little training or special tools
Application	➢ Access network, Ethernet	➢ Access network, Ethernet
Component and system cost	➢ Lower compared to SMF	➢ Potentially lower compared to glass-MMF

4.3. Bandwidth of plastic optical fiber links: Numerical evaluations

Considering the link perspective, it is always essential to have a numerical model that provides a description of a channel which is accurate enough for the data transmission rate of the link. In the case of glass-MMF links, appropriate numerical models of glass-MMF had been adopted for Gigabit Ethernet and 10 Gigabit Ethernet standards. Similarly, an accurate numerical model for POF is essential for high-speed links using POF. The MMF model described in section 2.4 incorporates all the primary physical properties of POF and is accurate enough for high-data-rate POF links. Apart from yielding accurate estimate of the temporal response of the POF link, the physical model also provides spatial responses and insightful connections with the physical properties of the fiber.

4.3.1. Evolution of POF temporal and spatial response

A comprehensive numerical analysis using the MMF-model described in section 2.4 is performed to investigate the combined effect of inter-modal dispersion and mode coupling phenomena on the temporal response of GI-POF. The numerical model also provides the evolution of MPD which is indicative of the emission angle of MMF output and can be directly compared with the far-field measurement results described in section 4.2.4.

The input parameters to the model are refractive index profile, wavelength of operation and mode coupling strength A. The general conclusions obtained from the numerical analysis are applicable to any GI-MMF. However, the specific values of the

parameters are characteristic of GI-PF-POF.

The refractive index profiles used have a core-cladding index-delta (Δ) of 1.5% and a cladding-index of 1.34, corresponding to GI-PF-POF. The refractive index profiles that are investigated are:

a) Pure α-profiles with α ranging from 1.8 to 2.2.

b) Mixed α profiles where the α varies across the radius i.e $\alpha = \begin{cases} \alpha_1 \text{ for } r < a/2 \\ \alpha_2 \text{ for } r > a/2 \end{cases}$.

   Here α_1 and α_2 ranges from 1.8 to 2.2.

c) Profiles with irregularities known to result in severe DMD in glass-MMF; center peak and center dip (with α = 2) [6]. The center dip and center peak have an index deviation 12% of Δ.

To demonstrate the temporal behavior and evolution of MPD in GI-POF, a situation similar to the DMD measurement (section 2.2.1) is numerically simulated. Thus, the initial MPD is obtained for the 7-μm-FWHM Gaussian excitation corresponding to SMF-launch at different offsets from the center of the MMF core. The MCC is varied over a wide range from 0.01 to 1000 m^{-1} and the corresponding MCLs are computed. It is assumed that the highest order mode group has the highest coupling to leaky modes and that is simulated by applying a DMA for the highest order mode group. The effect of DMA is explored for 0, 0.3, 3 dB/m.

4.3.2. Effect of mode coupling

Figure 17 demonstrates the evolution of DMD under mode coupling in a GI-POF. The DMD is computed for three MCLs correspondin

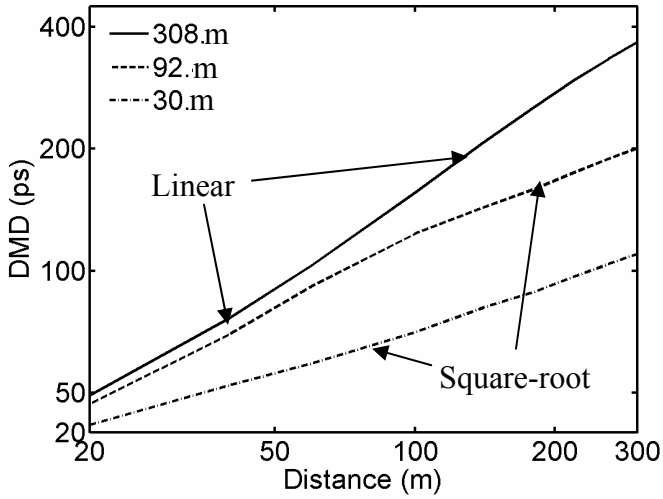

Figure 17. Evolution of DMD with fiber length for different MCLs. For relatively long MCL (308 m), the DMD remains linear with fiber length up to 300 m. For relatively small MCL (30 m), the DMD becomes proportional to the square-root of the fiber length after 30-40 m. For an intermediate MCL (92 m), the DMD changes from being linear to square-root at ~100 m.

Figure 18 summarizes the effects of mode coupling on the temporal response and mode power distribution of 200-m, 50-μm GI-POF (α = 2.1). At 850 nm wavelength, 16-ps-FWHM pulses are launched at different offsets. The lowest depicted mode coupling of 1.7×10^{-4} m^{-1} corresponds to that found in glass-MMF (section 2.5). On the other hand, the highest coupling of 5 m^{-1} corresponds to an MCL of 30 m, and is consistent with that reported for GI-POF which ranges between 2 to 100 m [34][35][37].

An intermediate MCC of 0.17 m^{-1} is chosen to illustrate the transition between weak and strong coupling.

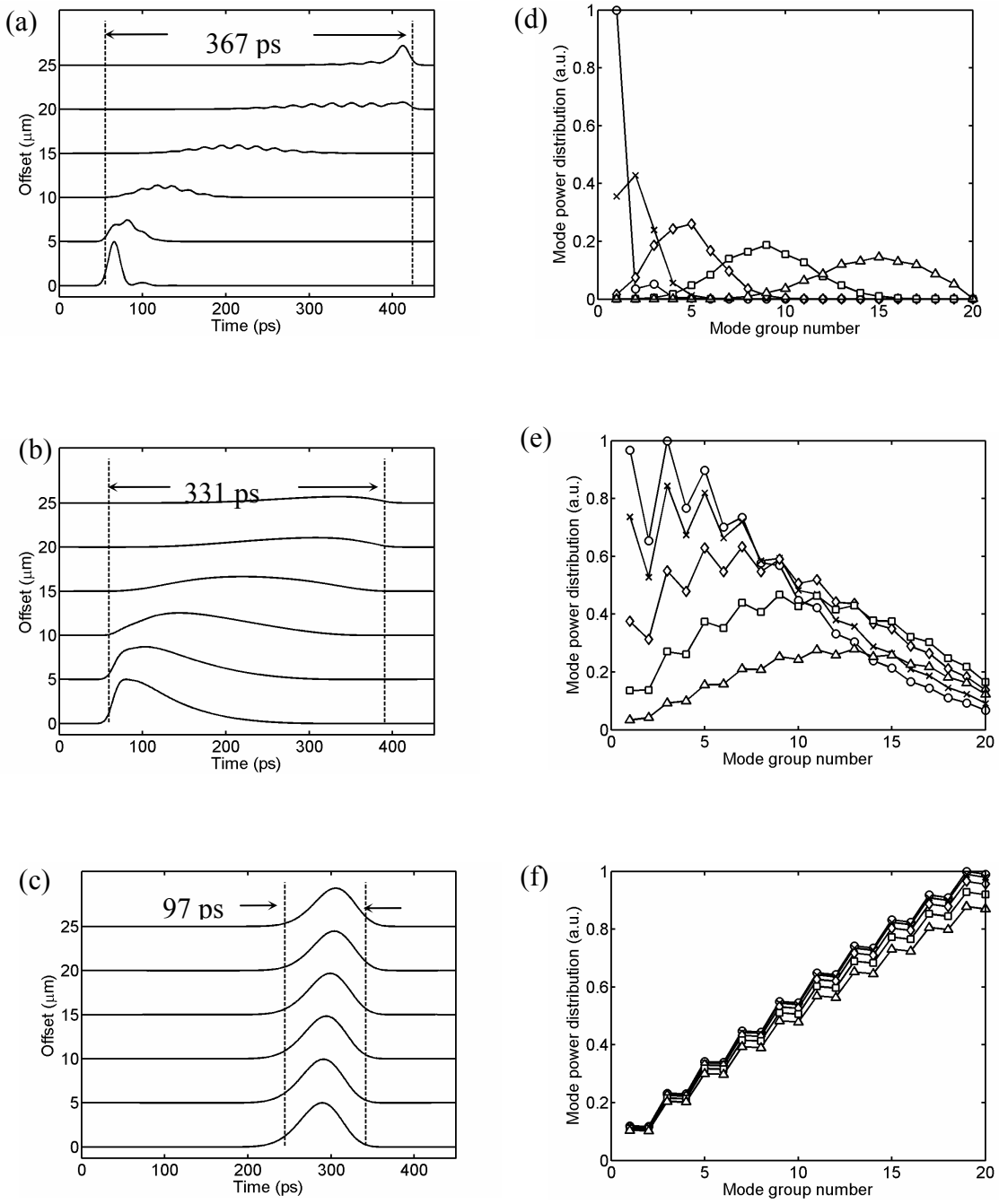

Figure 18. DMD simulation for 200-m GI-POF with average mode coupling coefficients of 1.7×10^{-4}, 0.17 and 5 m^{-1} (a, b and c respectively). Corresponding MPD (d, e, f) vs. mode group number for launch offsets of 0 μm - open circles, 5 μm - ×'s, 10 μm - diamonds, 15 μm - squares and 20 μm – triangles.

The temporal response changes dramatically with increasing mode coupling (Figure 18 a, b and c). In the absence of significant mode coupling (Figure 18 a) the non-optimal refractive index profile ($\alpha = 2.1$) yields a DMD of 367 ps. It is noted that this is close to the maximum DMD of 2 ns/km allowed in FDDI grade glass MMF and only supports 10 Gb/s with a restricted mode launch. As the MCC is increased to 0.17 m^{-1}, energy transfer among the mode groups first fills the valleys between the discrete mode groups and then increases the width of the response at a particular offset although the DMD of 331 ps is reduced slightly. Increasing the MCC to 5 m^{-1} with corresponding MCL of 30 m, reduces the DMD to 97 ps. The individual offset responses are also reduced compared to intermediate coupling (Figure 18 c).

As expected for small coupling, the MPDs at the receive-end remain dependant on launch condition (Figure 18 d) and are essentially the same as those at the launch. Of course, the leaky mode group loses power, and there is somewhat less power in the HOMs in general. For strong coupling (Figure 18 f) all launch-offsets yield similar near equilibrium MPDs after 200 m. The equilibrium MPD is equal power in all modes (not mode groups) and therefore, the increase in power with mode group number reflects the increasing degeneracy with increasing mode group number. Furthermore the included DMA of 0.3 dB/m does not appreciably reduce the power in the leaky mode. The intermediate MCC case (Figure 18 e) reveals a range of MPDs as the offset is changed and the emission angle of light at the receive-end depends on the launch condition. Experimentally it is challenging to distinguish between the MPDs beyond the intermediate coupling regime. This may account for the range of MCL that have been reported.

4.3.3. Effect of differential modal attenuation

The effect of DMA on DMD is examined since high DMA may also limit DMD by shedding power for modes with large relative delay. A range of DMA of 0, 0.3, 3 dB/m is explored. A DMA of 0.3 dB/m for the highest mode group produces the net loss of 7 dB which is close to the modal attenuation of 200 m GI-POF. Figure 19 shows that changing the DMA does not appreciably change the DMD and confirms that the mode coupling is the primary factor in enhancing the bandwidth of POF. However net loss scales linearly with the attenuation rate of the leaky modes.

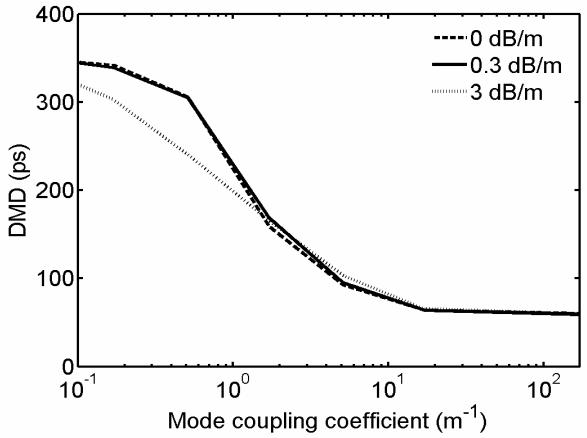

Figure 19. DMD vs mode coupling for different attenuation rate of the leaky mode for 200 m 50-μm POF with $\alpha = 2.1$

4.3.4. Effect of refractive index accuracy

GI-PF-POF has a large transmission window from 700 to 1400 nm. Therefore, similar DMD simulation is performed at 1310 nm at two mode coupling coefficients 0.34

km^{-1} and 6.8 m^{-1} corresponding to glass MMF and PF-POF respectively. Figure 20 shows the computed total DMD (defined in 2.2.1) vs. the power law coefficient α of the graded index profile. The low coupling case reproduces the standard glass-MMF behavior which requires very precise α to obtain small DMD when many modes are excited. In contrast, the strong coupling of the POF allows a DMD of <50 ps/200 m to be achieved for a large range of α; ±0.05 with respect to optimum. It is noted that for low coupling the impulse response is comprised of distinct mode groups. For strong coupling the response is nearly Gaussian, which has a FWHM that is approximately half that of the 25% DMD metric. Thus, as indicated in Figure 20, the POF supports 40 Gb/s for a DMD of ~50 ps. Clearly, 200 m of GI-PF-POF is capable of supporting 40 Gb/s transmission for any launch condition.

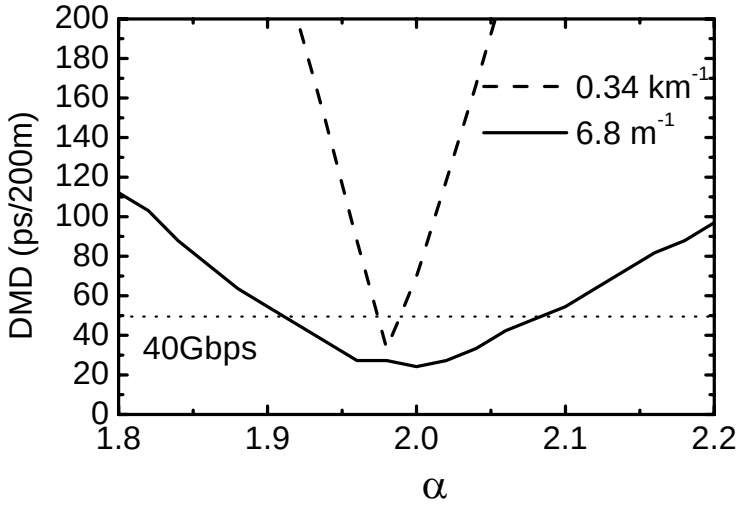

Figure 20. DMD vs. refractive index profile α parameter for two mode coupling coefficients.

The DMDs for other profile irregularities are summarized in Figure 21. Although the MPD varies only slightly among the different fibers the temporal response is strongly

dependent on the index profile and the DMD varies considerably. The effect of MCC on DMD has a near threshold-like behavior. An MCC below 0.2 m^{-1} has a little practical impact on DMD yet the near minimum DMD is reached with an MCC of ~10 m^{-1} or greater. Strong coupling substantially reduces the DMD for all index irregularities.

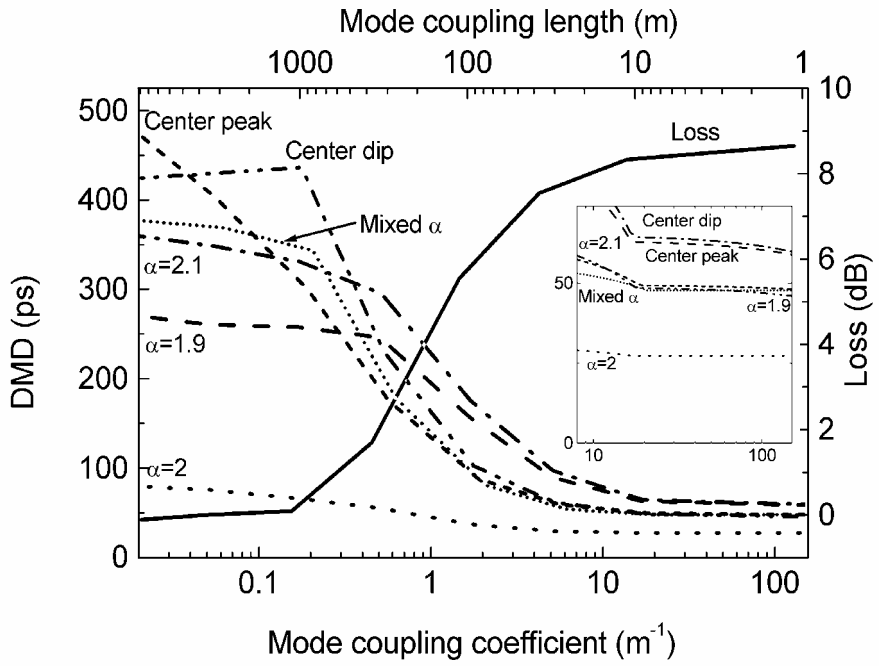

Figure 21. DMD vs. mode coupling coefficient for 200 m 50-μm POFs with different refractive index profiles. Loss vs. mode coupling coefficient (solid). Inset depicts DMD details at high coupling.

The MCC depends on the mode coupling strength *A* and the transverse mode profile. It is found that the MCC for a given *A* varies only slightly for the index irregularities considered here. This relative insensitivity results from the insensitivity of the transverse mode profiles to the index profile irregularities in contrast to the mode group delays. It is also found that the MCLs corresponding to an average MCC are similar for different

index profiles. Therefore the coupling length scale in Figure 21 is accurate for all fibers independent of index irregularity.

It is evident from Figure 20 and inset of Figure 21 (strong mode coupling limit) that although mode coupling reduces DMD, the resultant DMD remains dependent on the index profile for all coupling strengths. The model also demonstrates, that DMD increases approximately linearly up to coupling length L_c, and the DMD τ at length L ($L>L_c$) is given by $\tau = \tau_c \left(L / L_c \right)^{1/2}$, where τ_c is the DMD at L_c. This result captures the dependence on both the coupling and the index profile. Optimum performance is obtained by the combination of well behaved index profiles and strong mode coupling.

4.3.5. Link simulation: 40 Gb/s transmission over POF

The DMD of 50 μm core GI-POF suggested that 40 Gb/s transmission over 100 m of POF links is achievable. However, a full channel simulation is required to quantitatively estimate the effect of POF link performance at a data rate of 40 Gb/s.

Figure 22 shows the simulation set up for the analysis of 40 Gb/s link performance using GI-POF. The transmitter generates NRZ pulses for 40 Gb/s data rate with a rise time of 8 ps. The receiver is comprised of a square-law detector followed by a 4th order Bessel-Thomson low pass filter with a bandwidth of 35 GHz. The response of GI-POF is generated from the numerically created impulse responses for a DMD simulation. The launch condition is assumed to be a particularly stressed one where the POF responses for different offsets in the DMD simulation are equally weighted to create a cumulative response of the POF link.

The metric used for the evaluation of link performance is the power penalty. The power penalty is defined as the excess optical power (in dB, written as dBo) required for the POF link compared to the back-to-back for the data transmission at 40 Gb/s and a BER of 10^{-12}.

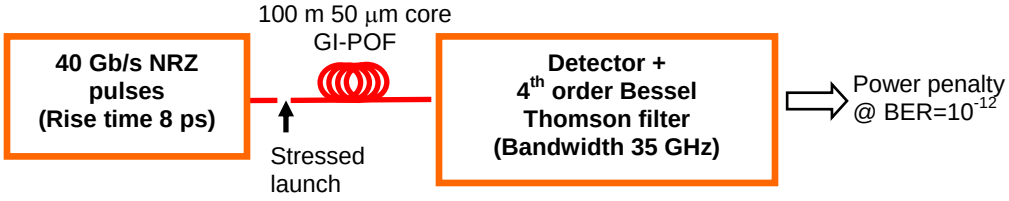

Figure 22. 40 Gb/s POF link for numerical simulation

The link simulation is performed for a variety of GI-MMFs with different MCC and α. The MCCs chosen are 'no coupling', 0.7 m^{-1}, and 6.8 m^{-1} which are representatives of glass-MMF, GI-POF with low mode coupling, and GI-POF with typical mode coupling respectively. For these three MCCs, the index α is varied from 1.85 to 2.15. Figure 23 shows the power penalty vs. α for the three mode coupling coefficients. This shows that for an optimum refractive index profile ($\alpha \approx 1.97$), 40 Gb/s transmission over 100 m is achievable with nominal (<1 dBo) for all GI-POFs independent of mode coupling strength. However, increasing mode coupling strength increases the range of α over which 40 Gb/s performance is achievable. For the typical mode coupling strength of POF, 40 Gb/s with power penalty <2 dBo is achieved for $\alpha = \pm 0.075$ around the optimum. Thus, strong mode coupling in GI-MMF enables the achievement of 40 Gb/s performance with much relaxed tolerance to refractive index profile. This indicates that

such performance can be achieved in GI-PF-POF with high yield once the abovementioned accuracy in refractive index profile becomes possible.

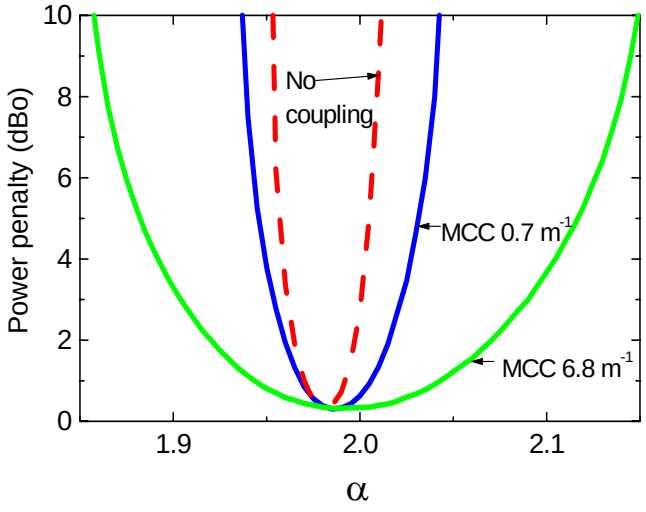

Figure 23. Power penalty for 40 Gb/s, 100 m GI-POF link vs. α of the GI-POF

4.4. POF temporal response: Experimental evaluation

We performed extensive experimental measurements to characterize the temporal responses of POF.

4.4.1. Differential modal delay measurement set up

Using a high dynamic range, high temporal resolution fiber response measurement set up, shown in Figure 24, the impulse response and DMD of GI-PF-POF are examined. A Ti:Sapphire laser source is used to generate 15-ps pulses near 845 nm. The laser output is coupled into an SMF (single mode at 800 nm) using a lens arrangement and

subsequently butt-coupled into the POF. The POF output is collected using a 62.5 μm glass MMF patchcord and is coupled to a 50-μm glass-MMF pigtail of a commercial photodetector with 18 ps FWHM. The response is captured using a fast (70+ GHz bandwidth) digital sampling oscilloscope (Tektronix-TDS8200) with low jitter (< 1 ps). Using a 10 dB splitter, part of the signal from SMF is sampled for power monitoring and trigger signal generation for the scope. For the DMD measurements the launch-fiber is scanned using an automated precision mechanical stage in an X-Y grid of uniform spacing.

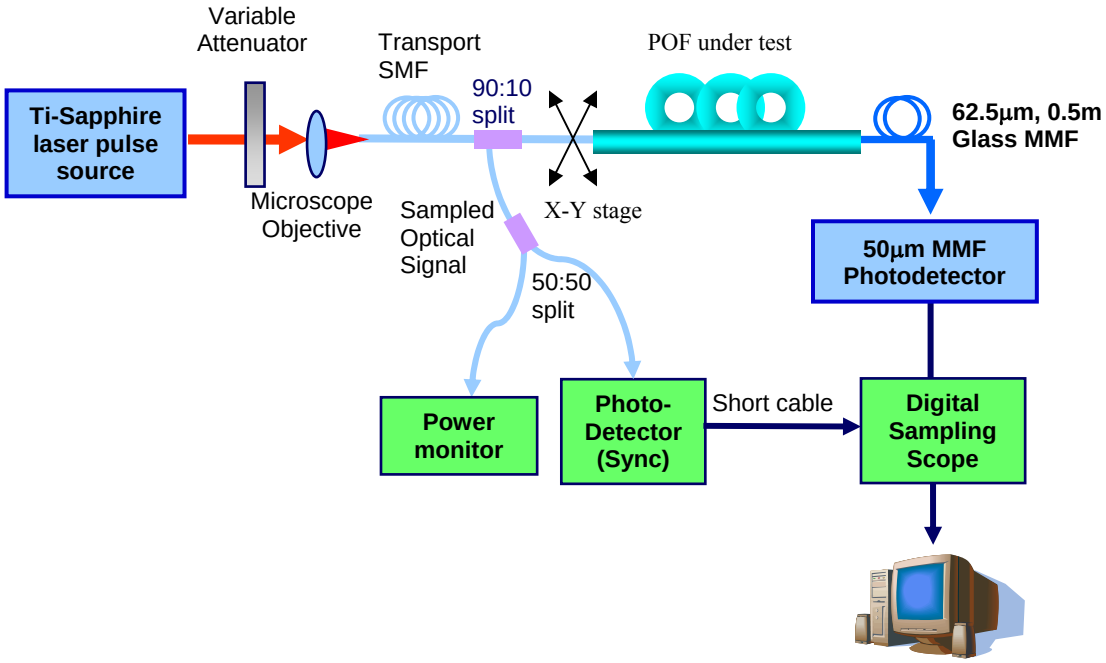

Figure 24. DMD measurement set up for POF

4.4.2. Impulse response

The fiber examined is a 50 μm core with 490 μm cladding, GI-PF-POF from Chromis Fiberoptics (Giga-POF-50SR), with a numerical aperture of 0.19. Figure 25 shows the POF impulse response to a center launch condition and reveals that there is very little structure in the impulse response.

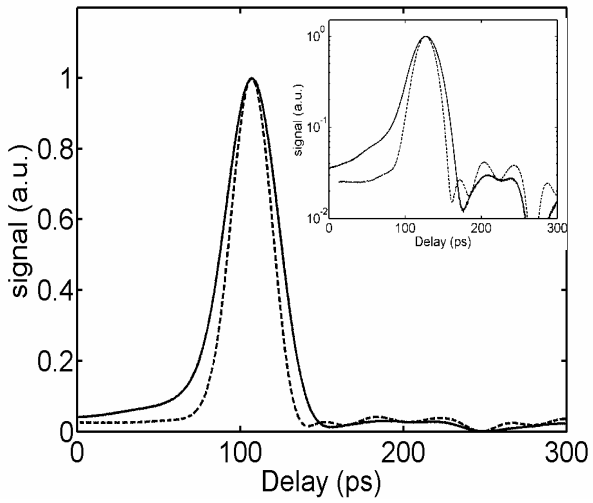

Figure 25. Impulse response at 800 nm after transmission through 200 m of GI POF, inset is a log plot of the same. Dotted curve represents the reference pulse.

The 200 m fiber reveals small broadening in the trailing edge of the response but an otherwise Gaussian like response. This is consistent with the strong mode coupling regime. The arrival of the distinct mode groups can be observed in such an arrangement when examining glass-MMFs of similar length (Figure 26).

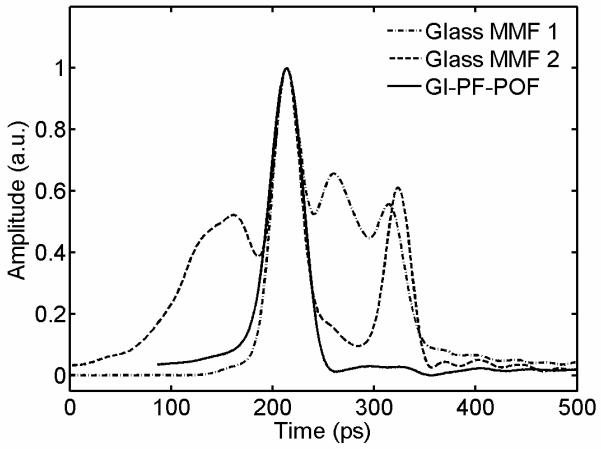

Figure 26. Comparison of impulse response of 200 m GI-PF-POF with that of 220 m of typical FDDI grade glass-MMF. The IPRs are time-aligned and amplitude-normalized for the main peak.

Figure 27 shows the deconvolved response for the 200 m POF. The FWHM in this case is 29 ps, consistent with the simple estimate. The inset shows the frequency response for this same fiber and the reference system response. Although these estimates are still limited by our inherent system bandwidth, it is clear that 200 m of POF can easily support data rates >20 Gb/s. Furthermore, 40 Gb/s is possible with a modest penalty.

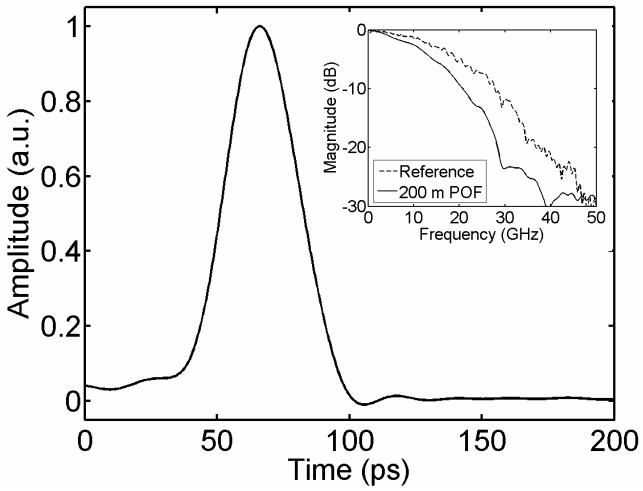

Figure 27. Deconvolved response of 200 m POF showing a 29 ps FWHM. Inset: Corresponding frequency response.

4.4.3. Differential modal delay: 62 μm core GI-PF-POF

We performed DMD measurements of multiple samples of 100 m, 200 m, and 300 m of 62 μm core GI-PF-POFs. The transmit SMF is scanned for X and Y offsets with grid spacing of 5 μm. Figure 28 shows the typical DMD behavior of 62 mm core GI-PF-POF with lengths 100 m, 200 m, 300 m having DMD value of 39 ps, 54 ps, and 95 ps respectively. The DMD plot is the conventional DMD plot for all Y offsets superimposed. DMD metric is defined in section 2.2.1. We note that the impulse responses of GI-PF-POF are independent of launch position and the relative delay at high offsets is very small, <10ps for even 300 m of POF length. This DMD behavior is consistent with simulated DMD in the strong mode coupling regime (Figure 18 c) and shows the bandwidth of the POF to be nearly independent of the launch conditions. Also, it is noted that the signal is attenuated when launched at high offsets. This is indicative of enhanced loss of the HOMs which are coupled to strongly attenuated cladding modes.

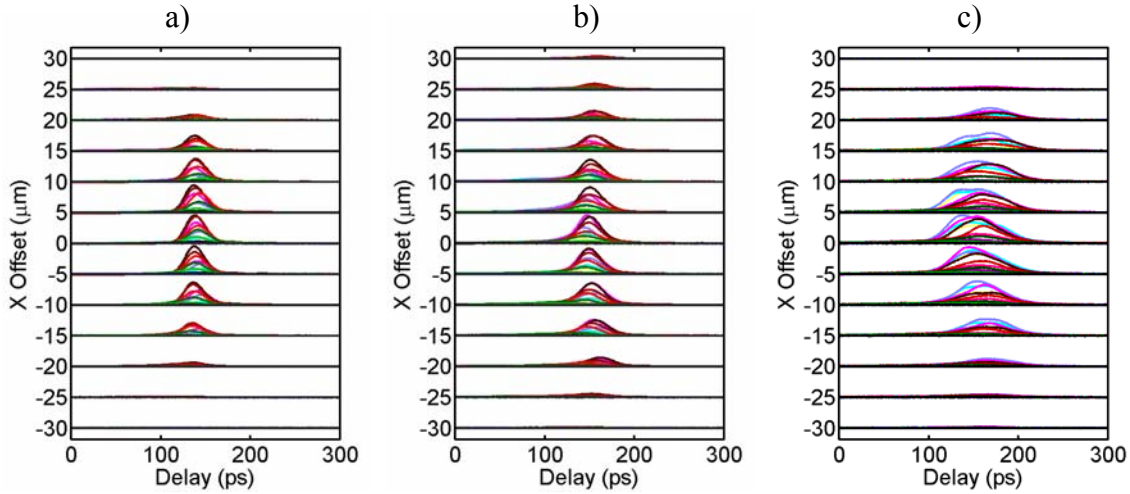

Figure 28. Measured DMD of 62 μm core GI-PF-POF: a) 39 ps over 100 m b) 54 ps over 200 m c) 95 ps over 300 m

4.4.4. Differential modal delay: 120 μm core GI-PF-POF

The large core 120 μm core GI-PF-POF is a potential medium for low-cost, short reach links because it provides the benefits of the standard MMF links to a greater extent. We characterized large 120 μm core GI-PF-POF by performing DMD measurements. Since the light from a 120 μm is only partially collected using a 62 μm glass-MMF, a receive-side scan is performed to measure the contribution from different modes. For the sake of time-efficiency, the transmitter is scanned in a X-Y stripe of 10 μm spacing and the receive-MMF is scanned across the diameter with a 15 μm spacing. Figure 29 shows DMD behavior of 120 μm core GI-PF-POF with lengths of 100 m, 200 m, and 300 m having DMD value of 38 ps, 71 ps, and 95 ps respectively. The DMD is plotted for different Y offsets and receiver positions superimposed. The DMD of 120 μm core GI-PF-POF exhibits the same features as 62 μm core GI-PF-POF i.e. the large bandwidth and launch-insensitivity. It is also noted that the bandwidth of large 120 μm core GI-PF-POF is sufficient to support 10 Gb/s over 200 m links.

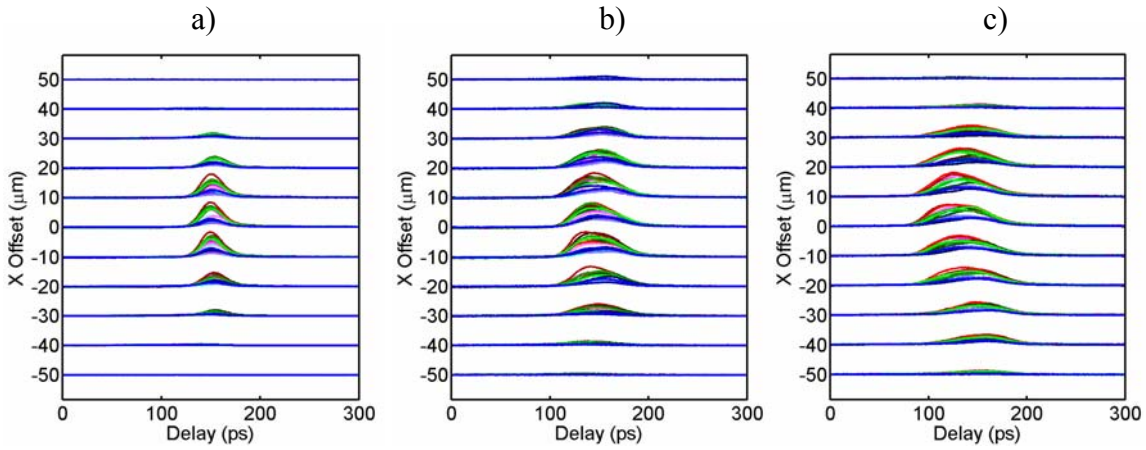

Figure 29. Measured DMD of 120 μm core GI-PF-POF: a) 38 ps over 100 m b) 71 ps over 200 m c) 95 ps over 300 m

4.4.5. Statistical behavior of POF performance

We demonstrated that GI-PF-POF has been shown to be a capable optical medium for low-cost, short-reach (<100 m) high-bandwidth links. However, unlike single mode fiber, an essential challenge of deploying multimode fiber links is the wide variability in the channel response owing to the challenges associated with reproducing the optimal index profile and launch conditions. To ensure robust link performance a statistical study of the fiber behavior is required. Indeed, a statistical analysis of glass MMF was essential to the successful development of the 10 GbE standards. A similar approach has not yet been taken in the case of GI-PF-POF due to the statistically inadequate published data on the measured POF response and the uncalibrated interplay between the two dominant factors, variation in refractive index and strong mode coupling, influencing the POF response.

We report the first statistical study of commercially available 10Gb/s GI-PF-POF by performing high-resolution DMD measurements on 78 POF samples of a variety of construction, length and core size. We measured six variations of GI-PF-POF: three types of "bare" fiber comprised of core, cladding, and over-cladding only; two types of "coated" fiber, which have an additional overcoat layer ~1000μm thick; and one type of conventional Kevlar-jacketed "cabled" fiber. Of the bare fiber, we measured 62μm core fiber with overclad diameters of 490μm (62/490/none) and of 750μm (62/750/none), and 120μm core fiber with an overclad diameter of 750μm (120/750/none). Of the coated fiber, we measured 62μm and 120μm core fiber, both having a 750μm over-clad and a ~1000μm coating (62/750/1000 and 120/750/1000 respectively). The cabled fiber was 62μm core with a 490μm over-clad which was then cabled in a conventional manner (62/490/cable).

The fiber end preparations were performed using a POF milling machine and care was taken to minimize scattering losses at the transmitting and receiving ends.

The measured DMD vs. fiber length for the set of 62/490/none and all 62 μm POF are shown in Figure 30 and Figure 31 respectively. The 'run' denotes the POF produced with same manufacturing settings; the 'sample' denotes POF segments taken from the same run. It is apparent from Figure 30 that POF response varies from run-to-run more than from sample-to-sample. The variation within runs is as much as that of between different types of 62μm POF.

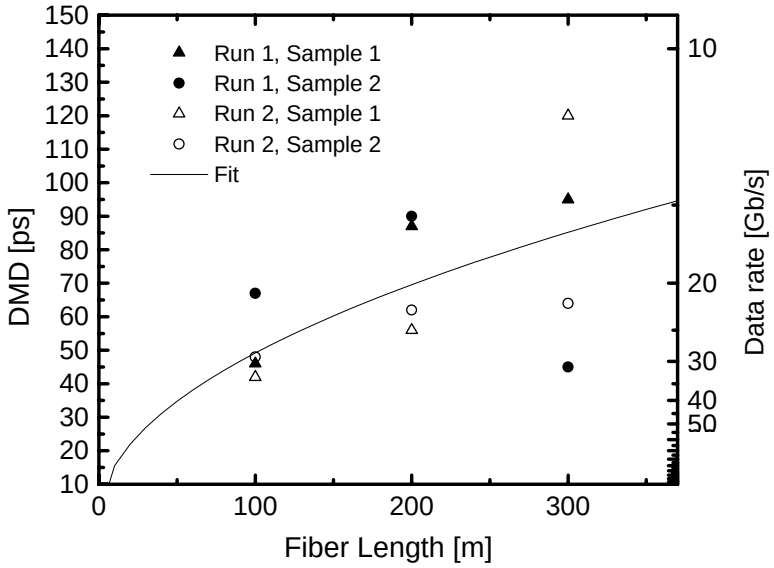

Figure 30. Scattered plot of DMD vs. fiber length for 62/490/none GI-PF-POF. The fitted line denotes the bandwidth scaling with square-root dependence on length.

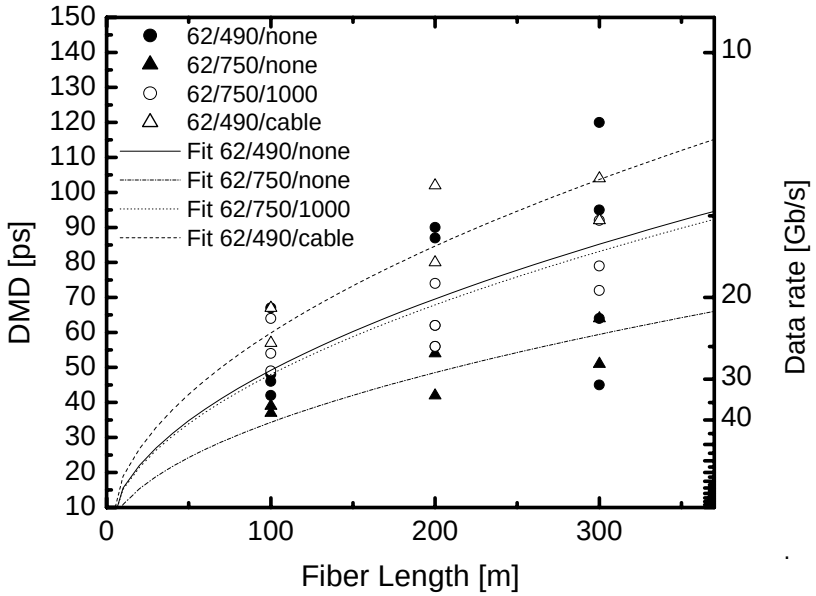

Figure 31. Scattered plot of DMD vs. fiber length for 62 μm GI-PF-POF. The fitted line denotes the bandwidth scaling with square-root dependence on length.

The estimated supported data rate is also shown in the figure. We estimate the supported data rate by assuming a nominally Gaussian shape for the pulse response. We find that the mean and standard deviation of the DMD at 200m is 65ps and 16ps respectively (the FWHM is 46 ps) and thus the 62μm POF readily supports 10Gb/s for lengths up to 200m (the longest practical length due to attenuation of ~35dB/km). Considering the minimum measurable DMD is 34ps, we estimate that as many as half of the 62μm POFs will support 40Gb/s up to 100m; remarkable considering these fibers have a specified >300MHz-km bandwidth.

For the strong mode coupling known to exist in POF, the bandwidth is expected to scale as the square root of fiber length. We therefore also show the best fit function of the form αL^{β} where L is the fiber length, α is a scaling factor and β is the power law

dependence. The best fit for all the 62μm fibers requires β=0.5, consistent with strong mode coupling.

The measured DMD vs. fiber length for the set of 120/750/none and all 120μm POF are shown in Figure 32 and Figure 33 respectively. The best fit for 120μm POF requires β's of 0.7 and 0.5 for 120/750/none and 120/750/1000 respectively. The mean and standard deviation of DMD at 100m is 64ps and 16ps respectively (the FWHM is 46 ps); thus, 120μm GI-PF-POF readily supports 10Gb/s over 100m.

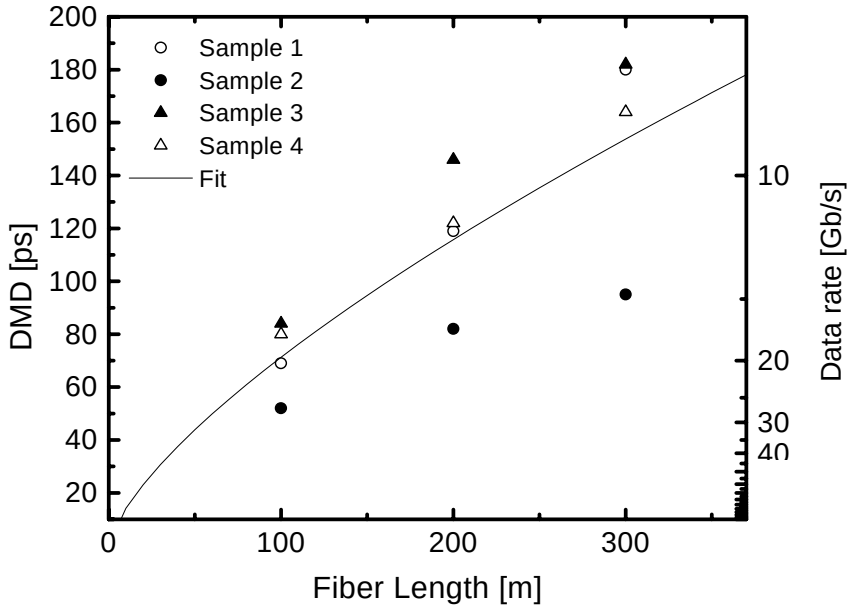

Figure 32. DMD vs. fiber length for 120/750/none GI-PF-POF. The line denotes the best fit and shows a bandwidth scaling with square-root dependence on length.

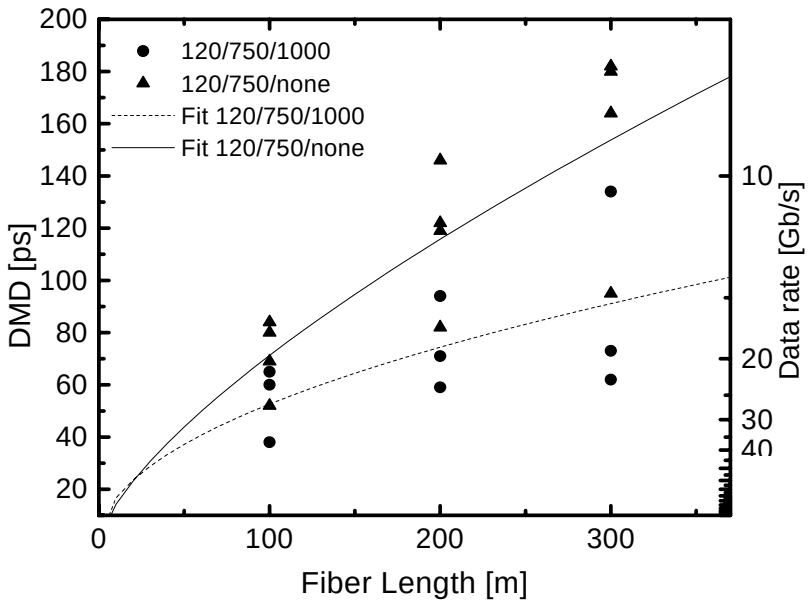

Figure 33. DMD vs. fiber length for 120 μm GI-PF-POF. The lines denote the best fit and shows a bandwidth scaling with square-root dependence on length.

4.5. Summary

It is demonstrated using experimental results and numerical model that in the strong mode coupling regime large variation in the refractive index profile of GI-POF can be tolerated while keeping the DMD small. The numerical simulation performed for 50-μm GI-POF is equally applicable to GI-POF with larger core sizes. It is found that 40 Gb/s transmission is feasible over 200 m of 50-μm GI-PF-POF.

CHAPTER V

LARGE-AREA HIGH-SPEED RECEIVERS

5.1. Introduction

The principal driving force behind MMF economy is the large alignment tolerance due to its large core size. The large core diameter and numerical aperture of the MMF ease the coupling of light into the fiber from the source – and thus greatly reduces the alignment tolerance at the transmitter. However, those same attributes increases the difficultly in capturing of the light efficiently onto a detector. If the light is not captured completely in the detector, apart from the reduction in power, there can be additional modal noise penalty. On the other hand, large detector results in large depletion layer capacitance. Therefore, the design of transimpedance amplifier that meets the electrical specifications of high bandwidth and low noise becomes difficult.

Figure 34 shows the model of a typical optical receiver consisting of photodetector (PD) and feedback transimpedance amplifier (TIA). The photodetector is modeled as a current source I_{pd} in parallel with the photodetector capacitance C_{pd}. The feedback transimpedance amplifier has a transimpedance gain of R_F. The transit time of the photodetector is often short and the nominal bandwidth of the receiver is given by

$$f_{-3dB} = \frac{A_T}{2\pi R_F C_{pd}}. \tag{19}$$

The gain A_T of the amplifier that satisfies the bandwidth requirement of the receiver is

limited by the process parameters (f_T). It is evident from Eq. (19) that larger C_{pd} requires smaller R_F to satisfy the bandwidth requirement. This, apart from reducing the transimpedance gain, also increases the input referred noise of the receiver given by

$$\left\langle i_n^2 \right\rangle = \frac{4k_B T}{R_F}, \tag{20}$$

where k_B is the Boltzman's constant and T is the operating temperature. Increase in the input referred noise reduces sensitivity of the receiver. Thus, the design of a receiver with a large photodetector requires a tight trade-off between the receiver sensitivity and bandwidth.

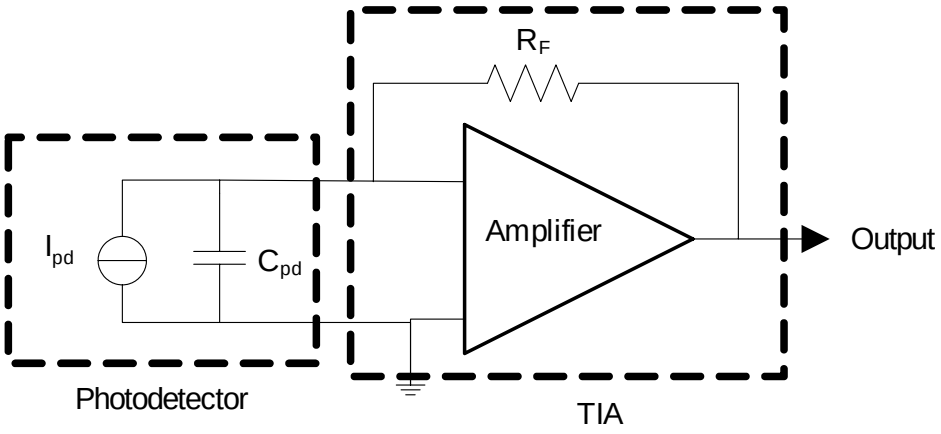

Figure 34. Front end of optical receiver

5.2. Standard receiver with large photodetector

Table 6 shows the diameter, depletion layer capacitance and typical bandwidth properties of some of the commercially available photodetectors. The bandwidth of these photodetectors is primarily input pole limited as mentioned above and not transit-time-limited. According to Eq. (19), the maximum photodetector capacitance for a TIA input

resistance of 50Ω is 318 fF. Thus, a 10-Gb/s receiver with conventional TIA has limitation in the detector diameter. A TIA with a lower input resistance (20-30 Ω) would enable the use of larger active area (100 μm diameter) photodetector with relatively larger photodetector capacitance. We have evaluated and implemented regulated input based TIA as the possible solution to develop the receiver with large photodetector.

Table 6. Commercially available typical large area photodetectors [40]-[43]

Vendor	Photodetector type	Photodetector diameter (μm)	Photodetector capacitor (fF)	Bandwidth (GHz) / Data rate (Gb/s)
Cosemi	GaAs PIN	75	-	-/10-12.5
	GaAs PIN	100	340	/4
Albis	GaAs PIN	70	240	10/10
	GaAs PIN	100	400	5/5
Vitesse	GaAs PIN	100	350	6/-
Hamamatsu	GaAs MSM	200	500	3/-

5.3. Regulated Cascode Transimpedance amplifier

In recent years, there has been a lot of interest in TIA with regulated cascode (RGC) input configuration for its tolerance to large input capacitance. Table 7 shows some of the reported performance of RGC input based TIA (RGC-TIA) [44]-[48]. Improvements over the conventional RGC-TIA have been reported [49]. Simulation results showing that RGC-TIA can tolerate up to 1 pF of input capacitance while supporting >10 Gb/s data rate has been reported [50]. However, the only implementation that can accept a large capacitance of 0.5 pF is designed for relatively lower speed (1.25 Gb/s) application.

The other implementations supporting 10 Gb/s data rate has been shown to tolerate only up to 0.32 pF capacitance. Thus, the potential of RGC-TIA has not been fully exploited for high-speed, alignment-tolerant receiver applications. Also, to the best of our knowledge, analysis and implementation of the RGC-TIA in bipolar technology has not been reported in the literature.

Table 7. Reported performance of RGC-TIA

Process	Input cap. (pF)	Speed / Bandwidth (Gb/s / GHz)	Input referred noise (pA/√Hz)	Sensitivity	Gain (dBΩ)	Power/ Supply (mW/V)
0.6 μm digital CMOS [44]	0.5	1.25/0.95	6.3	-20dBm @10^{-12}	58	85/5
0.6 μm digital CMOS [45]	.5	2.5/2.2		-17dBm @10^{-10}	55.3	210/5
0.18 μm CMOS [46]	0.15	10/7.6		-12dBm @10^{-12}	87	210/1.8
80 nm digital CMOS [47]	0.32	-/13.4	28	-8 dBm	52	2.2/1
0.18 μm RF CMOS [48]	0.25	-/8	18		53	13.5/1.8

5.4. Analysis of regulated cascode input stage

5.4.1. Basic principle of operation

Figure 35 shows the basic RGC input stage. The transistor T_2 is a common-emitter amplifier stage with open loop gain $G_{T_2} = -g_{m2}R_{c2}$. The transistor T_1 is a common-base stage with T_2 acting as a local feedback to the base of the T_1. Due to the feedback, the input impedance of the RGC input stage is reduced to $z_{in,RGC} \approx \frac{V}{I} = \frac{1}{g_{m1}\left(1 + g_{m2}R_{c2}\right)}$.

Thus the input impedance of RGC-TIA is $\left(1+g_{m2}R_{c2}\right)$ times lower than that of the common-base stage T_2 alone. This low input impedance moves the input pole resulting from the photodetector capacitance (Eq. 19) to higher frequency and reduces its bandwidth limiting effect. The input photodetector current follows the low impedance path into the emitter of T_1 and is amplified with unity current gain. Thus, the output voltage at the collector is R_{c1} times the photodetector current, i.e. the transimpedance gain is ~R_{c1}.

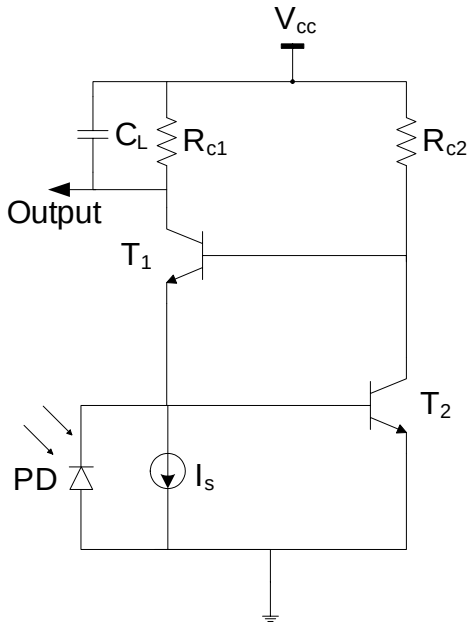

Figure 35. Schematic diagram of RGC input stage

5.4.2. AC analysis and bandwidth optimization

Figure 36 shows the approximate small signal model of the RGC input stage with a photodetector. The resistors and capacitors in parallel are represented by the corresponding equivalent value. They are: total input capacitance $C_i = C_{pd} + C_{\pi 2}$; total

base-collector capacitance for T_2 $C_f = C_{\pi 1} + C_{\mu 2}$; effective base-emitter resistance for T_2 $R_i = R_{\pi 2}$.

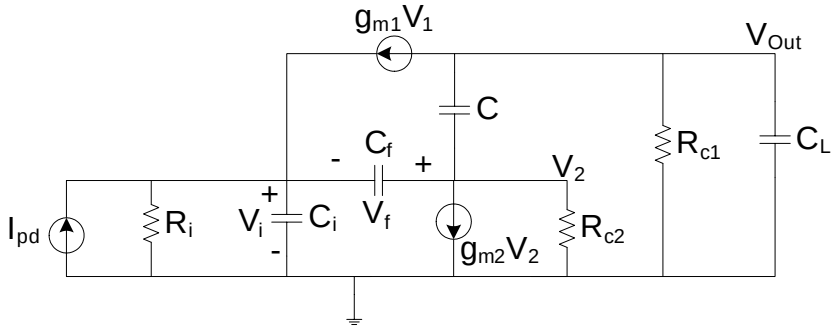

Figure 36. AC equivalent circuit of RGC input stage

The small signal model of the RGC input stage is analyzed and the input impedance is given by

$$Z_{in}(s) = \frac{v_i}{i_{pd}} \approx \frac{1}{g_{m1}(1+g_{m2}R_{c2})} \frac{(1+sR_{c2}C_f)}{\left(1+\frac{C_f+C_{ie}}{g_{m1}}s+\frac{R_{c2}}{g_{m1}}C_fC_{ie}s^2\right)}, \tag{21}$$

where the effective input capacitance $C_{ie} = \frac{C_i}{(1+g_{m2}R_{c2})}$. The result is consistent with the low frequency ac analysis i.e. $Z_{in,RGC} = Z_{in}(0)$.

The transimpedance gain Z_T of the RGC input stage is given by

$$Z_T(s) = \frac{v_{Out}}{i_{pd}} \approx R_{c1} \frac{1}{\left(1+\frac{C_f+C_{ie}}{g_{m1}}s+\frac{R_{c2}}{g_{m1}}C_fC_{ie}s^2\right)(1+sR_{c1}C_L)} \tag{22}$$

The transimpedance gain at $s = 0$ is R_{c1} as found in the low frequency ac analysis. The denominator has a second order form which dominates the response. Therefore, the optimum response is obtained by optimizing the second order function for a critically

damped transfer function with maximum frequency. The denominator of the second order form is given by $D(s) = \frac{s^2}{\omega_n^2} + 2\gamma\frac{s}{\omega_n} + 1$. By comparison with Eq. (22),

$$\omega_n = \sqrt{\frac{g_{m1}}{R_{c2}C_fC_{ie}}} \tag{23}$$

and

$$\gamma = \frac{1}{2}\frac{C_{ie}+C_f}{\sqrt{C_{ie}C_f}}\frac{1}{\sqrt{g_{m1}R_{c2}}}. \tag{24}$$

The design goal is to a) Maximize ω_n and b) optimize such that $\gamma = 1/\sqrt{2}$.

Maximizing ω_n is equivalent to minimizing $1/\omega_n^2$. Using Eq. (23) and expanding the terms,

$$1/\omega_n^2 = \frac{C_{pd}}{g_{m2}f_{T1}} + \frac{C_{pd}}{g_{m1}f_{T2b}} + \frac{1}{f_{T1}f_{T2a}} + \frac{g_{m2}/g_{m1}}{f_{T2a}f_{T2b}}, \tag{25}$$

where, $2\pi f_{T1} = \frac{g_{m1}}{C_{\pi1}+C_{\mu1}} \approx \frac{g_{m1}}{C_{\pi1}}$, $2\pi f_{T2} = \frac{g_{m2}}{C_{\pi2}+C_{\mu2}}$, $2\pi f_{T2a} = \frac{g_{m2}}{C_{\pi2}}$, and $2\pi f_{T2b} = \frac{g_{m2}}{C_{\mu2}}$.

To obtain the best performance, the transistors T_1 and T_2 are biased at the maximum f_T. Therefore, f_{T1}, f_{T2}, f_{T2a}, and f_{T2b} can be assumed to be constants. To minimize the RHS of Eq. (25), it is first minimized with respect to g_{m2}. The condition obtained is

$$\frac{C_{pd}}{g_{m2}f_{T1}} = \frac{g_{m2}/g_{m1}}{f_{T2a}f_{T2b}} \Rightarrow C_{pd}C_{\pi1} = C_{\pi2}C_{\mu2}. \tag{26}$$

The RHS of Eq. (25) is minimized for smaller g_{m1}, but value of g_{m1} is constrained by other factors such as the bias requirements, peaking and noise. The T_1 requires a minimum dc bias current such that it remains in the active region for large photocurrent. This ensures a minimum value for g_{m1}. From Eq. (24), the damping factor is approximately given by,

$$\gamma \approx \frac{1}{2}\sqrt{\frac{C_{ie}/C_f}{g_{m1}R_{c2}}} \approx \frac{1}{2}\sqrt{\frac{C_i/C_f}{g_{m1}g_{m2}}}\frac{1}{R_{c2}} \tag{27}$$

The value of R_{c2} is determined using Eq. (27) for appropriate peaking. The value of R_{c1} is optimized for larger transimpedance gain until the effect of the output pole (Eq. 22) becomes significant. It is noted that the peaking is a more sensitive function of R_{c2} than the transistor parameters. Increasing R_{c2} decreases γ i.e. increases peaking. Peaking is also increased when a photodiode with smaller C_{pd} than the designed value is used.

5.4.3. Noise analysis

Figure 37 shows the ac equivalent of the RGC input stage including the significant noise sources.

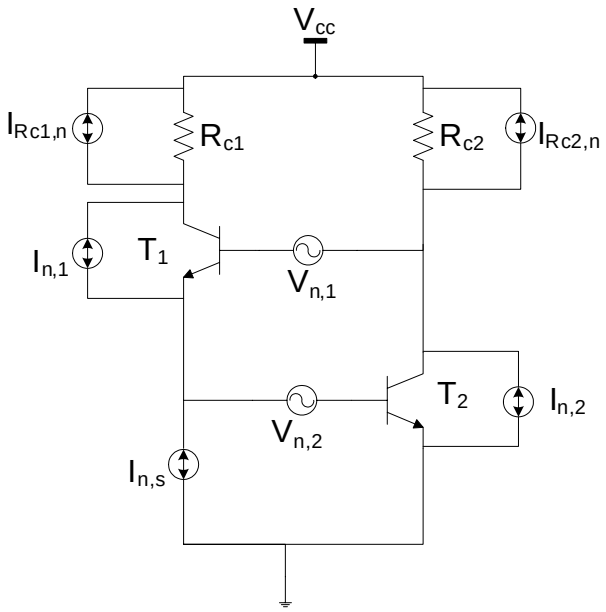

Figure 37. AC equivalent of RGC input stage including noise sources

To obtain the equivalent input noise, the noise power spectral density is determined analytically for each noise source separately. The noise contributions from the transistors T_1 and T_2 are shot noise ($I_{n,1}$ and $I_{n,2}$) resulting from the collector current, thermal noise ($V_{n,1}$, $V_{n,2}$) resulting from the base resistor (R_{b1} and R_{b2}). The base shot noise contribution is ignored. The thermal noise contribution from the resistors ($I_{n,Rc1}$ and $I_{n,Rc2}$) and the noise from the biasing current source ($I_{n,s}$) are included. Relevance of each is determined by evaluation using typical parameter values. After complete analysis and appropriate approximations, the input referred noise current is obtained as:

$$I_{n,eq} = s\left(C_{ie} + C_{\mu 2}\right)V_{n,1} + s\left(\frac{C_{ie} + C_f}{g_{m1}}\right)I_{n,1} + s\left(C_{pd} - C_{\mu 2}\right)V_{n,2} + s\left(\frac{C_i}{g_{m2}}\right)I_{n,2} + I_{n,s} + DI_{n,Rc1} + s\left(\frac{C_i}{g_{m2}}\right)I_{n,Rc2}, \quad (28)$$

where $D = \left(1 + \frac{C_{ie} + C_f}{g_{m1}}s + \frac{R_{c2}}{g_{m1}}C_f C_{ie}s^2\right)$.

The noise sources associated with the T2 and Rc2 provide the excess noise compared to the noise contributors of the common-base TIA. This excess noise degrades the sensitivity of the RGC-TIA.

The power spectral density of the equivalent input noise current is found to be:

$$\overline{I}_{n,eq}^2 = \omega^2\left(C_{ie}+C_{\mu 2}\right)^2\overline{V}_{n,1}^2 + \omega^2\left(\frac{C_{ie}+C_f}{g_{m1}}\right)^2\overline{I}_{n,1}^2 + \omega^2\left(C_{pd}-C_{\mu 2}\right)^2\overline{V}_{n,2}^2 + \omega^2\left(\frac{C_i}{g_{m2}}\right)^2\overline{I}_{n,2}^2$$
$$+\left(1+\omega^2\left(\frac{C_{ie}+C_f}{g_{m1}}\right)^2\right)\overline{I}_{n,Rc1}^2 + \omega^2\left(\frac{C_i}{g_{m2}}\right)^2\overline{I}_{n,Rc2}^2 + \overline{I}_{n,s}^2$$
$$= \omega^2\left(\frac{C_{pd}+C_{\pi 2}+g_{m2}R_{c2}C_{\mu 2}}{g_{m2}R_{c2}}\right)^2 4kTR_{b1} + \omega^2\left(\frac{C_{pd}+C_{\pi 2}+g_{m2}R_{c2}\left(C_{\pi 1}+C_{\mu 2}\right)}{g_{m2}R_{c2}}\right)^2\frac{2kT}{g_{m1}} \quad (29)$$
$$+\omega^2\left(C_{pd}-C_{\mu 2}\right)^2 4kTR_{b2} + \omega^2\left(C_{pd}+C_{\pi 2}\right)^2\frac{2kT}{g_{m2}}$$
$$+\left(1+\omega^2\left(\frac{C_{pd}+C_{\pi 2}+g_{m2}R_{c2}\left(C_{\pi 1}+C_{\mu 2}\right)}{g_{m1}g_{m2}R_{c2}}\right)^2\right)\frac{4kT}{R_{c1}} + \omega^2\left(\frac{C_{pd}+C_{\pi 2}}{g_{m2}}\right)^2\frac{4kT}{R_{c2}} + +\overline{I}_{n,s}^2$$

The, noise contribution from $I_{n,Rc1}$ is constant at the output and thus input referred noise increases at high frequency. It is obvious from Eq. (29) that, at higher frequency significant noise contribution occurs due to $V_{n,2}$ and $I_{n,2}$. The contribution from $V_{n,2}$ can be reduced by reducing the base resistance R_{b2}. In the case of $V_{n,2}$ and $I_{n,2}$, the noise contribution at higher frequency is proportional to photodetector capacitance C_{pd}. However, for a particular C_{pd}, the contribution from $I_{n,2}$ is minimized for $C_{pd} = C_{\pi 2}$.

Thus, considering Eq. (26), the design rule optimizing both noise and the bandwidth is found be $C_{pd} = C_{\pi 2}$ and $C_{\pi 1} = C_{\mu 2}$. (30)

The sizes of transistors T1 and T2 can be appropriately chosen to satisfy Eq. (30). It should be noted that the transistor sizes found by using Eq. (30) is consistent with the requirement of small g_{m1} stated earlier. Thus, both low noise and high bandwidth requirements can be simultaneously satisfied.

5.5. Large-area 10 Gb/s photoreceiver

A 10 Gb/s optical receiver for large-core MMF is designed which uses a relatively larger photodetector and a RGC-TIA. The receiver uses a GaAs PIN photodetector with an active area diameter of 100 μm or higher. A receiver with such a detector and conventional TIA would yield a typical bandwidth of <5 GHz. Thus, the proposed receiver would provide larger tolerance for conventional MMF core size (50 and 62.5 μm) and would allow even larger core (~100 μm) glass MMF or POF. Therefore, low-cost, highly alignment tolerant 10 Gb/s link using large-core POF and the designed receiver would be possible. Although CMOS is the preferred technology for its low high-volume cost, the RGC-TIA is implemented in BiCMOS process for its higher available gain and bandwidth. It is a standard 5 metal layer, 0.35 μm BiCMOS process with an f_T of 45 GHz.

5.5.1. Photoreceiver on board

Figure 38 shows the basic block diagram of the proposed photoreceiver consisting of a biased photodetector and the receiver die. The RGC receiver block consists of three basic blocks – RGC TIA, a single-ended to differential (S-to-D) conversion block, and a current mode logic (CML) buffer. The final outputs are differential outputs.

The RGC TIA is designed to tolerate a photodetector capacitance up to 0.7 pF. The designed bandwidth of RGC TIA is 9 GHz. The transimpedance gain is 60 dBΩ. The S-to-D conversion block is designed using the differential amplifier with the output of RGC TIA as one input and the D.C. reference signal as the other input. The D.C. reference

signal is generated by low-pass filtering the output of the RGC-TIA. The gain of this block is 10 dB. The CML buffer is designed to yield 150 mV peak to peak voltage swing for each output.

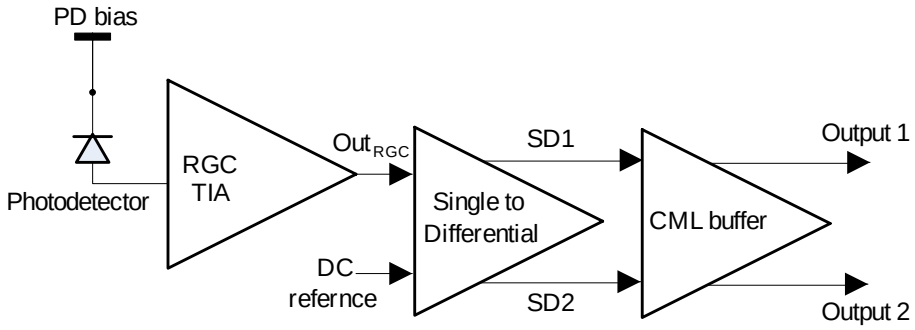

Figure 38. Block diagram of the photoreciver consisting of the photodiode and the RGC receiver block. The RGC receiver consists of RGC TIA, single-ended to differential conversion block and current mode logic buffer.

The complete photoreceiver is developed on board. The receiver die along with the GaAs PIN photodetector with 100 μm diameter from COSEMI is placed on the board. The anode of the photodetector is wirebonded to the input of the RGC TIA. The outputs of the receiver die are wirebonded to the 50 Ω transmission lines on the board. The photodiode is reverse biased with the cathode connected to a .1 μF capacitor to reduce the noise in the bias voltage.

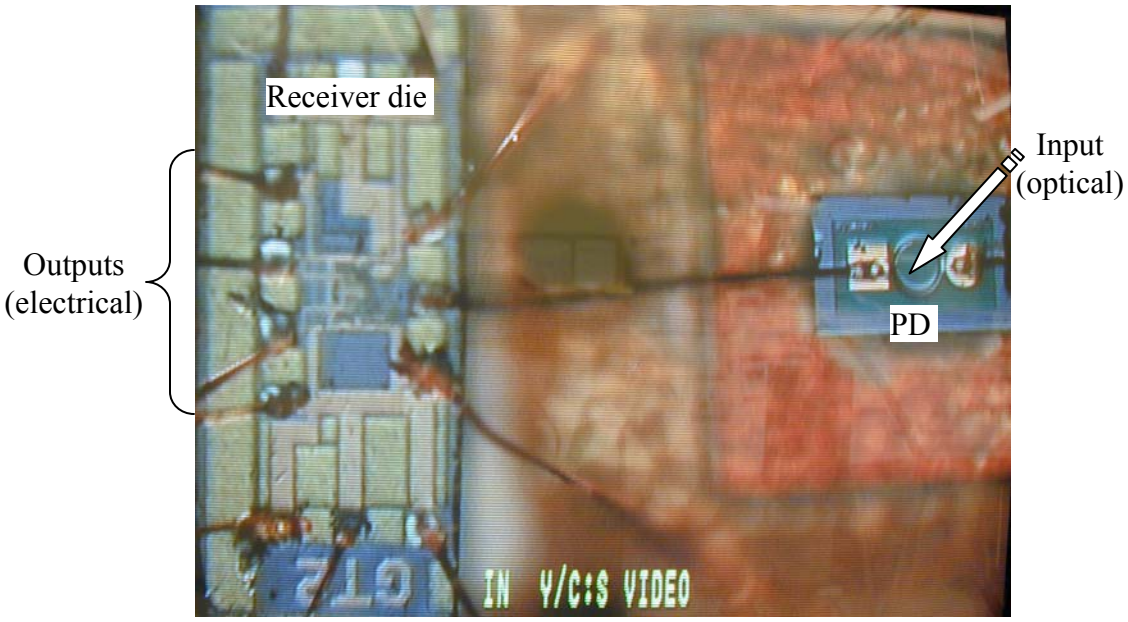

Figure 39. Receiver on board: receiver die (left) and GaAs photodiode (right) are placed on a board. The anode of the photodiode is wirebonded to the receiver input and the outputs are wirebonded to 50 Ω transmission lines on board.

5.5.2. Evaluation of the receiver

Due to the lack of availability of broadband and high-speed balun in our laboratory at the time of measurement, one output is evaluated at a time.

Figure 40 shows the measured eye diagram with the 10 Gb/s PRBS 2^{31}-1 bit pattern with incident optical power of -10 dBm. Clearly, the eye is open with low temporal and amplitude jitter. The rise time is ~60 ps.

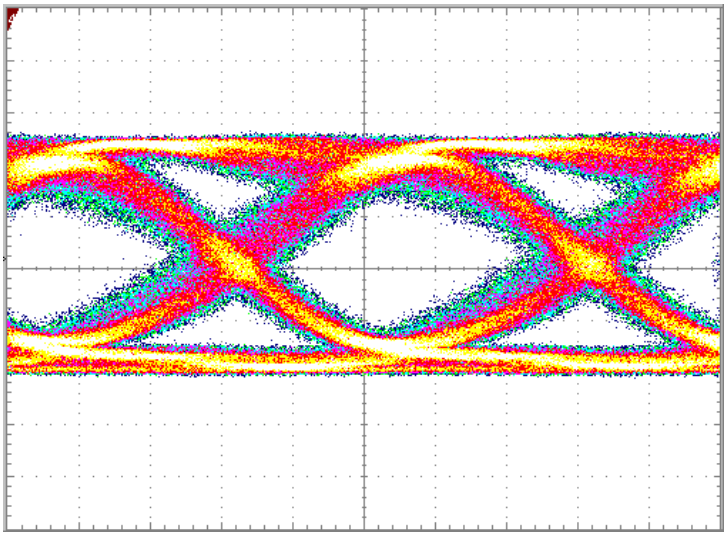

Figure 40. Measured eye diagram at 10 Gb/s with PRBS 2^{31}-1 signal at -10 dBm of optical power.

Figure 41 shows BER measurement results at 10 Gb/s with PRBS 2^{31}-1 signal for single output with the other output terminated with 50 Ω load. The sensitivity for the single output is -11 dBm at 10 Gb/s at a BER of 10^{-12}.

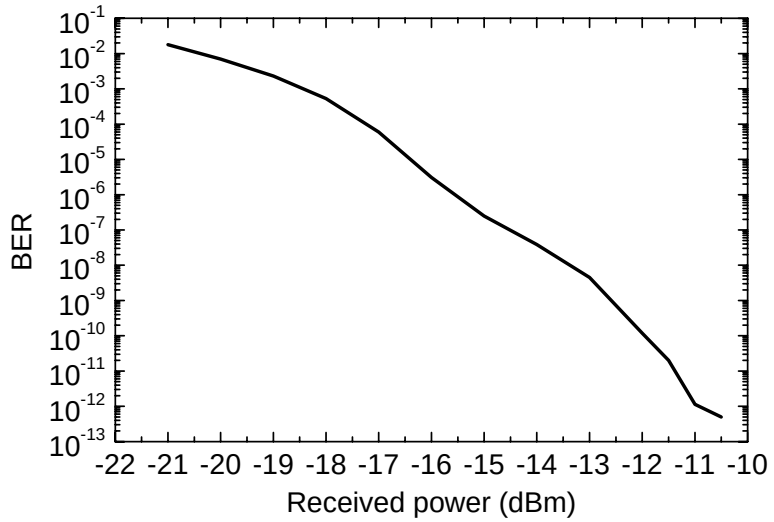

Figure 41. Measured BER at 10 Gb/s with PRBS 2^{31}-1 signal for one output with the other output terminated with 50 Ω load

We note that, the differential evaluation of the receiver improves the sensitivity by 3 dB. Therefore, for a typical 10 Gb/s link at 850 nm the photoreceiver yields a sensitivity of -14 dBm at BER of 10^{-12}. This performance is comparable to the state-of-the-art receiver for MMF [50] using a photodiode much larger compared to the typical photodiode used for MMF link.

5.6. Summary

We report the development of 10 Gb/s regulated cascade input stage based TIA which can tolerate a large photodetector capacitance of 0.5-0.7 pF. The TIA enables the use of large sized photodetectors with large diode capacitance while supporting large bandwidth. The TIA is integrated with a GaAs PIN photodetector with an active area

diameter of 100 μm. The receiver is designed in 0.35 μm BiCMOS process and has a sensitivity of -14 dBm at BER of 10^{-12} at 850 nm wavelength.

The developed optical receiver is significantly larger than the conventional 10 Gb/s receiver with modest degradation in the sensitivity. Thus, MMF and receiver alignment tolerance is greatly improved reducing the packaging cost at the receiver-end. This also enables the use of larger core POFs (100 – 120 μm diameter) by improving the collection efficiency.

CHAPTER VI

HIGH-SPEED PLASTIC OPTICAL FIBER LINKS

6.1. Introduction

It is shown in chapter 4 that GI-PF-POF has large bandwidth that can support high data rate of transmission. It is also shown that the available bandwidth is highly insensitive to the launch conditions i.e. the coupling of light from the transmitter to the POF core. In this chapter high data rate links using GI-PF-POFs are demonstrated. The link lengths are typically limited by the available power budget. Thus, the one of the primary objective of the research i.e. realization of high-performance, short-reach links is achieved.

Using larger-core GI-PF-POF and the large-area receiver described in chapter 5, a short reach 10 Gb/s link is realized that provides large alignment tolerance at the transmitter because of the core-size of the POF and large alignment tolerance at the receiver because of the larger area of the detector. This link is the key to the design of low-cost, short-reach, high-data-rate links that is the primary goal of the research.

6.2. 40 Gb/s POF links

In chapter 4 it is found via impulse response and DMD measurements that 50μm core GI-PF-POF supports 40 Gb/s transmission over 100 m of link length. However, until

now to the best of our knowledge, 40 Gb/s transmitters are available only at longer wavelengths such as 1300 nm and 1550 nm. Therefore, 40 Gb/s links using POF were demonstrated at those wavelengths.

6.2.1. 40 Gb/s POF links at 1550 nm

40 Gb/s links are popular and primarily available at 1550 nm SMF links. However, attenuation in GI-PF-POF at 1550 nm is high (150 dB/km) and therefore, the link length is limited to short distances (<30 m). Figure 42 shows the experimental set up for the evaluation of 40 Gb/s, 30 m GI-PF-POF link at 1550 nm. The transmit optical data is generated using a 40Gb/s $LiNbO_3$ intensity modulator and a CW laser source capable of 9 dBm output power to compensate the higher attenuation in the POF link at 1550 nm. The MMF receiver has a bandwidth of 22 GHz and is followed by a 38 GHz linear amplifier with 26 dB gain. We are thus able to evaluate BER of the link up to 30 Gb/s without significant receiver induced ISI penalty.

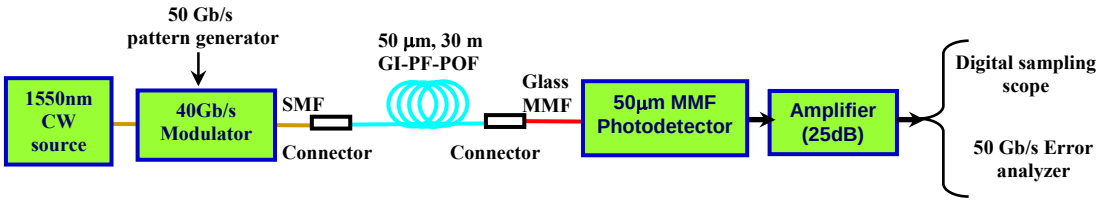

Figure 42. Experimental set up for 40 Gb/s POF link evaluation

We examine the impulse response of 30 m lengths of GI-PF POF at 1550 nm with high dynamic range and temporal resolution. At 1550 nm, a passively mode locked fiber laser followed by optical bandpass filter is used to obtain 16 ps pulses. The POF output was coupled to a 50 µm glass MMF pigtail of a broadband commercial photodetector and

a digital sampling oscilloscope with combined bandwidth >30GHz and with less than 1ps jitter. Figure 43 shows the impulse response measurements of the back-to-back and the link at 1550nm. The 30m response is almost indistinguishable from the reference. This and the lack of distinct mode groups typically observed in silica MMF is indicative of the strong mode coupling regime.

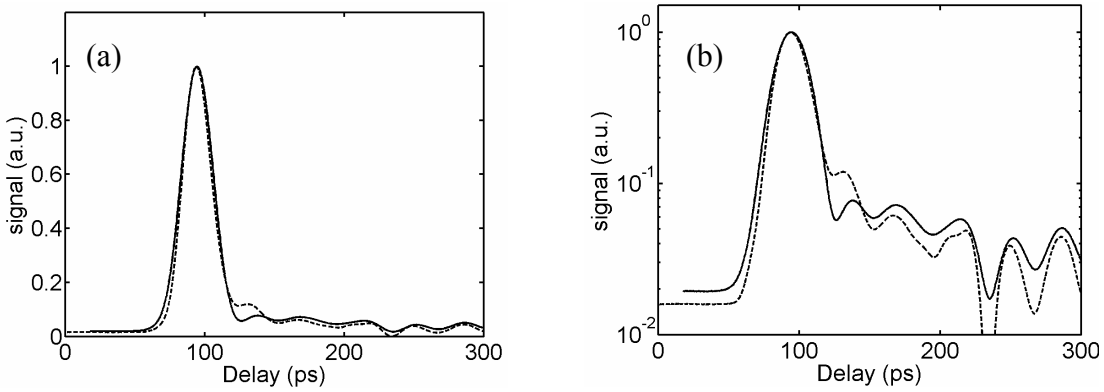

Figure 43. (a) Impulse responses at 1550 nm after transmission through 30 m of GI-PF-POF, (b) Log plot of the same. Dotted curve represents the reference pulse.

Figure 44 shows the measured eyes at 10, 20, 30, and 40 Gb/s. Eye diagram measurements at different offsets also confirm the launch insensitivity as demonstrated by the DMD measurement. The eyes for 10 Gb/s and 20Gb/s show large eye openings and Q factor necessary to maintain a very low BER. The eye for 30 Gb/s depicts a slight ISI penalty due to the limited receiver bandwidth. At 40 Gb/s, the eye opening is noticeably reduced due to ISI.

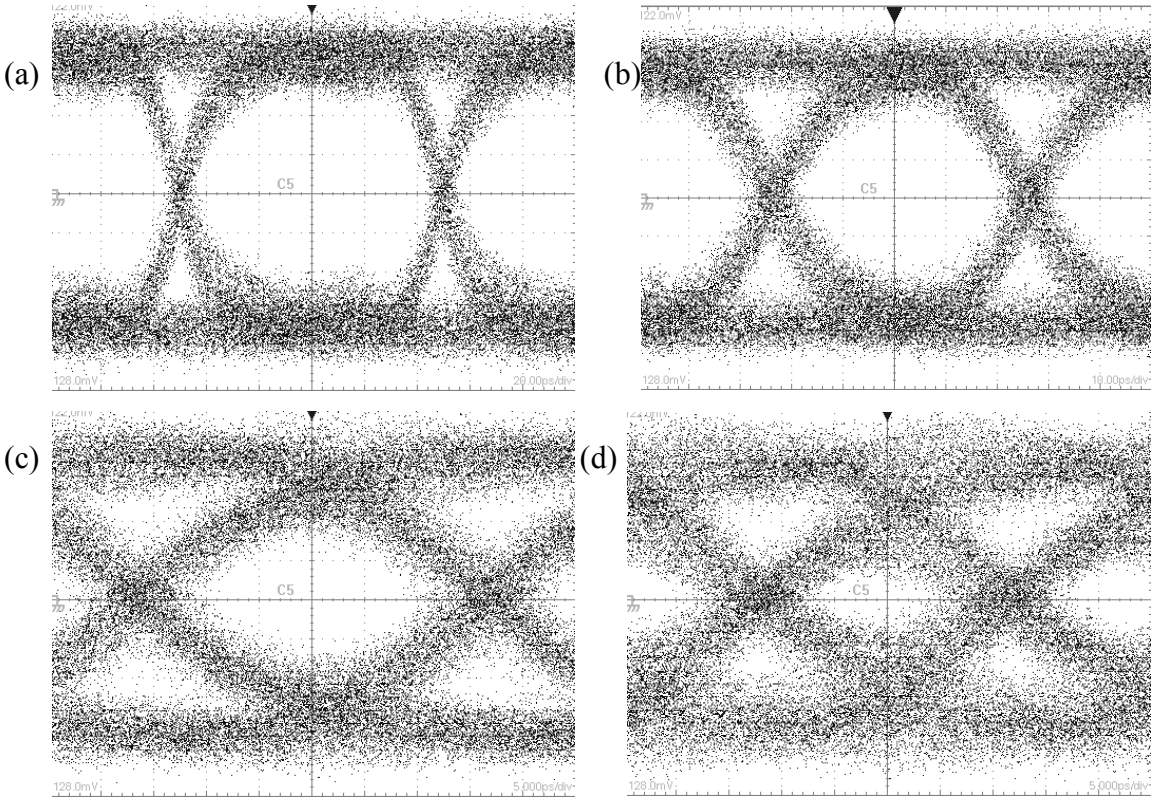

Figure 44. Eye diagrams for a PRBS 2^{31}-1 after 30m GI-PF-POF at a) 10Gb/s b) 20Gb/s c) 30Gb/s d) 40Gb/s. The ISI results from bandwidth limitations of the receiver.

Figure 45 shows the BER curves for 10, 20, and 30 Gb/s for both back-to-back and the POF link. The figure indicates 3.1dB penalty for the 10 Gb/s and 20 Gb/s data rates and a 4 dB penalty for 30 Gb/s. These penalties include the power coupling efficiency between the POF and the receiver detector which we measured to be 2.5 dB. This mode selective loss at the receiver also contributes modal noise. Importantly, the strong mode coupling insures that the ISI will not increase with increasing receiver efficiency. Hence the net penalties are 0.6 dB for 10 Gb/s and 20 Gb/s and 1.5 dB for 30 Gb/s. The associated reduction in modal noise may further improve these results. We note that high receiver ISI penalty preclude measuring the BER at 40 Gb/s.

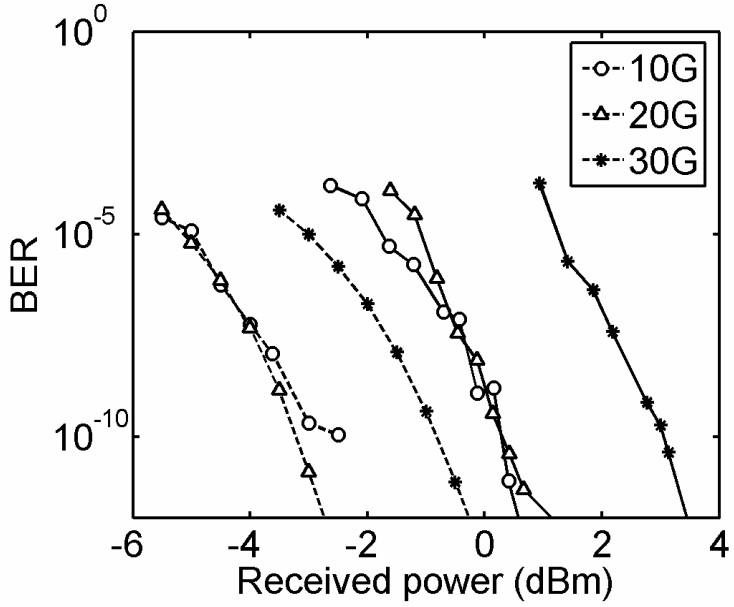

Figure 45. BER measurements for back-to-back and 30 m GI-PF-POF link with PRBS 2^{31}-1 at different bit rates.

In summary, we for the first time demonstrated a 30m POF link at 1550nm with negligible dispersion penalty up to 30 Gb/s.

6.2.2. 40 Gb/s POF links at 1310 nm

As mentioned earlier, loss in GI-PF-POF at 1550 nm is high and the preferable transmission wavelength range is 800-1350 nm. Therefore the obvious choice for the demonstration of 40 Gb/s data transmission in GI-PF-POF is 1300 nm.

The experimental setup is conventional and similar to shown in Figure 42. It includes: a 50 Gb/s pattern generator, a laser transmitter, the fiber under test, a MMF receiver followed by the error analyzer or digital sampling scope. The transmitter is comprised of a low insertion loss, X-cut Lithium Niobate intensity modulator with a bandwidth >30 GHz and a 1325 nm FP laser with 3 nm spectral width. A commercial

MMF detector is used with 3dB-bandwidth of >25 GHz and conversion gain of 13.6 V/W. This detector is followed by a linear post amplifier with 15 dB gain and bandwidth of 30 kHz-38 GHz. The fiber is 100 m of 50 μm core SC-connectorized and cabled GI-PF-POF. The signal is launched using a single mode fiber and is coupled to the detector via a 50 μm core GI-MMF and GRIN lens.

As shown in Figure 46 a the POF impulse response, corresponding to an isolated "1 bit" at 50 Gb/s, is nearly indiscernible from the reference. The FWHM of the 100 m fiber response is 29.7 ps compared to the back-to-back of 28.3 ps. Therefore, the fiber response is <10 ps and the ISI penalty due to the fiber is expected to be negligible for data rates of 40 Gb/s. Clearly higher data rates and/or longer reach are possible. The Log scale depiction of the impulse response (Figure 46 b) reveals only features due to electrical issues further indicating the integrity of the impulse response. Impulse responses at other wavelengths yield similar results.

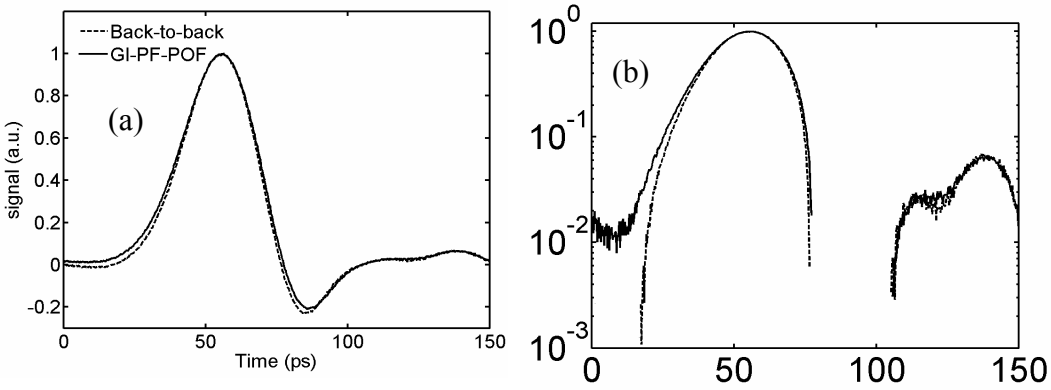

Figure 46. (a) Impulse response of 100 m, 50 μm core, graded index plastic optical fiber. (b) Log plot of the same.

Figure 47shows the 40 Gb/s eye diagram of the back-to-back and after 100 m of GI-PF-POF. The eye remains open at 40 Gb/s. The noise in the eye diagrams is limited by the detector and sampling scope noise. The reduced eye opening with increased rate is due to ISI which results almost exclusively from Tx and Rx bandwidth limitations.

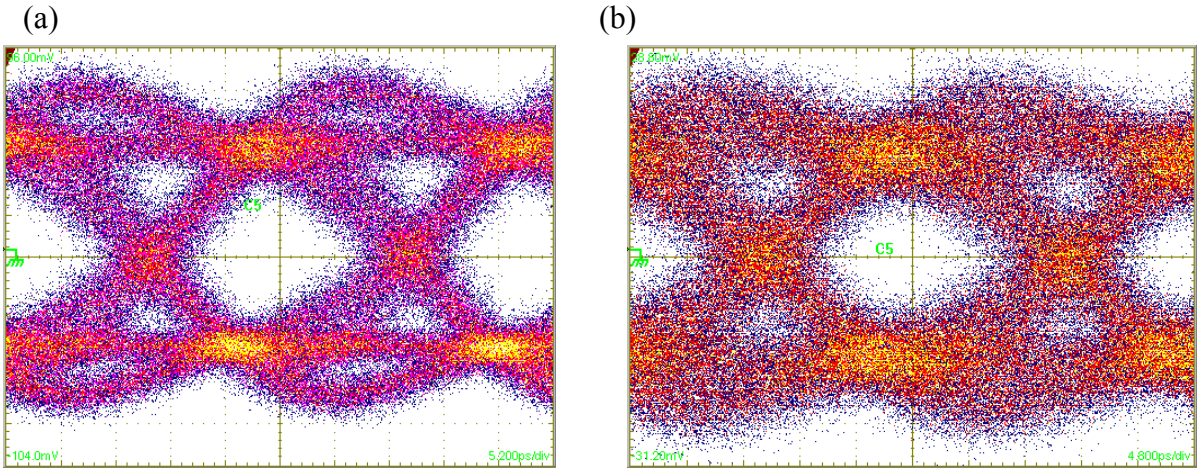

Figure 47. 40 Gb/s eye diagrams for PRBS 2^{31}-1 pattern for the (a) back-to-back and (b) after 100 m of 50 μm GI-PF-POF

Figure 48 shows the results of the BER measurements at 20, 30 and 40 Gb/s. The optical power penalty shown the BER curves for all data rates is ~1 dB which results from the coupling loss into the detector. We recorded a BER of 10^{-10} at 40 Gb/s. However, the minimum BER observed at 40 Gb/s was less than 10^{-12}. The minimum BER in 40 Gb/s is limited by the bias drift of the intensity modulator (which can be mitigated with a feedback control circuit) in an already Tx and Rx bandwidth limited system.

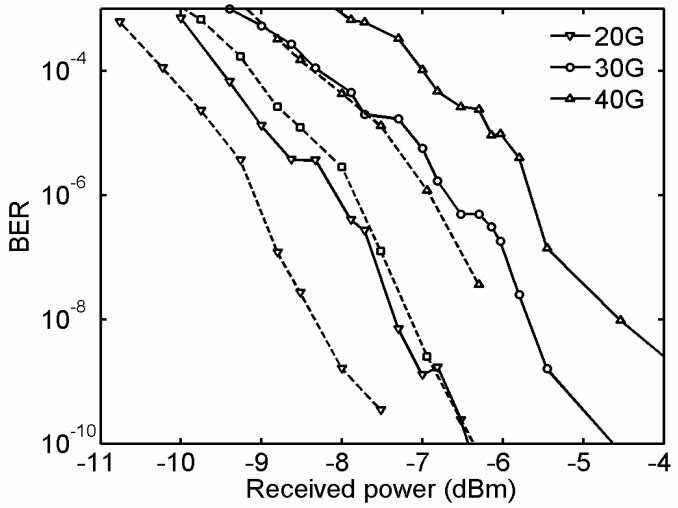

Figure 48. BER measurements for back-to-back (dashed) and 100 m GI-PF-POF link (solid) (PRBS 2^{31}-1).

6.2.3. Open challenges in 40 Gb/s POF links

Apart from satisfying the bandwidth and signal integrity requirements, a link must have an optical power budget achievable with the state-of-the-art components. Optical power budget for high-data-rate links is essentially more stringent because of the lower sensitivity of the receiver with large bandwidth. Achieving good sensitivity for large-core fiber receivers is even more challenging for two reasons. The power collection efficiency of the finite-sized detector is reduced when light is coupled from a large-core fiber with high numerical aperture and results in a direct power penalty. The large capacitance associated with a large photodetector reduces the bandwidth and increases the noise power spectral density of practical implementation of receiver stage (generally a transimpedance amplifier) following the photodetector. In the 40 Gb/s link demonstration, the receiver used has an effective sensitivity of -6 dBm at 40 Gb/s and

BER of 10^{-8}. The CW source generates a maximum of 8 dBm of power and after the modulator, maximum 0.1 dBm power is launched into the POF. The net channel insertion loss of GI-PF-POF and the GI-MMF is 4.4 dB and results in maximum received power of -4.34 dBm. Thus, the link operates within a tight power budget. Increasing the receiver sensitivity and reducing the connector losses are the keys to improve the power budget. On the other hand, the power budget for 25 Gb/s POF link would be much relaxed as the achievable receiver sensitivity would be better.

6.3. Alignment-tolerant 10 Gb/s POF links

Although, 40 Gb/s links using 50 μm core fiber and long-haul-style DFB lasers and Lithium-Niobate-modulators, larger core GI-PF-POF provide sufficient bandwidth for 10 Gb/s links at a larger alignment tolerance. Using larger 130 μm core GI-PF-POF 11 Gb/s has been demonstrated using single mode fiber launch of 1300 nm FP lasers [33],[52][33] . However, to fully exploit the alignment simplicity of larger core fiber it is necessary to develop links using low-cost 850 nm VCSELS.

Directly-modulated, multimode VCSELs are regarded as the appropriate transmitter for low-cost, high-performance MMF links. However, the interaction between the VCSEL and MMF modes requires a certain encircled flux to be maintained at the launch to ensure linearity and high-speed transmission. DMD measurement of GI-PF-POF indicates that unlike glass MMF, POF is insensitive to launch condition at the transmitter. Thus, large alignment tolerance at the transmitter can be allowed without any significant

penalty. Low-cost VCSELs with large active area and higher output power can be effectively used with POF to develop high data rate links and improved power budget.

Here we demonstrate that larger core plastic fibers (120 μm) are readily compatible with multi-transverse-mode 10 Gb/s VCSELs and that highly alignment tolerant (±15 μm) 10 Gp/s links are possible.

6.3.1. POF link: using commercial transceivers

We first demonstrated a 10 Gb/s POF link using a commercially available MMF-pigtailed VCSEL source at 850 nm (from California Scientific Inc.), 100 m of 120 μm GI-PF-POF and commercially available receiver for 62 μm glass MMF (PT-12B from Picometrix). Although, the receiver collection efficiency for a 120 μm core POF was suboptimal, the demonstration provided a proof of concept. Figure 49 shows the basic set up for the link test.

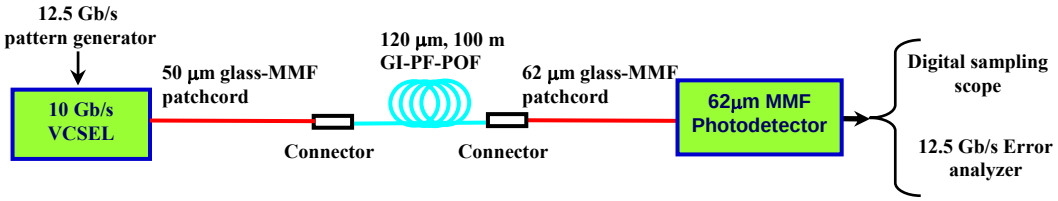

Figure 49. Experimental set up for 10 Gb/s POF link evaluation using commercial transceiver for glass-MMF

We at first examined the temporal response and link performance of three samples of 100 m of 120 μm GI-PF-POF. DMD measurements with high temporal resolution were performed to evaluate the fiber bandwidth and its sensitivity to launch conditions. The

net DMD were found to be 66, 88 and 86 ps. Figure 50 a shows the DMD of one of the POF with Y-offset of 0 μm and X-offset varying from -60 to 60 μm. Similar features are observed in the other two samples. The DMD suggests that the fiber response is nearly insensitive to offsets of ±10 μm.

The VCSEL source had a nominally 10 GHz bandwidth and 6 dB extinction ratio. The average optical power output is -3.5 dBm. Thus, the effective optical power ((Power at bit 1-Power at bit 0)/2) is -5.7 dBm. The receiver had a nominal bandwidth of 12 GHz and a sensitivity of -14 dBm at a BER 10^{-12}. Figure 50 b shows the response of the VCSEL for an isolated '1' at 12.5 Gb/s. The FWHM of the VCSEL response is 80 ps. The FWHM of the POF responses are 120, 124 and 112 ps respectively. Thus, 10 Gb/s performance can be achieved with nominal ISI penalty.

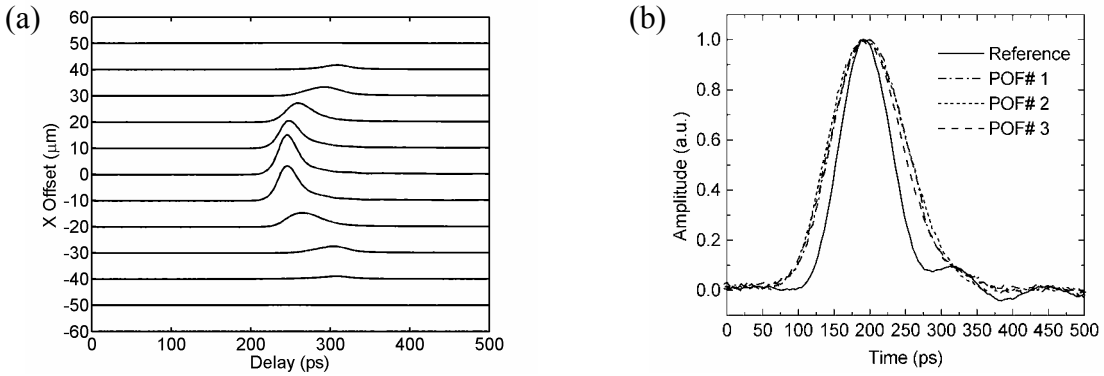

Figure 50. (a) DMD measurement of 100 m of 120 μm GI-PF-POF; (b) Impulse response with the VCSEL source show sufficient bandwidth for 10 Gb/s performance of three samples of GI-PF-POFs

Figure 51 shows the observed eye diagram for the back-to-back (VCSEL-receiver) system and the 100 m POF at 10 Gb/s. The POF yields an open eye; however it suggests

ISI penalty as expected from the impulse response. Similar performance is observed in all three samples of the POF.

The net insertion loss of the SC-connectorized POF is ~10 dB resulting from ~5 dB loss in the fiber and ~2.5 dB loss at each connector. Thus, with an average input power of -5.7 dBm, the optical power margin for the channel is -1.7 dB. We observed a bit error ratio of 10^{-7} due to the finite ISI penalty of the channel. However, with a better extinction ratio and lower loss in the connectors of the POF we can expect a margin of >5 dB and error-free transmission at 10 Gb/s is possible for <100 m POF links.

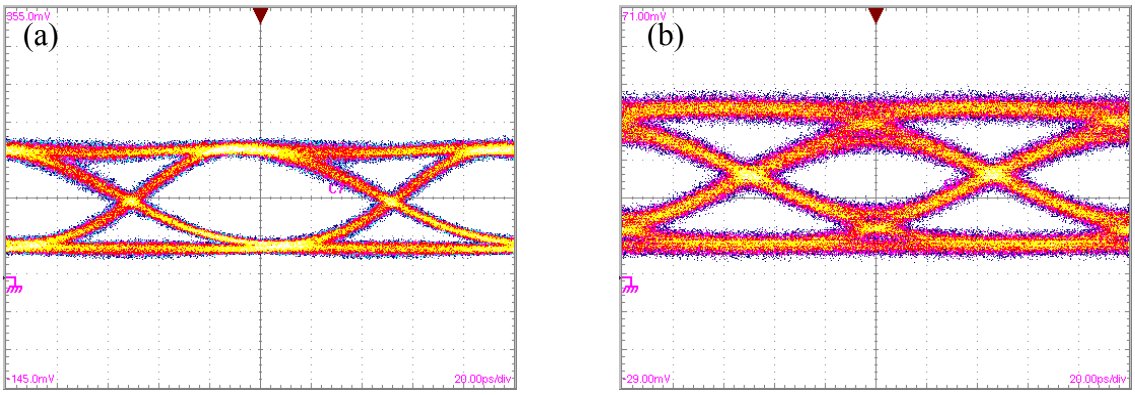

Figure 51. (a) Reference eye diagram at 10 Gb/s with commercial 850 nm VCSEL source and commercial 62.5 μm MMF receiver; (b) Eye diagram at 10 Gb/s after transmission thru 100 m of 120 μm core GI-PF-POF

6.3.2. POF link: using SFP+ VCSEL and large-active-area receiver

We further assessed the launch alignment tolerance of the GI-PF-POF link using a commercial SFP+ transmitter coupled into a 50 μm conventional glass-MMF. The transmit glass-MMF and the POF are butt-coupled and placed on an automated X-Y stage such that the light can be launched at various offsets at the core of the POF. The output of the POF is fully collected by the photodiode without any intervening lens. We note

that the use of a SFP+ receiver incurs ~3dB coupling loss at the receiver and results in additional modal noise penalty. Figure 52a shows the output intensity profile of the transmit MMF and indicates a nearly filled MMF core. Figure 51b shows the received eye for a PRBS 2^{31}-1 pattern. The bandwidth limitation in the eye is primarily due to the receiver.

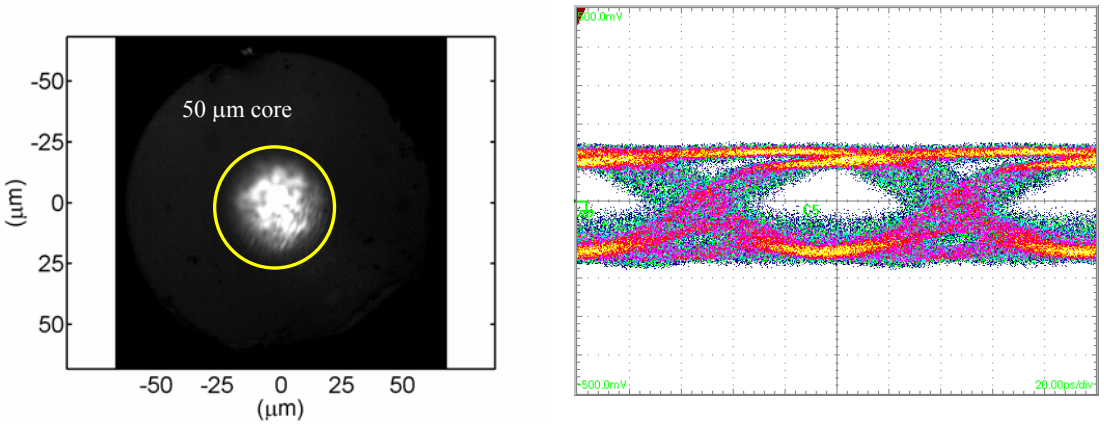

Figure 52. (a) Output intensity profile of the transmit MMF (Circle indicating 50 µm diameter) b) Received 10.3125 Gb/s eye

The transmitted and the received power of the link are -3 dBm and -7.45 dBm. The measured BER for a matrix of X and Y offsets between the transmit MMF and the POF (Figure 53). An error-free (BER<10^{-12}) transmission over ±15 µm offset is observed demonstrating large alignment tolerance at the transmitter. We note that without the large area PIN receiver it would not be possible to collect sufficient power to enable error free transmission.

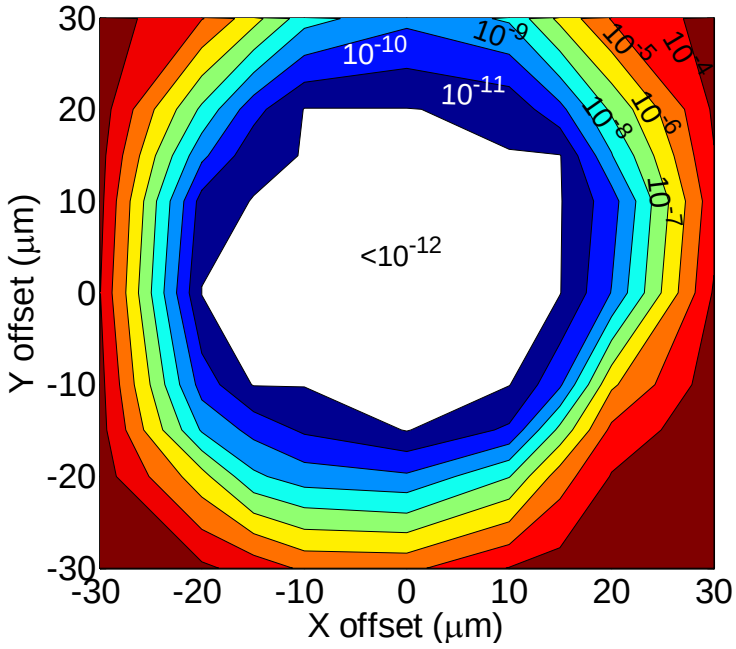

Figure 53. Contour plot of BER vs. offset between the centers of the transmit 50 μm core glass-MMF and 120 μm core GI-PF-POF.

6.3.3. POF link: multimode VCSEL and large-active-area receiver

The research work towards the development of low-cost, alignment-tolerant, short-reach POF link logically converged in the demonstration of the 10 Gb/s POF link comprised of a multimode VCSEL, 120 μm GI-PF-POF and the large-area photoreceiver, described in chapter 5.

Figure 54 shows the experimental set up for the link demonstration. The multimode VCSEL exhibits a measured 3dB bandwidth of 18 GHz and center wavelength near 848nm [53]. Commercially available 10 Gb/s VCSELs are also suitable. However the VCSELs used in this work are known to be multimode and do not have an intervening lens.

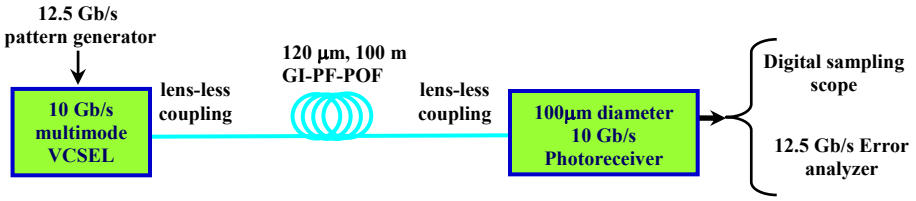

Figure 54. Experimental set up for 10 Gb/s POF link evaluation using multimode VCSEL and large-area photoreceiver

The 100m GI-PF-POF has 120µm core, clad, and a 750µm over-clad. Unlike the conventional glass MMF, the POF is not connectorized and is end-prepared using a POF milling machine. The POF is characterized using conventional DMD measurements. We measured the DMD by scanning the launch single mode fiber at the transmitter end and also scanning the receive face of the POF with a 62.5 µm glass MMF for each launch offset. The responses for different transmit scan positions are shown superimposed for all receiver positions (Figure 55).

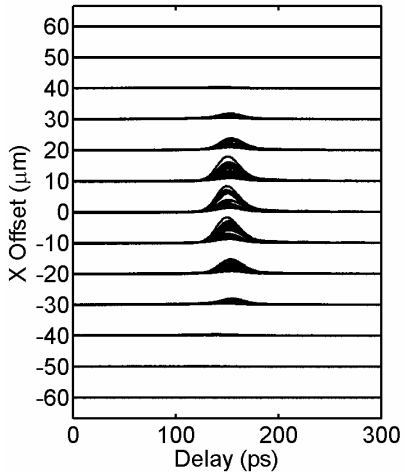

Figure 55. Measured DMD of the 120 µm GI-PF-POF of 100m length. The DMD is 38ps.

The link employs direct coupling of light from the VCSEL to the POF without any collection lens. Similarly, at the receiver-end the light is directly coupled from the POF to the detector. The alignment accuracy at both the transmitter and the receiver is <20μm. The power output from the VCSEL is -4dBm and the received power after the POF is -14dBm. Figure 56a, and Figure 56b show the back-to-back and link eye diagrams at 10Gb/s. The performance is limited by the channel loss and the bandwidth limitation of the receiver and the POF. However, this shows that error-free transmission with high alignment tolerance is possible with improved power budget i.e. better receiver sensitivity and lower POF attenuation.

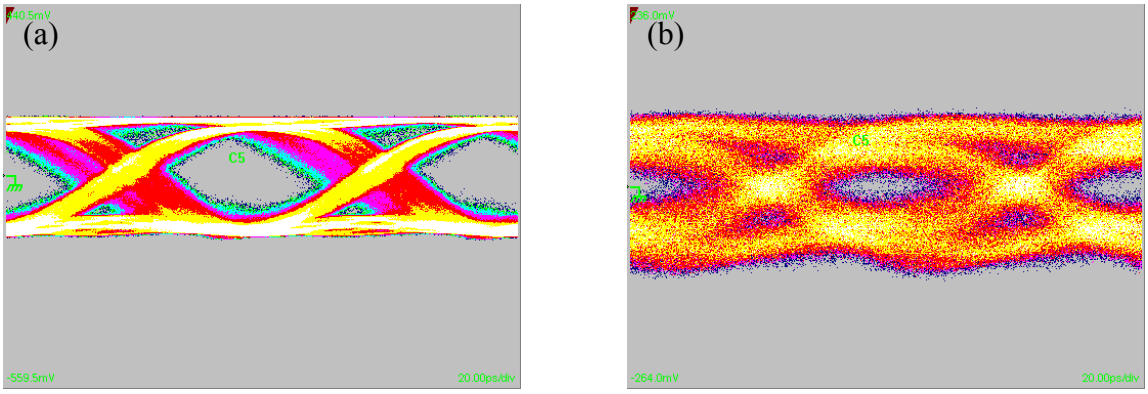

Figure 56. (a) Measured 10Gb/s eye diagram of the back-to-back system comprising of the multimode VCSEL and the large-area photoreceiver connected by 1m of glass MMF; (b) Measured 10Gb/s eye diagram of the alignment tolerant 100m, 120μm core POF link. The light coupling at the transmit-end (multimode VCSEL to POF) and the receive-end (POF to large-area receiver) are lens-free.

6.3.4. Power budget

Power budget is an important consideration in the development of robust optical link. Figure 57 shows the power that has been used in 10 GBASE LRM standard that used

legacy glass-MMF and electronic dispersion compensation to combat the ISI resulting from the limited bandwidth of the glass-MMF.

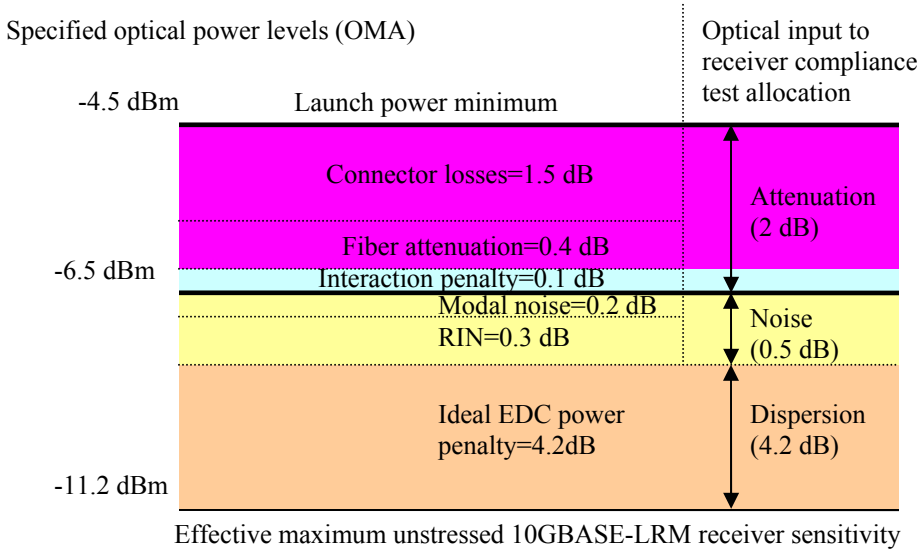

Figure 57. Power budget for IEEE 10GbE LRM (legacy MMF with electronic dispersion compensation)

GI-PF-POF has shown to have sufficient bandwidth for 10Gb/s transmission over >200m. However, the attenuation of POF is relatively higher than glass MMF and therefore, the link length is limited only by the available power budget. Following the power budget of 10 GBASE LRM standard, a power budget for 10Gb/s POF link can be proposed that uses the power allocated for dispersion penalty in fiber attenuation (Figure 58).

It is also noted that the power budget for 10GBASE LRM standard allocates sufficient power margin for VCSEL, receiver, and MMF vendors. This constraint is absent in case of the design of active links and therefore, more aggressive power budget can be used. However, increasing POF link lengths with high yield requires the

development of POF with lower attenuation, transmitter with higher power and design receiver with better sensitivity.

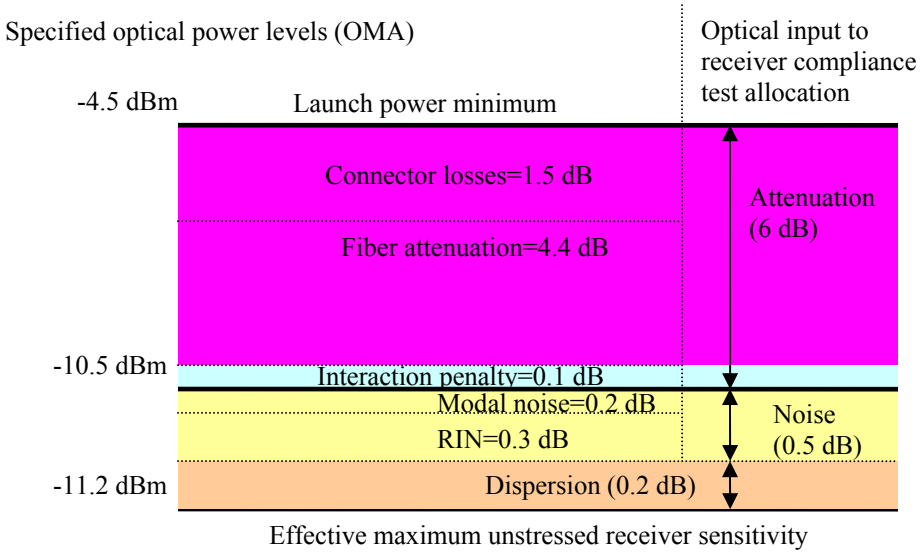

Figure 58. Proposed power budget for alignment-tolerant POF link

6.4. Summary

In this chapter we demonstrated the prototype of short-reach, low-cost, high-performance POF links that is the ultimate focus of this research. The GI-PF-POF has already been shown to be capable of supporting 10Gb/s over 100m of 120μm POF and 40Gb/s over 100m of 50μm POF via DMD measurements. In this chapter, we demonstrated 40 Gb/s transmission over 100 m of 50 mm GI-PF-POF at 1300 nm. With appropriate VCSEL, this performance can also be achieved at 850 nm wavelength. Thus, POF-technology is future proof and can be readily upgraded to higher data rates.

We exploited the full advantages of 120 μm core POF links using the large-active-area photoreceiver described in chapter 5. We showed that multimode VCSELs can be coupled into 120μm core GI-PF-POF without use of a lens and achieve bandwidths necessary to support error-free transmission of >10Gb/s over 100m. We also demonstrated that the developed photoreceiver, even without a lens, can collect the light from 120 μm POF with high efficiency and high alignment tolerance. We finally demonstrated a highly alignment tolerant POF link using a multimode VCSEL, 100m of 120μm core GI-PF-POF, and the developed large-area photoreceiver. The develop link with some improvement in the power budget would dramatically reduce the packaging cost associated with the alignment and thus yield low-cost, short-reach, high data-rate links. Thus we demonstrated all of the necessary functionality needed to deploy 1ow cost 10Gb/s optical links and we show scalability to >20Gb/s.

CHAPTER VII

CONCLUSIONS

7.1. Contributions

The primary focus of this dissertation has been the development of enabling technologies for improved multimode fiber links. The improvements are not only the increase in bandwidth and reach, but the reduction of cost. The approach take for the aforementioned improvements is the holistic view of the channel that involves global optimization of transmitter, fiber, receiver performance and signaling strategies. The optimization resulted in channel designs and impairment mitigation techniques that are combinations of optical, opto-electronic, and electronic methods.

The significant contributions of this research are described below:

- *Evaluation of mode coupling strength of glass-MMF:* The mode coupling strength of conventional glass-MMF is estimated by comparing the impulse responses of long length of MMF obtained using the comprehensive MMF model that includes the mode coupling effects and high-resolution, high-dynamic range impulse response measurements.
- *Use of Raman amplification as channel impairment mitigation technique in glass MMF:* We demonstrated using both numerical analysis and experimental evaluations that mode selective Raman gain in glass-MMF can be used not only to combat attenuation but to reduce intersymbol interference. It is shown that the gain of the lowest order mode in communications grade

GI-MMF is comparable to that found in SMF and an ISI reduction of is 1.4 dB can be achieved with a Raman pump power of 250 mW. The ISI improvement is independent of DMD and bit rate and hence is equally available for higher data-rates and multi-wavelength applications.

- *Numerical demonstration of the effect of the strong mode coupling and 40 Gb/s capability of GI-PF-POF:* We used the comprehensive MMF that includes the mode coupling effect to evaluate the temporal and spatial response of graded-index, perflourinated plastic optical fiber (GI-PF-POF) and showed that strong mode coupling in GI-PF-POF results in Gaussian-like temporal response independent of launch conditions and 40 Gb/s transmission over >100 m is achievable.
- *Experimental evaluation of the temporal behavior of GI-PF-POF:* We performed high-resolution differential modal delay (DMD) evaluation of GI-PF-POF and the results corroborated the facts found via numerical evaluation i.e. GI-PF-POF yields Gaussian-like impulse responses independent of the launch conditions and large bandwidth capable of supporting 40 Gb/s transmission is available for nearly launch-insensitive excitation. We also showed that large bandwidth capable of 10 Gb/s transmission over >200m link is available in large-core (120μm diameter) GI-PF-POF.
- *Demonstration of 40 Gb/s transmission over 100 m of GI-PF-POF:* We performed like demonstration supporting the previous numerical and experimental observations. We showed error-free transmission at a data rate of 40 Gb/s over 100 m of 50 μm core GI-PF-POF.

- *Development of large active area (100μm diameter) photoreceiver for MMF:* To exploit the launch insensitivity and large bandwidth available in 120 μm core GI-PF-POF, we developed photoreceiver with large active area (100 μm diameter) photodiode. The bandwidth limitation resulting from the large depletion layer capacitance of large-area photodiode is mitigated by using a capacitance insensitive transimpedance amplifier (TIA). We developed a regulated cascade input based TIA in 0.35 μm BiCMOS process which has low input impedance and thus provide larger immunity to bandwidth reduction resulting from photodiode capacitance.
- *Demonstration of 10 Gb/s, alignment-tolerant POF link:* We demonstrated alignment-tolerant, 10 Gb/s POF link using a multimode VCSEL, 100m, 120μm-core GI-PF-POF, the developed 100μm-diameter photoreceiver. The large, launch-insensitive bandwidth provides the alignment tolerance at the transmitter; whereas the large area photodetector collects the POF out with large alignment tolerance. The demonstrated 10Gb/s POF link forms the basis for low-cost, short-reach link by the use of passive registration and reduction the packaging cost.

7.2. Future research directions

The most obvious future research direction of this dissertation is the continuation of the of the primary goal of this research i.e. improvement of the MMF link by enhancing the bandwidth-distance while reducing the system complexity and cost.

We have formed the foundation for low-cost, short-reach, 10Gb/s POF links. However, realization of a commercial product requires robust performance with high yield. Therefore, improvement in the power budget is necessary which can be achieved by improving the receiver sensitivity.

The current research has shown that GI-PF-POF is capable of 40 Gb/s transmission at 1300 nm. However, external modulated 40 Gb/s link is not particularly low cost. Link at 850 nm using directly modulated VCSEL would create similar low-cost link at high data rate. Recently, high-data-rate VCSELs have been reported that can be used in these links. However, the challenge lies in the design of the receiver. The approach take for 10 Gb/s receiver is readily scalable to higher data rate where the appropriate choice of photodetector size and the suitable TIA design can yield MMF receiver with high collection efficiency.

REFERENCES

[1]. P. K. Pepeljugoski and D. M. Kuchta, "Design of optical communications data links," *IBM Journal of Research and Development*, vol. 47, pp. 223-237, March/May 2003.

[2]. P. Polishuk, "Plastic optical fibers branch out," *Topics in Design and Implementation*, pp. 140-148, Sept. 2006.

[3]. Y. Koike, and T. Ishigure, "High-bandwidth plastic optical fiber for fiber to the display," *Journal of Lightwave Technology*, vol. 24, pp. 4541-4553, Dec. 2006.

[4]. J.A. Buck, *Fundamentals of Optical Fibers*, John Wiley & Sons, 1995.

[5]. TIA, "FOTP-220 – differential mode delay measurement of multimode fiber in the time domain," TIA-455-220, PN3-0008, 2001.

[6]. IEEE 802.3aq 10G-LRM Task Force; 108 fiber model, http://www.ieee802.org/3/aq/public/tools/108fiberModel.

[7]. [Online] Chromis Fiberoptics, Technology, http://www.chromisfiber.com/techno-why.htm.

[8]. P. Pepeljugosky, D. Kuchta, A. Risteski, "Modal noise BER calculations in 10-Gb/s multimode fiber LAN links," *IEEE Photonics Technology Letters*, vol. 17, December 2005.

[9]. A. M. J. Koonen, "Bit error rate degradation in a multimode fiber optic transmission link due to modal noise," *IEEE Journal on Selected Areas in Communications*, vol. SAC-4, December 1986.

[10]. D. Marcuse, *Theory of Dielectric Optical Waveguides*, Academic Press, 1991.

[11]. R. Olshansky, "Mode Coupling Effects in Graded-Index Optical Fibers," *Applied Optics*, vol. 14, pp. 935-945, April 1975.

[12]. W. A. Gambling, D. N. Payne, and H. Matsumura, "Mode conversion coefficients in optical fibers," *Applied Optics*, vol. 14, pp. 1538-1542, July 1975.

[13]. K. Nagano and S. Kawakami, "Measurements of mode conversion coefficients in graded-index fibers," *Applied Optics*, vol. 19, pp. 2426-2434, July 1980.

[14]. M. Webster, L. Raddatz, I. H. White, and D. G. Cunningham, "A statistical analysis of conditioned launch for gigabit Ethernet links using multimode fiber," *Journal of Lightwave Technology*, vol. 17, pp. 1532-1541, Sept. 1999.

[15]. K. M. Patel and S. E. Ralph, "Enhanced multimode fiber link performance using a spatially resolved receiver," *IEEE Photonics Technology Letters*, vol. 14, pp. 393 -395, March 2002.

[16]. P. Pepeljugoski , J. Schaub , J. Tierno ,B. Wilson, J. Kash, S. Gowda, H. Wu and A. Hajimiri, "Improved Performance of 10 Gb/s Multimode Fiber Optic Links Using Equalization," in *Proc. Optical Fiber Conference*, pp. 472-474, 2003**.**

[17]. A. M. E.-A. Diab, J. D. Ingham, R. V. Penty, and I. H. White, "Statistical analysis of subcarrier-modulated transmission over 300m of 62.5-μm-core-diameter multimode fiber," *Journal of Lightwave Technology*, vol. 23, pp. 2380-2398, August 2005.

[18]. K. Balemarthy and S. E. Ralph, "Low-complexity hybrid MLSE equalizers for 10Gb/s Ethernet multimode fiber links," in *Proc. Optical Fiber Conference*, OW154, 2006.

[19]. K. Balemarthy, A. Polley and S. E. Ralph, "Electronic equalization of multikilometer 10-Gb/s multimode fiber links: mode-coupling effects," *Journal of Lightwave Technology*, v 24, pp. 4885-4894, Dec. 2006.

[20]. M. N. Islam, "Raman amplifiers for telecommunications," *IEEE Journal of Selected Topics in Quantum Electronics*, vol. 8, pp. 548-559, May-June 2002.

[21]. R. H. Stolen, S. E. Miller, and A. G. Chynoweth, *Nonlinear properties of Optical Fibers, Optical Fiber Telecommunications*, Chap. 5, pp. 125-150, Academic, New York, 1979.

[22]. K. S. Chiang, "Stimulated Raman scattering in a multimode optical fiber: evolution of modes in Stokes waves," *Optics Letters*, vol. 17, pp. 352-354, March 1992.

[23]. K. S. Chiang, "Stimulated Raman scattering in a multimode optical fiber: self-focusing or mode competition?," *Optics Communications*, vol. 95, pp. 235-238, January 1993.

[24]. S. H. Baek and W. B. Roh, "Single-mode Raman fiber laser based on a multimode fiber," *Optics Letters*, vol. 29, pp. 153-155, January 2004.

[25]. T. H. Russell, S. M. Willis, M. B. Crookston, and W. B. Roh, "Stimulated Raman scattering in multi-mode fibers and its application to beam cleanup and combining," *Journal of Nonlinear Optical Physics and Materials*, vol. 11, pp. 303-316, 2002.

[26]. Y. Kang, "Calculations and Measurements of Raman Gain Coefficients of Different Fiber Types," Masters Thesis, Virginia Polytechnic Institute and State University, 2002.

[27]. C-A Bunge, R. Kruglov, and H. Poisel, "Rayleigh and Mie scattering in polymer optical fibers," *Journal of Lightwave Technology*, vol. 24, pp. 3137-3146, August 2006.

[28]. Y. Ohtsuka, E. Nihei, and Y. Koike, "Graded-index optical fibers of methyl methacrylate-vinyl benzoate copolymer with low loss and high bandwidth," *Applied Physics Letters*, vol. 57, pp. 120-122, July 1990.

[29]. W. R. White, P. Wiltzius, and M. Dueser, "Scattering loss in plastic optical fiber," *1998 IEEE/LEOS Summer Topical Meeting. Digest. Broadband Optical Networks and Technologies: An Emerging Reality. Optical MEMS. Smart Pixels. Organic Optics and Optoelectronics*, pp. III/17-18, 1998.

[30]. W. White, "New perspective on the advantages of GI-POF," *POF World West 2006*. Santa Clara, 2006.

[31]. R. Michalzik, *Fiber Optic Data Communication*, Elsevier Academic Press, 2002, Chapter: *Optical backplanes, board and chip interconnects*, pp. 245.

[32]. T. Ishigure, E. Nihei, S. Yamazaki, K. Kobayashi, and Y. Koike, "2.5 Gb/s 100 m data transmission using graded-index polymer optical fiber and high-speed laser diode at 650 nm wavelength," *Electronic Letters*, vol. 31, pp. 467-468, March 1995.

[33]. G. Giaretta, M Wegmueller, and R. V. Yelamarty, "11Gb/sec data transmission through 100 m of perfluorinated graded-index polymer optical fiber," in *Proc. Optical Fiber Conference*, San Diego, CA, PD-14, Feb. 1999.

[34]. R. F. Shi, C. Koeppen, G. Jiang, J. Wang, and A. F. Garito, "Origin of high bandwidth performance of graded-index plastic optical fibers," *Applied Physics Letters*, vol. 71, pp. 3625-3627, Dec. 1999.

[35]. W. R. White, M. Dueser, W.A. Reed, and T. Onishi, "Intermodal Dispersion and Mode Coupling in Perfluorinated Graded-Index Plastic Optical Fiber," *IEEE Photonics Technology Letters*, vol. 11, pp. 997-999, August 1999.

[36]. T. Ishigure, M. Kano, and Y. Koike, "Which Is a More Serious Factor to the Bandwidth of GI-POF: Differential Mode Attenuation or Mode Coupling?" *Journal of Lightwave Technology*, vol. 18, pp. 959-965, July 2000.

[37]. G. Jiang, R. F. Shi, and A. F. Garito, "Mode coupling and equilibrium mode distribution conditions in plastic optical fibers," *IEEE Photonics Technology Letters*, vol. 9, pp. 1128-1131, August 1997.

[38]. S. E. Golowich, W. White, W. A. Reed, and E. Knudsen, "Quantitative estimates of mode coupling and differential modal attenuation in perflourinated graded-index plastic optical fiber," *Journal of Lightwave Technology*, vol. 21, pp. 111-121, January 2003.

[39]. K. M. Patel, A. Polley, K. Balemarthy and S. E. Ralph, "Spatially resolved detection and equalization of modal dispersion limited multimode fiber links," *Journal of Lightwave Technology*, vol. 7, pp. 2629-2636, July 2006.

[40]. Cosemi Technologies : GaAs photodiode MXP7002 web reference: http://www.cosemi.com/gaas.html#

[41]. Albis Optoelectronics : GaAs photodiode PDCS100T-GS web reference: http://www.albisopto.com/index.php?PageID=3&rnd=c001d3

[42]. Vitesse : GaAs photodiode VSC7780 web reference: http://www.vitesse.com/products/product.php?number=VSC7780

[43]. Hamamatsu : MSM photodetector G4176-01 web reference: http://sales.hamamatsu.com/index.php?id=13186743&language=1&undefined

[44]. S. M. Park, and H.-J. Yoo, "1.25-Gb/s regulated cascode CMOS transimpedance amplifier for Gigabit Ethernet application," *IEEE J. of Solid-State Circuits*, vol. 39, No. 1, pp. 112-121, January 2004.

[45]. S. M. Park, "Gigabit CMOS transimpedance amplifiers for optical communication applications," *Proceedings of the 7th Korea-Russia International Symposium,KORUS 2003*, pp. 211-215, 2003.

[46]. W.-Z. Chen, Y.-L. Cheng and D.-S. Lin, "A 1.8V 10-Gb/s fully integrated CMOS optical receiver analog front-end," *IEEE journal of solid-state circuits*, vol. 39, no. 1, June 2005.

[47]. C. Kromer, G. Sialm, T. Morf, M. L. Schmatz, F. Ellinger, D. Erni and H. Jackel, "A low power 20-GHz 52-dBΩ transimpedance amplifier in 80-nm CMOS," *IEEE journal of solid-state circuits*, vol. 39, no. 1, June 2004.

[48]. Z. Lu, K. S. Yeo, J. Ma, M. A. Do, W. M. Lim and X. Chen, "Broadband design techniques for transimpedance amplifier," *IEEE transactions on circuits and systems-I: regular papers*, vol. 54, no. 3, March 2007.

[49]. C.-T. Chan, and O. T.-C. Chen, "Inductor-less 10Gb/s CMOS transimpedance amplifier using source-follower regulated cascode and double three-order active feedback," *ISCAS 2006*, pp. 5487-5490, 2006.

[50]. S.-J. Sim, J. Park, and S. M. Park, "A 1.8V, 60dBΩ, 11GHz transimpedance amplifier with strong immunity to input parasitic capacitance," *ISCAS 2006*, pp 5483-5486, 2006.

[51]. Picometrix: High-speed receiver compatible with 62.5 μm MMF for 10 GbE standard. web reference http://www.advancedphotonix.com/ap_products/pdfs/pico_bulletins/PT-12B-PB.pdf

[52]. G. Giaretta, W. White, M. Wegmuller, and T. Onishi "High Speed (11 Gbit/s) Data Transmission Using rfluorinated Graded-Index Polymer Optical Fibers for Short Interconnects (<100 m)," *IEEE Photonics Tech. Lett.*, vol. 12, pp. 347-349, 2000.

[53]. P. O. Leisher, C. Chen, J. D. Sulkin, M. S. B. Alias, K. A. M. Sharif, and K. D. Choquette, "High Modulation Bandwidth Implant-Confined Photonic Crystal Vertical Cavity Surface Emitting Laser," *IEEE Photon. Tech. Lett.*, vol. 19, pp. 1541-1543, 2007.

PUBLICATIONS

1. **A. Polley**, P. J. Decker and S. E. Ralph, "10 Gb/s, 850nm VCSEL-POF links," *2008 Conference on Lasers and Electro-Optics (CLEO)*, 2008, CTuLL3.
2. **A. Polley** and S. E. Ralph, "100 m, 40 Gb/s Plastic Optical Fiber Link," *Optical Fiber Communication Conference (OFC)*, 2008.
3. **A. Polley** and S. E. Ralph, "Mode coupling plastic optical fiber enables 40Gbps performance," *IEEE Photonics Technology Letters*, vol. 19, pp. 1254-1256, August 2007.
4. **A. Polley**, K. Balemarthy and S. E. Ralph, "Mode coupling: Why POF supports 40Gbps," *2007 Conference on Lasers and Electro-Optics (CLEO)*, 2007, CWM5.
5. **A. Polley**, R. J. Gandhi and S. E. Ralph, "40 Gbps short reach links using plastic optical fiber," *Optical Fiber Communication Conference (OFC)*, 2007, OMR5.
6. **A. Polley** and S. E. Ralph, "Receiver-side, adaptive, opto-electronic chromatic dispersion compensation of single-mode fiber," *Optical Fiber Communication Conference (OFC)* 2007, JThA51.
7. **A. Polley** and S. E. Ralph, "Raman amplification in multimode fiber," *IEEE Photonics Technology Letters*, vol. 19, pp. 218-220, Feb. 2007.
8. **A. Polley** and S. E. Ralph, "Raman amplification in multi mode fiber: Reduction of inter-symbol interference via mode selective gain," The 19th Annual Meeting of the IEEE *Lasers and Electro-Optics Society (LEOS)* 2006.
9. **A. Polley** and S. E. Ralph, "Raman Amplification in Multi-Mode Fiber: Reduction of Inter-Symbol Interference via Mode Selective Gain," *2006 Optical Amplifiers and their Applications (OAA) Topical Meeting*, paper OWC2, 2006.
10. K. Balemarthy, **A. Polley** and S. E. Ralph, "Electronic equalization of multikilometer 10-Gb/s multimode fiber links: mode-coupling effects," *Journal of Lightwave Technology*, v 24, n 12, Dec. 2006, p 4885-94.

11. K. M. Patel, **A. Polley**, K. Balemarthy and S. E. Ralph, "Spatially resolved detection and equalization of modal dispersion limited multimode fiber links," *Journal of Lightwave Technology*, v 24, n 7, July 2006, p 2629-36.
12. **A. Polley**, J. H. Kim and S. E. Ralph, "Efficient photoconductive THz source with spatially shaped excitation" *2005 Conference on Lasers and Electro-Optics (CLEO)* , v 3, 2005, p 1942-4.
13. J. H. Kim, **A. Polley** and S. E. Ralph, "High efficiency terahertz photoconducting sources by use of spatially shaped excitation," The 17th Annual Meeting of the IEEE *Lasers and Electro-Optics Society (LEOS) 2004*, v 1, Nov. 2004, p 374-5.
14. J. H. Kim, **A. Polley** and S. E. Ralph, "Efficient photoconductive terahertz source using line excitation," *Optics Letters*, v 30, n 18, Sept. 2005, p 2490-2.
15. S. E. Ralph, Z. Zhiyong, D. Mattox, K. M. Patel, K. B. Wise and **A. Polley**, "Optimizing the third-order optical susceptibility of Pt-doped BaTiO3 grown by combustion chemical vapor deposition," *2004 Conference on Lasers and Electro-Optics(CLEO)*, v 1 , May 2004, p 1132-3.
16. S. E. Ralph, K. M. Patel, C. Argon, A. **Polley** and S. W. McLaughlin, "Intelligent receivers for multimode fiber: optical and electronic equalization of differential modal delay," The 15th Annual Meeting of the IEEE *Lasers and Electro-Optics Society (LEOS)*, v 1, Nov. 2002, p 295-6.

INVENTION DISCLOSURES

[1] **Arup Polley** and Stephen E. Ralph, “Mode selective Raman gain in multimode fibers to improve link performance”, GTRC ID No. 3778, March 2006.

[2] **Arup Polley** and Stephen E. Ralph, “Opto-electronic mitigation of chromatic dispersion impairment in single mode fiber link via intensity and phase recovery,” GTRC ID No. 3810, May 2006.

[3] **Arup Polley** and Stephen E. Ralph, "High-Speed Optical Receiver Circuit based on a Regulated Cascode Input Stage that Provides High Insensitivity to Input (Photodetector and Electrostatic Discharge Protecting Circuit) Capacitance," GTRC ID No. 4280, Dec 2007.

[4] **Arup Polley** and Stephen E. Ralph, "Low-Complexity, High-Speed Optical Link using Multimode Fiber and Receiver Comprising Large Area Detector and Input Capacitance Insensitive Transimpedance Amplifier," GTRC ID No. 4281, Dec 2007.

VITA

Arup Polley was born in Seuri, West Bengal, India in 1980. He received his Bachelor of Technology (B. Tech) degree in Electronics and Electrical Communication Engineering from Indian Institute of Technology, Kharagpur, India in 2003. In the same year, he came to Geogia Institute of Technology to pursue Ph.D. in Electrical Engineering in Ultrafast Optical Communications Group. He received Master of Science (M.S.) degree from Georgia Institute of Technology in Electrical and Computer Engineering and Physics in 2005 and 2008 respectively.

During the course of his Ph. D. program he has performed research in the modeling of TeraHertz signal generation in photoconductive switches and equalization of single mode and multimode fiber-optic channels. His primary research has been the development of low-cost, high-performance link design using plastic optical fiber. His research interests include optical communications and analog circuit design.

He is a student member of IEEE.